UNIVERSIDAD DE GRANADA

Ph.D. Thesis

Instrumentation based on flexible technology for biomedical sensorization and monitorization

Author
Víctor Toral López

Supervisors
Antonio García Ríos
Encarnación Castillo Morales

Doctoral Program in Information and Communication Technologies
Department of Electronics and Computer Technology

—

Granada, November 2022

Editor: Universidad de Granada. Tesis Doctorales
Autor: Víctor Toral López
ISBN: 978-84-1117-666-8
URI: https://hdl.handle.net/10481/79670

Instrumentation based on flexible technology for biomedical sensorization and monitorization

by Mr. Víctor Toral López
University of Granada, Department of Electronics and Computer Science

Palabras clave: Electrónica flexible, Bioseñales, Instrumentación, Electrónica impresa

Resumen

El uso de electrónica flexible para instrumentación biomédica, supone un gran avance para conseguir una monitorización continua mediante dispositivos *wearables*. En esta Tesis, se estudia el uso de nuevos materiales y técnicas de impresión para la consecución de un dispositivo de monitorización biomédica.

En primer lugar, se han desarrollado electrodos sobre diferentes materiales flexibles basados en grafeno, polímeros y tintas conductoras. Estos electrodos flexibles se han realizado empleando técnicas de impresión como *screen printing* o grabado láser. Además, se han estudiado sobre distintos substratos flexibles como pueden ser láminas de plásticos flexibles o textiles, siendo este último el más interesante para los dispositivos *wearables*. Las técnicas de impresión también se han utilizado para crear sensores flexibles a través de materiales orgánicos innovadores como son los *Metal-Organic Frameworks* (MOFs).

Por otra parte, también se ha estudiado la electrónica flexible aplicada al campo del *energy harvesting*, un campo muy interesante para aumentar la autonomía de los dispositivos *wearable*. En este aspecto se han desarrollado electrodos flexibles para el almacenamiento de energía. Se han empleado materiales como los MXenes y junto con polímeros conductores para crear dispositivos con capacidad de almacenar energía en un reducido espacio y manteniendo su flexibilidad.

Finalmente, toda la tecnología desarrollada, se ha combinado en un dispositivo *wearable* basado en electrónica reconfigurable que permite la monitorización de distintas señales biomédicas en un solo dispositivo.

Instrumentation based on flexible technology for biomedical sensorization and monitorization

by Mr. Víctor Toral López
University of Granada, Department of Electronics and Computer Science

Keywords: Flexible electronics, Biosignals, Instrumentation, Printed electronics

Abstract

The use of flexible electronics for biomedical instrumentation represents a great advance to achieve continuous monitoring through wearable devices. In this thesis, the use of new materials and printing techniques to achieve a biomedical monitoring device is studied.

First, electrodes have been developed on different flexible materials based on graphene, polymers and conductive inks. These flexible electrodes have been created using printing techniques such as screen printing or laser engraving. In addition, they have been studied on different flexible substrates such as flexible plastic sheets or textiles, the latter being the most interesting for wearable devices. Printing techniques have also been used to create flexible sensors through innovative organic materials such as Metal-Organic Frameworks (MOFs).

On the other hand, flexible electronics applied to the field of energy harvesting have also been studied, since it is a very interesting field to increase the autonomy of wearable devices. In this regard, flexible electrodes have been developed for energy storage. Materials such as MXenes and conductive polymers have been used to create devices capable of storing large amounts of energy in a small space while maintaining flexibility.

Finally, all the technology developed has been combined in a wearable device based on reconfigurable electronics that allows the monitoring of different biomedical signals in a single device.

Agradecimientos

En primer lugar, me gustaría agradecer su labor de dirección y tutela a mis directores Antonio García y Encarnación Castillo. Gracias a sus consejos esta tesis se ha podido llevar a cabo satisfactoriamente. También me gustaría agradecer los consejos y orientación de Diego P. Morales, que sin figurar como director formalmente, ha ejercido como tal a lo largo de este proyecto. Gracias a los tres por ayudarme a crecer tanto en plano académico como humano, buscando siempre que pueda evolucionar como investigador.

A mis compañeros del departamento y de despacho, especialmente a Fran Romero, quisiera agradecer la ayuda que siempre me han prestado cuando ha sido necesario. Y a todos los componentes del Departamento de Electrónica que me han acogido como uno más y me han integrado en todas las actividades del departamento. También quisiera agradecer a los miembros del Departamento de Química Analítica, Alfonso, Inma y Sergio, que me acogieron en sus laboratorios cada vez que lo necesité y me prestaron toda la ayuda necesaria en los experimentos.

Durante mi doctorado tuve la oportunidad de hacer una estancia en Lovaina en el grupo de Francisco Molina, al que agradezco su hospitalidad y disposición para ayudarme a llevar a cabo mis investigaciones allí ya que me hicieron sentir como en casa.

Como en todo gran proyecto, se necesita el apoyo de muchas personas externas al mismo, pero sin las cuales es imposible llevarlo a término. Entre ellas están mis amigos, que siempre han estado en los mejores y en los peores momentos para acompañarme o darme ánimos. Especialmente a Ignacio, que, desde que nos conocimos siempre ha estado ahí para todo, desde hacer de psicólogo a pasar frío o calor en la cuneta de una carretera para ver un rallye, pero sobre todo por ser una de esas personas que te hacen crecer cuando están a tu lado. También a mis compañeros de carrera, a los que siempre puedo recurrir tanto para pasar ratos inolvidables como cuando uno pasa por momentos duros

Por supuesto, llegar hasta aquí habría sido imposible sin las personas más importantes, mi familia, tanto biológica como no biológica que me han ayudado a ser lo que soy hoy. Gracias a Javier, Mari Carmen y Carmen

Ana que me habéis apoyado y aconsejado en estos años. A mis hermanos, Ana y Alex, siempre dispuestos a ayudar, a soportar mis defectos y a estar para lo que sea. A mis padres, Francisco y Victoria, gracias a los que he aprendido a ser como soy, por los valores que me han inculcado tanto para el trabajo como para la vida. En especial a mi padre, fallecido durante la realización de esta Tesis, que me inculcó siempre la pasión por los libros y el conocimiento y me enseñó a mantener los pies en la tierra. Gracias a todos, por soportar mis defectos y apoyarme en todo.

Y sobre todo gracias a Andrea, la persona que más ha tenido que soportar mis defectos y mis malos momentos en estos años. Que me ha apoyado incondicionalmente para todos mis proyectos y que me ha acompaña en la vida, haciendo que el camino no solo sea más llano, sino más completo. Gracias por hacerme mejor persona y descubrirme un mundo mejor.

Contents

List of Figures

List of Tables

List of Acronyms

ADC Analog-Digital Converter. 14, 15, 48, 50, 147, 170

ALU Arithmetic Logic Unit. 13–15

ALS Amyotrhopic Lateral Sclerosis. 21

ASIC Aplication Specific Integrated System. 140, 155

BAN Body Area Network. 3

BLE Bluetooth Low Energy. 12, 16, 17, 36, 46, 142, 149

BPM Bit Per Minute. 49

CAT Computarized Axial Tomography. 4

CGM Continous Glucose Monitoring. 4

CHF Congestive Heart Failure. 35

CP Coordination Polymer. 6, 119, 121, 125, 126, 129, 132, 133, 189

CPU Central Process Unit. 13, 14

CV Cyclic Voltammetry. 178, 180, 181

CVD Chemical Vapor Deposition. 63–65

DAC Digital-Analog Converter. 169

DFB Digital Filter Block. 14

DMA Direct Memory Access. 14

DMSO Dimethyl sulfoxide. 177

DWT Discrete Wavelet Transfom. 24, 25, 43

ECG Electrocardiogram. 7, 17–19, 34–37, 39, 41–44, 46, 47, 49–51, 53, 62, 63, 66, 68–72, 80, 88, 139, 144–152, 156, 157, 189

EEG Electroencephalogram. 62, 63, 139

EMG Electromyogram. 7, 17, 19, 20, 62, 63, 70–72, 77, 79, 81, 88, 139, 145–149, 154–157, 189

EOG Electrooculogram. 7, 17, 20, 21, 62–64, 66, 68–72, 74, 81, 139, 145–148, 151–153, 156, 157, 189

FET Field Effect Transitor. 105, 119

FN False Negative. 44, 71, 148, 150

FIR Finite Impulse Response. 14, 44

FP False Positive. 44, 71, 148, 150

FPAA Field Programable Analog Array. 13

FPGA Field Programable Gate Array. 13

GUI Graphic User Interface. 48

GO Graphene Oxide. 9, 10

HMI Human-Machine Interface. 20, 21

HR Heart Rate. 35, 44, 50, 53

ICG Impedance CardioGram. 35

IDE Integrated Developement Enviroment. 14

IDE Inter-Digitated Electrodes. 6, 104–107, 109, 110, 112, 121, 122, 132, 166, 179, 180, 189

I^{2}C Inter-Integrated Circuit. 37, 38, 45

IDWT Inverse Discrete Wavelet Transform. 24

IIR Infinite Impulse Response. 14

IoT Internet of Thing. 3–5, 62, 105

IWT Inverse Wavelet Transform. 24

LED Light Emitter Diode. 40

LIG Laser Induced Graphene. 9, 10, 28, 62–66, 75–81, 140, 144, 157, 177, 178, 180, 181, 184, 189, 190

MDF Median Frequency. 70, 71, 81, 149

MEMS MicroElectroMechanical Systems. 45

MNF Mean Frequency. 70, 79, 81, 149

MOF Metal-Organic Framework. 104, 105, 108, 119, 125, 166, 189, 190

MPU Main Process Unit. 45

MVIC Maximum Voluntary Isometric Contraction. 70, 148

OFET Organic Field Effect Transitor. 119

PANi Polyaniline. 11

PC PolyCarbonate. 179

PCA Principal Component Analysis. 151

PCB Printed Circuit Board. 45, 47, 190

PDMS Polydimethylsiloxane. 64

PEDOT poly(3,4-ethylenedioxythiophene). 11, 89, 140, 178, 181, 183, 184, 190

PET Polyethilene terephthalate. 64, 91, 92, 95–97, 107

PGA Programable Gain Amplifier. 15, 16

PLD Programable Logic Device. 13

POC Point Of Care. 167, 190

PPG PhotoPlestimoGraphy. 35, 37, 39, 42, 47, 49, 53

PPO Poly-Phenylene Oxide. 11

PRoC Programable Radio on Chip. 12, 16

PSoC Programable System on Chip. 12, 13, 16, 36–38, 40, 42, 45, 48, 53, 141, 142, 145, 147, 169–171

PTT Pulse Transist Time. 35

PVA Poly-Vinyl Alcohol. 179, 184

PVDF Polyvinylidene fluoride. 179

PWM Pulse Width Modulation. 13, 37, 38, 40

RAM Random Access Memory. 14

RFID RadioFrequency IDentification. 166–168, 170, 171

rGO reduced Graphene Oxide. 9, 28, 140

RH Relative Humidity. 6, 105, 108–112, 119, 129–133, 189, 190

RMS Root Means Square. 77, 155

SEM Scaning Electronic Microscope. 10

SNR Signal-Noise Ratio. 45, 71, 75

SPI Serial Periphereal Interface. 141, 143

SRAM Static Random Acces Memory. 13

TBAOH Tetrabutylammonium hydroxide. 177, 178

TD True Detected. 71, 148

TEG Thermo-Electric Generators. 11, 190

TIA Transimpedance Amplifier. 40

UART Universal Asynchronous Reciever Transmitter. 37, 38, 46, 141

UDB Universal Digital Blocks. 13, 38

USB Universal Serial Bus. 13, 37, 45, 47

WHMS Wearable Health Monitoring System. 34

Glossary

accelerometer Device capable to measure the acceleration, usually based on MEMS. 37, 38, 45, 46

baseline wandering Low frequency and high amplitude oscillation, as the one produce by breathing during biosignals acquisitions. 25, 44

biosignal signal generated by the human body, generally refered to electrical signal like ECG or EMG for example. 63, 147

clustering Signal processing method, based in classification on clusters depending on a characteristic value. 44, 151

colorimetric measurement Measurement method based in translate the measured value to a color which subsequetnly is readed by a image system. 143

lead They are the recording of the difference in electrical potentials between two points, either between two electrodes (bipolar lead) or between a virtual point and an appliance (monopolar lead). 18

electrochemical capacitors Energy storage devices, based on physical charge storage and surface redox reactions. 178

energy harvesting Devices and techniques oriented to extract energy from non-convetional sources like solar cells, radiofrequency or termoelectric generators. 177, 190

Fourier Transform mathematical transform that decomposes functions into frequency components. 22

trans-impedance amplifier Amplifier which converts a current singal to a voltage signal. 40

gyroscope System to measure the orientation of a device using gyroscopic effect, usually implemented as MEMS. 45

harmonic Multiple of a determined frequency. 21, 43

Holter monitor Heart monitoring device, which stores the ECG of the user during a period to be analysed later by a specialist. 34, 139

Information Age Historical period that began in the mid-20th century, characterized by a rapid transition from traditional industry to an economy mainly based upon information technology. 3

instrumentation amplifier High precsision diferenttial amplifier, composed by three operation amplifiers. 42

Internet of Things New paradigm of the Internet in which the devices communicates between them without human interference. 3, 62

isometric Muscular contraction without movement. 70, 148

isotonic Muscular contraction with a constant force. 70

Kapton Commercial name for polyimide manufactured by DuPont, that has great temperature and chemical resistance. 10, 63, 65, 80, 144

MicroElectroMechanical Systems Miniature machine that contains mechanical and electronic components. 45

Moore's Law Law which describes the developement of transistors, posited that roughly every two years, the number of transistors on microchips will double. 3

photoplestymography Method to measure oxigen saturation in blood using red light. 35

pseudocapacitance Energy storage mechanism based on surface redox reactions. 180

QRS Signal of a heart beat denoted by the characteristics points Q, R, S of the ECG signal. 34, 44, 49–51, 54

Raman spectrum spectroscopy analysis technique based on Raman dipersion. 65

saccadic Quick movement of both eyes to change the focus of the sight. 20, 147, 151, 153

supercapacitor High-capacity capacitor, which is able to accept and deliver charge much faster than batteries. 190

Thermo-Electric Generator solid state device that transform a temperature difference to electrical energy. 11

wavelet Non-zero function with finite integer, usually termed as short oscillation (see subsection 2.4.1). 22–24, 43, 145, 149

Wavelet Transform Mathematic transform based on a wavelet (see subsection 2.4.1). 19, 20, 22, 24, 25, 43, 67, 70, 75, 145

white noise random signal having equal intensity at different frequencies, giving it a constant power spectral density. 26

Part I

Background

Chapter 1

Introduction

The development of the transistor in 1947 [1] is considered the onset of the Information Age in which the humanity is involved nowadays. In this era, electronics are one of the main factors of evolution and economic growth. Since then, the evolution of electronics and communications has been as explosive as the social transformation they bring. First developments were mainly devoted to improve computation capacity and miniaturization, following the Moore's Law. Also communications were improving along with the introduction of new devices. Both wireless and wired communication technologies could be developed thanks to better devices. In any case, the groundbreaking development for the democratization of Information Age were the Internet and the Personal Computer (PC)

However, the greatest expansion of this Information Age starts with the introduction of smartphones in 2007. The first cell phones with internet connection appeared around 2000, but their use to access the Internet was residual in comparison to computers. The introduction of the LG Prada and the iPhone in 2007 started the Information Age´s revolution. These devices had two disruptive characteristics: the use of a large tactile screen, and several wireless connections especially oriented to access the internet everywhere. Thanks to these characteristics, smartphones changed the way the society relates with technology and even the way people relate to each other. Since then, almost everybody carries a smartphone all day long, so these devices can be seen as a gateway to a virtual world. From the perspective of this Thesis topic, smartphones quickly became the central device of the Body Area Network (BAN) along with wearable devices.The current smartphones capabilities make them the best interface between the user and wearable devices, but also between the wearable itself and a wide offer of internet services integrated in the Internet of Things (IoT) paradigm, which will be presented below.

Despite wearable technology has been constantly developed since the early 1990s, mainly driven by Steve Mann, known as "the father of wearable computing", it is not until 2014 that this technology became widely known and used. Several devices like Google Glass and FitBit devices were announced on this year. These devices were oriented to wearable augmented reality and activity monitoring, respectively. Wearable augmented reality had no success and all the development has been kept in an academic plane. However, activity monitoring has been widely used since then. Big firms, like Apple, have entered the market with devices such as the Apple Watch. The main use of these devices is sport monitoring along with notification or interface with the user, but their use for health monitoring is still limited. It is possible to say that the most common and the first wearable device oriented to health monitoring is the Holter monitor, used to capture the ECG signal of the user during long periods. However, even nowadays, it is bulky and may interfere in some daily activities of the user. More recently, there has been some commercial development in this regard of devices like Continuous Glucose Monitors (CGM) for people suffering from diabetes [2, 3]. However, all these devices have not yet evolved to the point where they can be used as a remote diagnosis tool for medical personnel.

The second important field for the market of wearables has been IoT developments. Despite the term started to be widely known in 2009, it was coined in 1999 by Kevin Ashton. Several developments appeared since then, like the first connected fridge from LG, but it is not until the expansion of Internet driven by the smartphones that IoT devices started to flood our daily life. Almost every field has been influenced in some way by the IoT and Big Data advances. Medicine is one of these fields in which electronics has been more and more present, from diagnostic devices, such as electronics radiography or Computarized Axial Tomography (CAT) scans, to connected patient information databases. However, all these advances have been kept inside hospital environments.

There are several reasons that make advantageous the fact of getting these services outside the hospitals, first one being the aging of population in the incoming years. It is expected that this phenomenon will tend to saturate public health systems in the future. Thus, diagnostic devices and patient remote monitoring may help to mitigate this problem. Diagnostic devices and remote monitoring of patients can help reduce this saturation. Another aspect that can be improved is the early detection of different conditions, since easy access to diagnosis devices facilitates provisional diagnosis, sometimes even before first symptoms appear. Another point of interest for

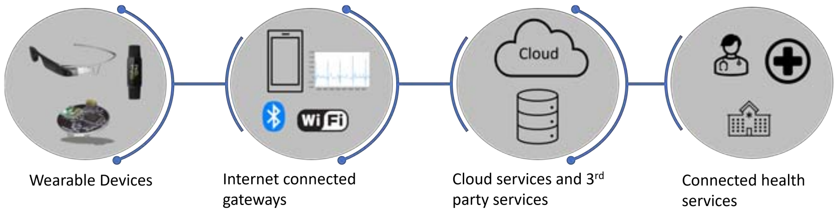

Figure 1.1: Health wearables IoT achitecture.

these devices is the possibility of collecting data to perform Big Data analysis, either for research or even to obtain more information from the user [4]. The objective is thus to develop an architecture similar to the one shown in Figure 1.1.

In summary, despite there are some advances in wearable technology, there are still challenges to overcome. For this, several technologies can be combined in an innovative solution. In one hand, flexible electronics technology paves the way to better integration and ergonomics of biomedical wearables. On the other hand, novel sensors like those based on μPAD or organic materials in combination with electronics, can be used as a remote portable laboratory [5]. Finally, all these technologies can be integrated in an IoT architecture to permit the remote diagnosis and monitoring of patients.

1.1 Objectives

As described above, there are big challenges to address in the field of wearables applied to health. This Thesis is focused on the study of flexible electronics for wearable devices applied to health with the main objective of creating a flexible instrument for biomedical monitoring. The work has been divided in the following objectives:

- **Development of electrodes and sensors based on flexible materials:** Using novel materials like Graphene derivatives and conductor polymers, several electrodes will be created and studied to acquire biosignals. Also flexible sensors will be developed to measure chemical substances.
- **Implementation of a flexible prototype**: A prototype based on reconfigurable electronics will be created with capabilities to combine these traditional devices with the flexible electronics previously developed.

- **Implementation of signal processing algorithms:** Algorithms mainly based on wavelets will be used to process and improve the signals acquired with the prototypes.

1.2 Thesis outline

This Thesis document is presented as a compendium of articles. The structure of Articles is the following:

- **Publication I**: This publication covers the development of a reconfigurable device as a first approximation to a prototype for signal acquisition. It was developed as a platform to monitor people during risk activities like soldiers or first responders.
- **Publication II**: This publication shows the use of novel materials to create flexible electrodes. In this publication, several materials are used for the creation of electrodes. These electrodes are studied in their physical and electrical properties as well as their behavior during signal acquisition in comparison to commercial electrodes.
- **Publication III**: This publication is devoted to flexible electrodes on textile substrates. Several conductive pastes based on carbon and silver are used to print on textiles to create electrodes. The electrodes are studied in terms of reproducibility of the patterns, and electronic and physical properties.
- **Publication IV**: In this publication, the use of novel organic materials is shown. In this paper an Relative Humidity (RH)-sensitive device is presented and optimized to change its response by controlling the fabrication parameters. This work is a demonstration of flexible materials to create sensors. Despite it is presented as an environmental sensor, thanks to its flexibility it can be used in wearable devices for safety applications.
- **Publication V**: In this work, a Coordination Polymer (CP) based on sodium ions is used as Relative Humidity (RH) sensor. In this paper its used as flexible sensor in combination with printed IDE devices is shown.
- **Publication VI**: This publication presents a wearable device, based on flexible electronics, for biosignals acquisition. In this work a prototype for flexible electrodes is shown. This prototype, thanks to reconfigurable electronics, is able to acquire the most usual biosginals:

ECG, EMG and EOG. Also, a custom Android app is presented, which acts as interface for the wearable device.

- **Publication VII**: This publication shows an application of RFID for wireless biosignal applications. An RFID based rearder is presented and applied to wireless biosensing. This device can be used in combination with LC tags to measure substances of interest.

Additionally, some results on energy harvesting will be presented in Chapter 10. These results have yet to be published, as the related work is still under development. Finally, the main conclusions of this Thesis will be presented in Chapter 11.

Bibliography

[1] J. Bardeen and W. H. Brattain, "The transistor, a semi-conductor triode," *Physical Review*, vol. 74, no. 2, pp. 230–231, jul 1948.

[2] T. Martens, R. W. Beck, R. Bailey, K. J. Ruedy, P. Calhoun, A. L. Peters, R. Pop-Busui, A. Philis-Tsimikas, S. Bao, G. Umpierrez, G. Davis, D. Kruger, A. Bhargava, L. Young, J. B. McGill, G. Aleppo, Q. T. Nguyen, I. Orozco, W. Biggs, K. J. Lucas, W. H. Polonsky, J. B. Buse, D. Price, R. M. Bergenstal, A. Carlson, S. Chambers, S. Yang, M. S. Kirkman, A. Kass, R. Fraser, T. Cushman, C. Ramos, M. Magar, M. Walker, S. Serafin-Dokhan, M. Salam, S. Hurst, M. J. Clifton, J. Kravarusic, A. Bansal, C. Fulkerson, L. Ang, C. Richardson, K. Mizokami-Stout, J. Reiss, V. Leone, K. Stifel, G. Dailey, A. Change, J. McCallum, M. I. Garcia, D. Davis, C. Lovell, C. Root, F. Toler, L. Wilhelm, R. Eifert, L. Murguia, B. Cota, L. Nguyen, R. Lipski, M. K. Lawrence, A. Fournier, M. Carter, S. Hoover, N. Cohen, T. Mouse, J. Rusnak, T. Campos, N. Njeru, T. Arant, S. E. Beck, and A. B. and, "Effect of continuous glucose monitoring on glycemic control in patients with type 2 diabetes treated with basal insulin," *JAMA*, vol. 325, no. 22, p. 2262, jun 2021.

[3] Z. Mian, K. L. Hermayer, and A. Jenkins, "Continuous glucose monitoring: Review of an innovation in diabetes management," *The American Journal of the Medical Sciences*, vol. 358, no. 5, pp. 332–339, nov 2019.

[4] M. J. Khoury and J. P. A. Ioannidis, "Big data meets public health," *Science*, vol. 346, no. 6213, pp. 1054–1055, nov 2014.

[5] I. Ortiz-Gómez, V. Toral-López, F. J. Romero, I. de Orbe-Payá, A. García, N. Rodríguez, L. F. Capitán-Vallvey, D. P. Morales, and A. Salinas-Castillo, “In situ synthesis of fluorescent silicon nanodots for determination of total carbohydrates in a paper microfluidic device combined with laser prepared graphene heater,” *Sensors and Actuators B: Chemical*, vol. 332, p. 129506, apr 2021.

Chapter 2

Materials and Methods

2.1 Novel materials

As stated in Chapter 1, the use of novel materials is a key point to develop flexible electronics devices. These flexible electronics allow a better integration of devices with the user. The use of these materials also introduces fabrication advantages, especially in terms of ease of fabrication and low cost. In this section the two main advanced materials used in this Thesis are presented, which are Laser Induced Graphene (LIG) and conductive pastes for printed electronics.

2.1.1 Laser Induced Graphene

Since it was discovered, graphene has aroused great interest due to its electrical and physical properties [1]. It has an extremely high conductivity and high specific strength. However, obtaining those characteristics requires a perfect crystalline graphene, which is difficult to create and extremely expensive. These drawbacks have driven the research on fabrication alternatives and the discover of graphene derivatives materials. Two of those alternatives are reduced Graphene Oxide (rGO) and LIG.

The use of rGO allows to obtain graphene in a cheaper way. This method parts from Graphene Oxide (GO) which is later reduced through chemical or thermal methods. This last method is attractive for flexible electronics, because the source of heat can be a laser. Using a laser to heat GO allows to apply it locally, so it is possible to "print" patterns of rGO in a layer of GO. As the GO is a dielectric material, it is thus possible to create graphene circuits using the laser patterning. This method makes use of very

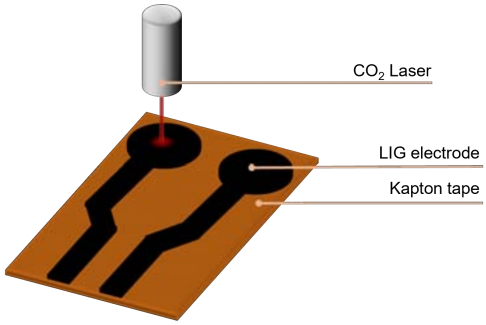

Figure 2.1: Scheme of the fabrication of LIG.

cheap fabrication machinery for the reduction process, basically a laser, but obtaining GO is still a complex method

Another technique to create graphene is the so called LIG. This method also uses a laser, but in this case a variety of materials can be used as base. The use of a laser over a material with high content of carbon transform this material into low-quality graphene, which has a reasonable conductivity to use it in flexible electronics. One of the most interesting materials to obtain LIG is Kapton®. This plastic is a polyimide with high carbon content that can stand high temperatures. Using a laser with enough power, the first a thin layer of the Kapton® is ablated and transformed in graphene, as Figure 2.1 shows.

For the work developed in this Thesis, a CO_2 laser Rayject 50 from Trotec has been used [2]. This laser has a maximum power of 30 W. The process to create these electrodes has been optimized with this laser to obtain a sheet resistance around 360 Ω/cm^2. The laser power needed to obtain this resistance is 2.4 W, with an engraving speed of 0.15 m/s. In Figure 2.2 a SEM image of the resulting material is shown. The difference between the pristine Kapton® and the ablated zone is easily noticeable, as the ablated zone is indeed much more irregular. Additionally to the conductivity, these irregularities provide the structure of high porosity as it is noticeable in the detail of Figure 2.2

2.1.2 Printed electronics

The other alternative for the development of flexible electronics is printed electronics. This field is based on the use of traditional impression techniques, such as screen printing, ink-jet, spray coating or rotating printing, to imprint electronic circuits. The first advances in this field came with the

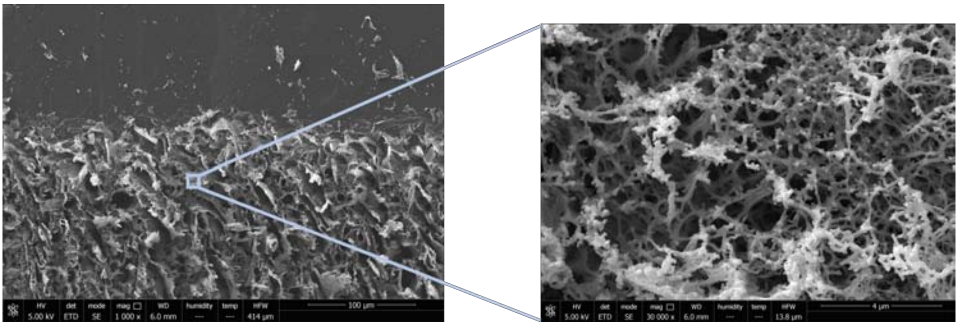

Figure 2.2: SEM image of the boundary of an ablated section of kapton (left) and detail on the structure (right).

development of conductive inks, usually based on carbon and silver chloride. However, the advances on organic chemistry provide a wide offer of conductive polymers like, for example, poly(3,4-ethylenedioxythiophene) (PEDOT), Polyaniline (PANi) or Poly-Phenylene Oxide (PPO). This variety of printable organic materials is not only limited to conductive inks, but they are also available for sensors, solar cells or Thermo-Electric Generator (TEG). In this work carbon and silver chloride inks have been used. The carbon paste used is C-220 from Applied Ink [3] and the silver one is EDAG 6038E SS E&C silver/silver chloride paste from Loctite (Henkel)[4].

Another widely used method to print electronics is spray coating. This system can be applied directly as spray or with a mask to draw more accurate patterns. This technique is more versatile than the others as any pattern can be printed without changing any part of the system. In fact, high-precision robotic arms are able to print in this way. The most usual system sprays the material using compressed air, which atomizes the material as it passes through a small nozzle. The atomization of inks is key for a good result so the viscosity of inks for spray is the limiting factor for the available materials. In this Thesis, spray coating has been used for organic materials because it allows a good control of the layer thickness.

Printed electronics have several advantages over traditional fabrication techniques. They allow using conventional and widely known printing techniques that are oriented to high throughput production, so they can achieve a high production rate of circuits, sensors, or other devices with low cost and standard fabrication machinery. Furthermore, different printing methods allow the use of a wide variety of substrate materials like textile, plastic or paper. Screen printing is one of the most extended techniques in printed electronics as it offers a compromise between the high flexibility of ink-jet printing and the fast production of rotary printing. Changing the design in

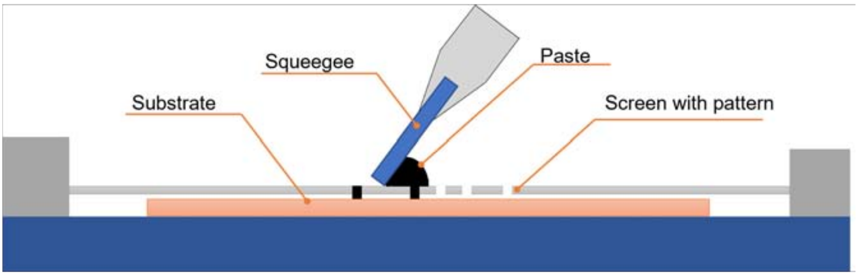

Figure 2.3: Schematic representation of the screen printing process.

screen printing just requires to produce a new screen while for rotary printing a new roller is required, which is more expensive and complex. On the other hand the process is slower than printing in a rotary printer.

Screen printing consist of a mask on which the ink is spread to transfer the pattern in this mask to the substrate. This mask is also known as screen, and it is made of a metallic wire mesh. Depending on the pattern and the ink or paste used, the screen can have different mesh densities, *i.e.*, different width in the wires or different distances between the wires. These two parameters will create larger or smaller holes for the ink to pass through. Higher density meshes, *i.e.*, with smaller slots for the ink, provide more accurate patterns, but it will be more difficult for the ink to pass through. To create the pattern, this mesh is covered with a UV sensitive emulsion that covers all the slots in the screen. Then, the emulsion is exposed selectively to UV light using a mask hardening the non-printing areas of the mesh. After washing the screen, the pattern is created, and it can be used for printing. Figure 2.3 shows schematically the process of screen printing.

2.2 Reconfigurable electronics

In this Thesis, reconfigurable electronics has been demonstrated to be a great option for hybrid electronics (combining flexible and rigid electronics). In this work PSoC systems have been used in the developed prototypes. This type of system integrates in one chip analog and digital reconfigurable capabilities along with an ARM processor. Specifically, PSoC 5LP and PRoC BLE are the central elements of the devices created in this Thesis.

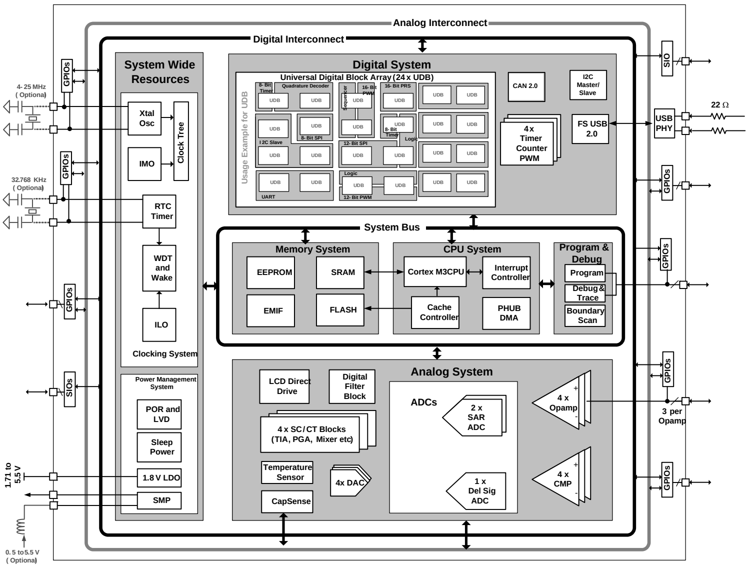

Figure 2.4: Internal architecture of PSoC 5LP devices.

2.2.1 PSoC 5 LP Devices

PSoC 5 devices are made up of a FPGA-like block with 24 Universal Digital Blocks (UDB) and different dedicated blocks (PWM, I2C, USB, etc.), a FPAA-like area with different analog blocks such as comparators, op-amps, etc., and an ARM Cortex-M3 CPU core with 64 KB of SRAM [5] memory. Figure 2.4 shows an overview of the PSoC 5 architecture. As it can be seen, it is divided into three main blocks and an additional one for synchronization and power supply.

As detailed above, the digital subsystem is based on UDBs whose architecture is shown in Figure 2.5. As it can be seen this part of the system is composed mainly by two parts: two Programable Logic Device (PLD) blocks and a datapath, similar to the one in a CPU. PLD blocks are used to implement logic expressions, state machines, sequencers, look-up tables, and decoders with a maximum of 12 inputs and 4 outputs in each PLD block. However, larger blocks can be created using the chaining interfaces available.

The datapath contains a 8-bit Arithmetic Logic Unit (ALU) with associated compare and condition generation logic, as shown in Figure 2.6. This datapath, can be used to for custom functions despite it is optimized to implement embedded functions such as timers, counters, integrator or PWMs. The ALU has 8 basic instructions which are:

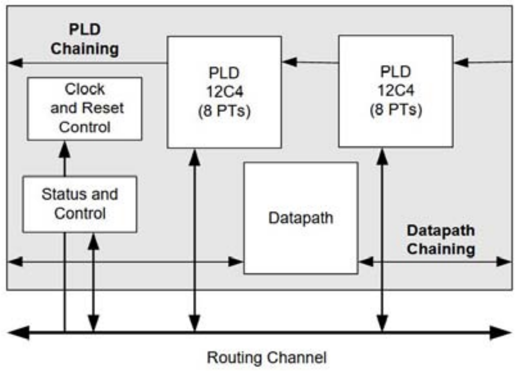

Figure 2.5: PSoC 5 UDB architecture.

- Increment
- Decrement
- Add
- Subtract
- Logical AND
- Logical OR
- Logical XOR
- Pass

At the output of the ALU, shift and mask operations are available as independent functions.

Additionally to these blocks, a dedicated HW accelerator block is available for filtering purposes, called Digital Filter Block (DFB). This block has a dedicated multiplier and accumulator that computes a 24×24-bit multiply-accumulate in one clock cycle. This enables the mapping of Finite Impulse Response (FIR) an Infinite Impulse Response (IIR) filter without using any CPU resources and in less time than in software implementations. The filters are calculated in the IDE software and configured during the programming process, as shown in Figure 2.7. The input and output operations can also be done without the intervention of the CPU, with the use of Direct Memory Access (DMA) channels. These channels allow the automated movement of data between registers or memory system, for example between the ADC and the DFB and later from the DFB to RAM.

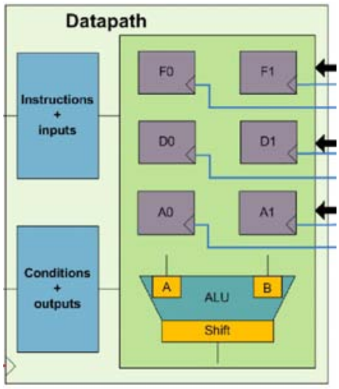

Figure 2.6: ALU architecture.

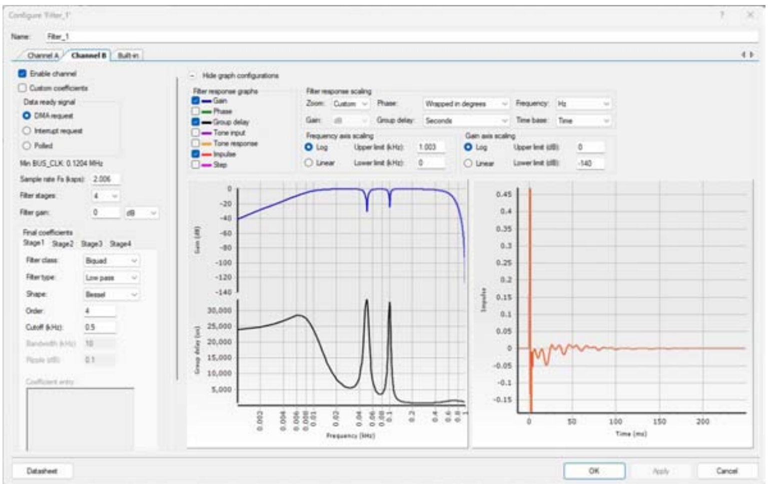

Figure 2.7: Example of configuration of Digital Filter Block.

In the analog subsystem several functions are available, but the most interesting for this work are the sigma-delta ADC and the programmable amplifiers. The sigma-delta ADC is a high resolution ADC with a nominal operation of 16 bits at 48 ksps. The ADC can be reconfigured up to 20-bit resolutions and up to 384 ksps when used with 8-bit resolution. It can operate at differential or single input modes. A wide range of input voltage ranges is also available, the minimum value is $\pm$ 0.64 V while the maximum swing is the supply voltage.

The programmable amplifiers are based on switched-capacitors blocks, which allow various analog functions like OpAmps, Programmable Gain Amplifier PGA or transimpedance amplifiers. In this work OpAmps and PGAs

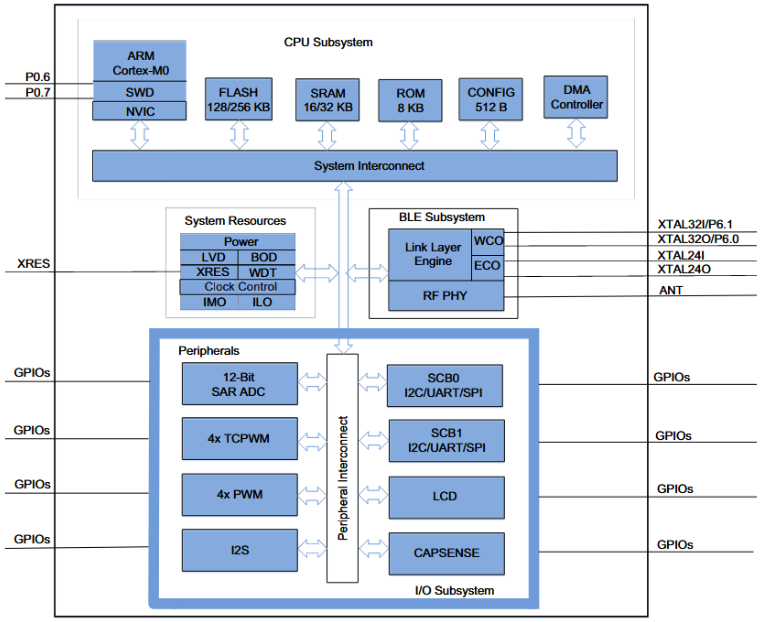

Figure 2.8: Internal architecture of PRoC devices [6].

have been used. OpAmps are used as simple buffers for input or output signals. PGAs are used for complementary amplification to externals amplifiers. PGAs are available in two versions, a normal amplifier and an inverting amplifier, both of them with selectable amplification ranging from 1 to 50 V/V. These blocks have a maximum bandwidth of 6 MHz and a slew rate of 3 V/μs [5].

2.2.2 PRoC BLE devices

PRoC BLE has been also used in this Thesis. This device has been used to cover the lack of wireless capabilities of PSoC 5LP devices. As shown in Figure 2.8, this device does not include programmable hardware as PSoCs do, but it has BLE support [6].

The hardware BLE subsystem consists of the link layer engine and physical layer. The link layer engine implements time-critical functions such as encryption in the hardware to reduce the power consumption, and provides minimal processor intervention and a high performance. The physical layer consists of a modem and an RF transceiver that transmits and receives BLE packets at the rate of 1 Mbps over the 2.4-GHz ISM band. The output power of the radio is programmable from –18 dBm to +3 dBm to optimize

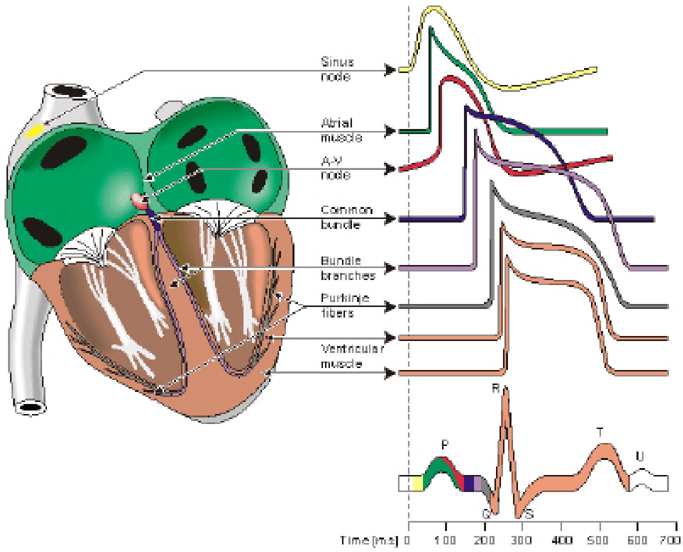

Figure 2.9: ECG composition from the activation of each part of the heart [1].

the current consumption for different applications. The rest of the BLE stack is implemented in firmware.

2.3 Biosignals

Biosignals can be defined as those signals that can be measured from living being. The term is usually reserved for electrical biosignals, but it may refer to other non-electrical biosignals such as respiration rate, pulsioximetry or temperature. This Thesis is focused on the most typical biosignals: Electrocardiogram (ECG), Electromyogram (EMG), Electrooculogram (EOG). In the following, the characteristics and the required acquisition systems are detailed for each of the cited signals.

2.3.1 Electrocardiogram

Analysis of the ECG signal is the most widely used diagnostic technique for cardiac diseases. This waveform is measured on the skin and is caused by the electrical response of the different types of cardiac cells during a cardiac

[1] By Eva Cevera, licensed under CC BY-NC-SA 3.0. Available at https://upload.wikimedia.org/wikipedia/commons/6/6f/Registro_ECG.jpg

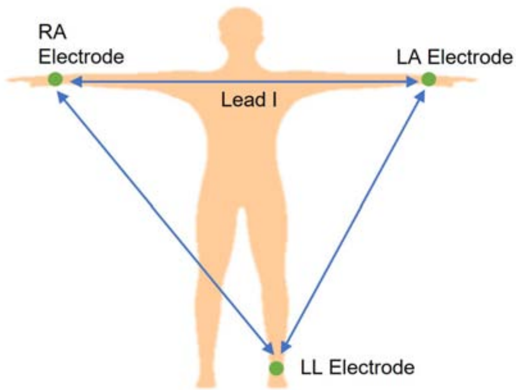

Figure 2.10: Position of electrodes for standards derivations.

cycle. Thanks to this signal, it is possible to detect malfunctions of the heart, which allows the prevention of problems generated by most cardiac conditions [7].

The ECG signal, as shown in Figure 2.9, is the electrical signal produced by the cardiac dipole during the activation of each part the heart. This signal starts at the right atrium, and it is propagated along the heart [8]. The characteristic shape of the signals has six important points in the signal, typically denoted PQRST. The amplitude of these points and the time duration of each phase are the main characteristics for diagnosis. It is clear that having a good and noise-free ECG signal is essential to draw medical conclusions, thus ECG filtering and processing are key tasks.

While acquiring ECG, the positioning of electrodes allows capturing different information of the heart functioning. Each of the positions is called derivation and there are up to 12 derivations for a full ECG acquisition. However, a basic diagnosis can be obtained with the basic standard Leads I, II and III acquired in the extremities as shown in Figure 2.10.

The ECG signal then is acquired in a differential way, so instrumentation amplifiers are used for this purpose. The ECG signals covers a spectrum from 1 to 100 Hz, although most part of the signal information is on the band from 1 Hz to 35 Hz. This means that electrical noise will affect the signal and further filtering at 50-60 Hz is needed. Thus, the typical ECG front-end is composed by an instrumentation amplifier and analog band-pass filtering.

Finally, the third electrode of the setup is used as reference and also to reduce common-mode noise such as 50-Hz interference. To do so, the common mode is feedback to the third electrode (usually attached to one leg) through an inverting amplifier.

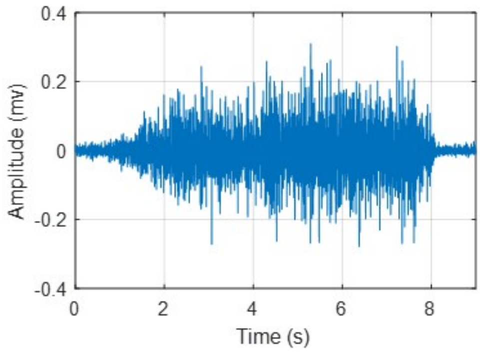

Figure 2.11: Surface EMG signal.

Once acquired, the ECG is treated with Wavelet Transform (see subsection 2.4.2) and then all the peaks are detected following the next procedure:

- **R peak detection**: The R peaks are classified through an threshold method, which is calculated as a 70% of the maximum of the signal
- **Q and S detection**: Once the R peaks are annoted, Q and S peak are found by searching for local minima before and after each detected R peak.
- **P and T detection**: Finally, P and T peaks are found as local maxima after and before S and Q peaks.

ECG processing allows extracting the diagnostic information that the medical personnel requires for diagnosis.

2.3.2 Electromyogram

Electromyogram (EMG) is the signal originated by muscles during contraction. The EMG is generated in each motor unit, which is composed by a motor neuron and the muscle fibers that it stimulates. With each activation, the motor unit generates an action potential that can be measured as an electrical signal. However, to measure a single motor unit requires invasive techniques like the use of needle electrodes to access to a specific motor unit. In this Thesis surface EMG is used, so each electrode captures the action potential of multiple motor units at the same time. This generates a signal like the one shown in Figure 2.11.

EMG signals have multiple applications, and in medicine they are used to diagnose neuromuscular malfunctioning, while for physiotherapists it is a basic tool during rehabilitation. It can be also used in sports, as a way to measure fatigue or to control the correct execution of exercises. Novel applications of these techniques include the use the EMG as an Human-Machine Interface (HMI) to control robots, prosthesis or games for example.

For the acquisition of this signal two electrodes are positioned over the muscle. They should be placed in parallel with the longitudinal axis of the fibers and separated 1 or 2 cm. These two electrodes are connected to a differential amplifier to capture the signals, that have a spectrum from 0 to 500 Hz. The interferences that affect the signal are similar to ECG, so the same feedback system can be used. In this case the filtering is adapted to the spectrum and the Wavelet Transform is also used to process the signal.

As explained above, the surface EMG captures the activation of several motor units at the same time, so it is impossible to carry out specific measurements of the motor unit response. However, from frequency and amplitude parameters of the EMG, it is possible to infer the behavior of the muscle fibers. The most usual analysis is based on the frequency spectrum of the signal, which is directly related to fatigue of the muscle [9]. Variations in the amplitude of the signal are related to the force of the contraction, so a higher amplitude value is generated by a stronger contraction [10].

2.3.3 Electrooculogram

Electrooculogram (EOG) is a technique to measure the movements of the eyes through the electrical signal generated during this movement. The origin of this electrical signal is the permanent potential difference which exists between the cornea and the ocular fundus as shown in Figure 2.12. When moving the eyes, this dipole is oriented to the direction of sight and a potential is generated around the eyes when they are moved [11]. By placing electrodes in the skin around the eyes it is possible to measure this potential and determine the movement, and its direction, of the eyes. At least 4 electrodes, *i.e.*, two differential channels, are needed to determine the position of the eye.

The eye has two type of voluntary movements, saccades and smooth pursuit. saccades are fast movements of the eye to redirect the focus to a specific target, while smooth pursuit movements consist on voluntary movements following a moving target. Despite there are two more involuntary types of movement of the eyes, only the voluntary are studied in this work.

The EOG is a diagnostic tool that can be applied to diagnosis of ocular diseases like the Best Disease [12] or to other studies like attention deficits and others psychological studies [13]. As it happens with EMG, the EOG is

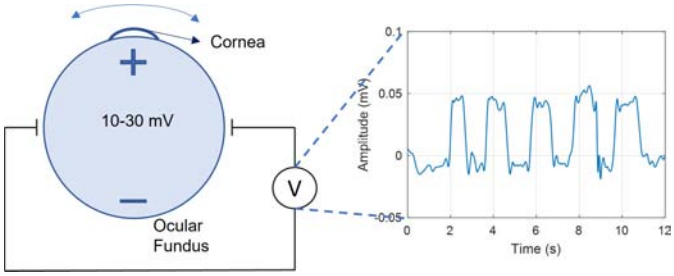

Figure 2.12: Eye potential position and output resulting from eye movement.

suitable for HMIs that can be really useful in cases of total paralysis like in Amyotrhopic Lateral Sclerosis (ALS) or spinal injuries.

The acquisition of EOG is similar to the signals exposed above, but two channels are required at a time. Despite this, the same analog front-end can be used adding a sequential multiplexer at the input to capture both channels. The frequency range of this signal is form 0 to 40 Hz. In this case, line interference is easily removed as it is out of the band of interest

The position of the eyes can be simply derived once the two channels are acquired. Each of the channel represents one of the coordinates of the vector that marks the direction of the sight.

2.4 Signal processing

All acquired signals, despite any previous analog filtering, are affected by artifacts and noise. Thus, further processing is needed after acquisition to correctly extract the characteristics of the acquired signals. The artifacts that will affect the signals used in this Thesis are mainly the following:

- **Baseline wander:** This interference is primarily due to the movement of the electrodes or the breathing of the patient. It is characterized for a low frequency variation of the signal amplitude, between 0 and 0.5 Hz.
- **Higher frequency noise:** This noise is originated mainly due to noise generated by the acquisition circuits themselves and interference from signals with higher frequencies than the band of interest.
- **Electric line interference:** This signal originates from the induction of the electrical signal in the acquisition systems. It is composed of a 50-Hz or 60-Hz sine and its harmonics. This noise will be eliminated

almost completely in the analog front-end of the system. Anyhow, digital filters can improve the reduction of this interference.

To solve these problems, the Wavelet Transform has been used in this work. In the next section, the summarized mathematical fundamentals of this transform and the algorithm used to implement it are detailed.

2.4.1 Wavelet Transform

The Wavelet Transform is one of the so called multi-resolution techniques, since its resolution in time and frequency is not constant. In this way, the Wavelet Transform has high resolution in frequency and low resolution in time for low frequencies, while for high frequencies the frequency resolution is low and the time resolution is high. This transform is based on the use of a function known as wavelet as a base for its transform, in the same way as the Fourier Transform uses sinusoidal signals. The Wavelet Transform represents the signal under analysis as a sum of scaled and translated in time versions of the wavelet. The main advantage of using this representation is that the resolution of the transform is not constant in frequency neither time. For low frequencies, time resolution will be low while frequency resolution is high, the opposite will happen for high frequencies. Figure 2.13 shows schematically this idea versus the time-frequency resolution of the Fourier Transform.

The first concept needed for the Wavelet Transform is to define what is a wavelet. It is defined analytically as a function which accomplishes the following characteristics:

- It should have finite energy, which means that: :

$$E = \int_{-\infty}^{\infty} \mid \Psi(t) \mid^2 dt < \infty \tag{2.1}$$

- For complex wavelets the Fourier Transform should be real and positive.

- It should satisfy the admissibility constant (C_Ψ) criteria, which, being $\hat{\Psi}(f)$ the Fourier Transform of the wavelet, is defined as:

$$C_\Psi = \int_{0}^{\infty} \frac{\mid \hat{\Psi}(f) \mid^2}{f} df < \infty \tag{2.2}$$

  This implies that the frequency spectrum of the wavelet should be finite and $\hat{\Psi}(0) = 0$.

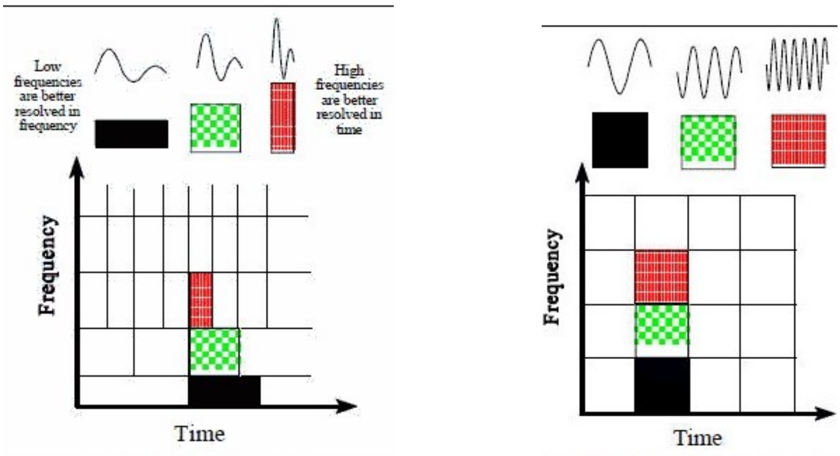

a) Time-frequency resolution of Wavelet Transform. b) Time-frequency resolution of Fourier Transform.

Figure 2.13: Resolution comparative between Wavelet and Fourier Transform.

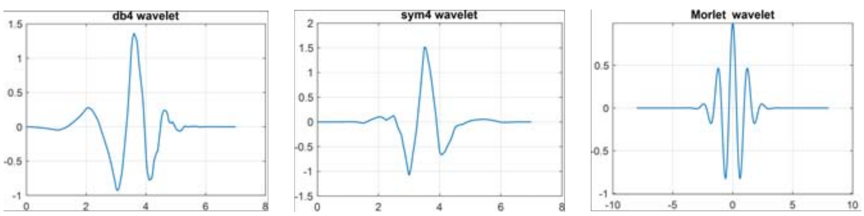

Figure 2.14: Some common wavelet functions.

In summary, a wavelet is a function which starts and ends with value 0, and it is perfectly located in time. Several families of wavelets exist depending on the original wavelet used. The most common wavelets are Haar, Daubechies, Coiflets, Symlet, Biortonormales, Meyer, Mexican hat, Shannon and Morlet. In this Thesis, Daubechies family is the one used. Each family has several subfamilies depending on the fading grade of the wavelet. The most common of this family are db6 and db4, which have fading grades of 6 and 4, respectively [14]. Figure 2.14 shows some examples of wavelets.

The wavelet transform of a function $f(t)$ is defined as:

$$X(a,b) = \frac{1}{\sqrt{|\,a\,|}} \int f(t)\Psi^*_{a,b}(t)dt \tag{2.3}$$

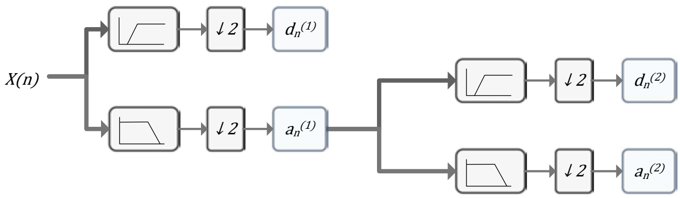

Figure 2.15: Wavelet decomposition algorithm (the symbol ↓ means down-sampling of the signal).

where * denotes complex conjugate and $\Psi_{a,b}(t)$ is the wavelet translated and scaled version defined as:

$$\Psi_{a,b}(t) = \frac{\Psi(\frac{t-b}{a})}{\sqrt{\mid a \mid}} \tag{2.4}$$

With this transform, given a wavelet, it is possible to define any function with the coefficients of scale and translation a, b. Using these coefficients it is possible to rebuild the original function through the Inverse Wavelet Transform (IWT), defined as:

$$f(t) = \frac{1}{\mid a \mid^2} \frac{1}{C_\Psi} \int_b \int_a X(a,b) \Psi^*_{a,b}(t) \mathrm{d}a \, \mathrm{d}b \tag{2.5}$$

All the definitions above are for a continuous domain. In signal processing, this transform is more often used in the discrete domain, as the signals are usually digitalized before their processing. Mallat [15] developed a pyramidal algorithm of the discrete Wavelet Transform, based on a set of filters. The filters are a low-pass filter, obtained from a scaling function and a high-pass filter obtained from a wavelet function. The output of the low-pass filter is known as the approximation vector while the one obtained from the high-pass filter is called the detail vector. Then, in the next step, the approximation vector of the previous decomposition level is downsampled at half the sampling frequency, *i.e.*, the spectrum of the signal is expanded and then the filters are applied again. Thus, the Wavelet Transform of a signal will result in n detail vectors and one approximation vector, being n the level of decomposition used. Figure 2.15 shows schematically the algorithm of the DWT.

For the reconstruction algorithm, also called Inverse Discrete Wavelet Transform (IDWT), the same filters are used but applied in the inverse order, *i.e.* oversampling the vector by the intercalation of 0s between each element

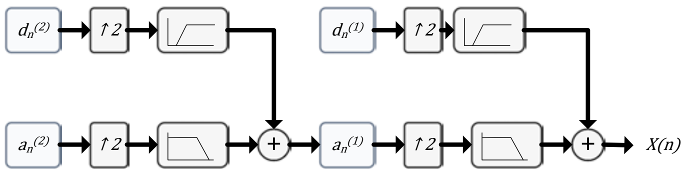

Figure 2.16: Reconstruction algorithm of the signal (the symbol ↑ means oversampling of the signal).

of the vectors and then filtering. The output of each filter is added, obtaining in this way the approximation vector of the upper level. Figure 2.16 shows schematically this process

2.4.2 Baseline wandering elimination and denoising

From the output of the Wavelet Transform, the signal is represented in several vectors of details and one vector of approximations. Modifying these vectors it is possible to alter the reconstructed signal and suppress noise or non-desired interferences on the signal. More concretely, baseline wandering can be suppressed by modifying the approximation vector of the last decomposition level, while high frequency noise will be reduced by modifying the detail vector of the first level [16].

Elimination of baseline wandering

To eliminate the baseline wandering, the wavelet decomposition is performed up to a scaling level L that is determined by the frequency sampling, according to:

$$L = log_2(Fs/2) \tag{2.6}$$

Analyzing the DWT algorithm, it can be seen that as the scaling level increases, the information of the signal contained in the approximation vectors approaches to the lowest frequencies of the signals. The bandwidth covered by the approximation vector of the last level will be the frequencies corresponding to the baseline wandering, which usually is from 0 to 1 Hz. In this way, if the vector of coefficients corresponding to the level L is replaced by 0s, that is, these coefficients are canceled, it will be possible to eliminate the low frequencies that originate this baseline wandering.

Denoising

This section of the processing is intended to suppress the noise of the signal, first estimating the noise level and then eliminating it. For this, in every detail vector all the coefficients under the noise level are modified. The noise level is estimated using a threshold level that, depending on the method used, can be determined as follows [16]:

- **Universal**
$$Th = \sqrt{2log(N)} \tag{2.7}$$
- **Exponential**
$$Th = 2^{\frac{j-M}{2}} \sqrt{2log(N)} \tag{2.8}$$
- ***Minimax***
$$Th = 0.3936 + 0.1829(log(n_j)/log(2)) \tag{2.9}$$

where N is the length of the signal, $j = 1, ..., M$ is the decomposition level, and n_j is the length of the vector of coefficients for level j.

Once the threshold has been obtained following one of the methods described above, it is rescaled according to the standard deviation of the noise. As this deviation is not known, an estimation is made from the median of the coefficient vectors in such a way that $\sigma = median(|d_n^i|)/0.6745$. In this way, when the signal is affected by white noise, it will be enough to estimate the variation in the first level of coefficients. Otherwise, this estimation must be made for each level. Thus, the rescaled threshold is defined as:

$$th_r = \sigma th \tag{2.10}$$

This rescaled threshold can be applied to the coefficient levels in two different ways, the so-called soft thresholding or hard thresholding, that is, by means of a soft or an abrupt threshold. These two thresholding methods are defined by the following expressions:

$$d_n^i = \begin{cases} sign(d_n^i)(|d_n^i| - th_{i,r}) & si\, |d_n^i| \geq th_{i,r} \\ 0 & si\, |d_n^i| < th_{i,r} \end{cases} \tag{2.11}$$

$$d_n^i = \begin{cases} d_n^i & si\, |d_n^i| \geq th_{i,r} \\ 0 & si\, |d_n^i| < th_{i,r} \end{cases} \tag{2.12}$$

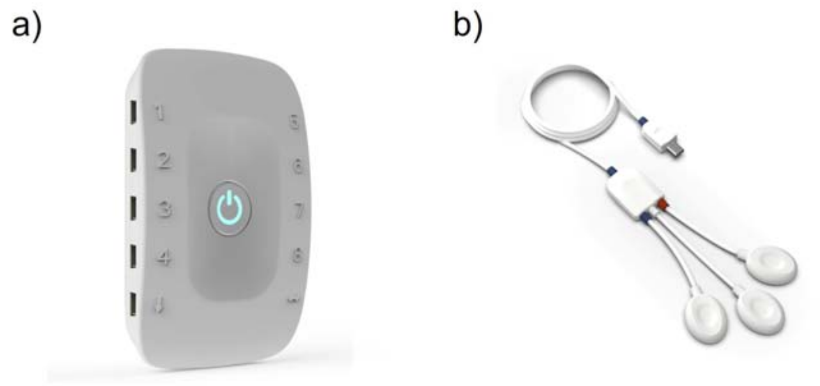

Figure 2.17: Biosignals Plux devices: a) 8 channels acquisition hub; b) ECG sensor.

2.5 Validation and test equipment

2.5.1 Biosignalsplux

Signal acquisitions in this Thesis have been validated with a commercial device. This task was done with the Biosignalsplux acquisition tool. This device is a commercially available instrument oriented to research and education in the acquisition of biosignals. The device used is shown in Figure 2.17a, and it has 8 input channels with the following characteristics [17]:

- Analog ports: 8 generic inputs
- Auxiliary ports: 1 ground & 1 digital I/O
- Resolution: up to 16-bit (per channel)
- Sampling rate: up to 3kHz (per channel)
- Communication: Bluetooth Class II

Several sensors can be connected to this acquisition hub, from electrodes for electrical biosignals to force or respiration sensors. Also, some actuators, such as lights or push buttons, are available. The ECG sensor, shown in Figure 2.17b, has an amplifier and analog filtering integrated. The gain is 1019 V/V and the filter is a band-pass filter between 25 and 100 Hz [18].

These devices include an acquisition software that allows to configure the acquisition parameters and to represent the signal in real time. This software is also able to analyze and extract parameters in real time from the signals acquired.

2.5.2 Laser engraver

The laser engraver used in this thesis is a Rayjet 50. This engraver has a CO_2 laser with a maximum power of 30 W. The laser is moved with a stepper motor that can displace the beam at a speed up to 1.5 m/s. In this work the laser has been used for LIG and to reduce rGO with the parameters shown in Table 2.1.

Table 2.1: Laser parameters used for LIG and rGO.

	Power (W)	Speed (m/s)
LIG	2.4	0.15
rGO	0.6	0.3

2.5.3 Profilometer

Profilometer studies have been carried out with a Dektak XT Bruker. This system takes measurements electromechanically by moving a diamond-tipped stylus over the sample. The user can configure the scan length, speed and stylus force. The profilometer has a manual stage for positioning of samples which can be held by vacuum. The measurements in this work were carried out with the micro-porous vacuum chuck that holds flexible samples flat. The lowest measurement range was always used to measure the samples.

Bibliography

[1] K. S. Novoselov, A. K. Geim, S. V. Morozov, D. Jiang, Y. Zhang, S. V. Dubonos, I. V. Grigorieva, and A. A. Firsov, "Electric field effect in atomically thin carbon films," *Science*, vol. 306, no. 5696, pp. 666–669, oct 2004.

[2] Trotec, "Rayjet 50 grabadora láser," visited 11/11/22. [Online]. Available: https://www.rayjetlaser.com/es/productos/rayjet-50-grabadora-laser

[3] "C-220 safety data sheet," 0, [Online; accessed 2020-10-21]. [Online]. Available: https://kayakuam.com/wp-content/uploads/2020/03/SDS-C-220-Carbon-Resistive-Ink-US.pdf

[4] "Safety datasheet edag 6038e," 0, [Online; accessed 2020-10-21]. [Online]. Available: https://mysds.henkel.com/SAP_GATEWAY/odata/SAP/YPSSWH_DOO_SRV//DocContentSet(Appid='YPSSW_SDSUA',Matnr='000000000001837601',Matnrcomp='',Subid='000000487422',Subidcomp='',Sbgvid='MSDS_UT_US',Laiso='EN')/DocContentData/$value

[5] Cypress, *PSoC 5LP: CY8C58LP Familiy Datasheet*, Infineon Technologies. [Online]. Available: https://www.infineon.com/dgdl/Infineon-PSoC_5LP_CY8C58LP_Family_Datasheet_Programmable_System-on-Chip_(PSoC_)-DataSheet-v15_00-EN.pdf?fileId=8ac78c8c7d0d8da4017d0ec547013ab9

[6] I. Technologies, *PRoC BLE: CYBL1XX7XFamily Datasheet*, 2016. [Online]. Available: https://www.mouser.com/datasheet/2/100/001-95464_PRoC_BLE_CYBL1XX7X_Family_Datasheet_Prog-1085717.pdf

[7] J. Burnett, "The origins of the electrocardiograph as a clinical instrument," *Medical History*, vol. 29, no. S5, pp. 53–76, 1985.

[8] J. G. Webster, *Medical Instrumentation: Application and Design.* John Wiley & Sons Inc, Feb. 2009. [Online]. Available: https://www.ebook.de/de/product/6279970/john_g_webster_medical_instrumentation_application_and_design.html

[9] H. A. Yousif, A. Zakaria, N. A. Rahim, A. F. B. Salleh, M. Mahmood, K. A. Alfarhan, L. M. Kamarudin, S. M. Mamduh, A. M. Hasan, and M. K. Hussain, "Assessment of muscles fatigue based on surface EMG signals using machine learning and statistical approaches: A review," *IOP Conference Series: Materials Science and Engineering*, vol. 705, no. 1, p. 012010, nov 2019.

[10] R. Merletti and D. Farina, Eds., *Surface Electromyography : Physiology, Engineering, and Applications.* John Wiley & Sons, Inc., apr 2016.

[11] "The mcgill physiology virtual lab," visited 10-11-2022. [Online]. Available: https://www.medicine.mcgill.ca/physio/vlab/Other_exps/EOG/eogintro_n.htm.

[12] D. J. Creel, "The electrooculogram," in *Clinical Neurophysiology: Basis and Technical Aspects.* Elsevier, 2019, pp. 495–499.

[13] F. Latifoğlu, M. Y. Esas, and E. Demirci, “Diagnosis of attention-deficit hyperactivity disorder using EOG signals: a new approach,” *Biomedical Engineering / Biomedizinische Technik*, vol. 65, no. 2, pp. 149–164, apr 2020.

[14] I. Daubechies, “Ten lectures on wavelets,” 1992.

[15] S. G. Mallat, “A theory for multiresolution signal decomposition: the wavelet representation,” vol. 11, pp. 674–693, 1989.

[16] E. Castillo, D. Morales, G. Botella, A. García, L. Parrilla, and A. Palma, “Efficient wavelet-based ecg processing for single-lead fhr extraction,” *Digital Signal Processing*, vol. 23, no. 6, pp. 1897–1909, 2013. [Online]. Available: http://www.sciencedirect.com/science/article/pii/S105120041300153X

[17] *8-Channel biosignalsplux HubDatasheet*, Biosignals Plux. [Online]. Available: https://support.pluxbiosignals.com/wp-content/uploads/2021/10/biosignalsplux-8-Channel-Hub-Datasheet.pdf

[18] *Electrocardiography (ECG)Sensor Datasheet*, Biosignals Plux. [Online]. Available: https://support.pluxbiosignals.com/wp-content/uploads/2021/10/biosignalsplux-Electrocardiography-ECG-Datasheet.pdf

Part II

Publications

Chapter 3

Wearable System for Biosignal Acquisition and Monitoring Based on Reconfigurable Technologies

Víctor Toral[1], Antonio García[1], Francisco J. Romero[1], Diego P. Morales[1], Encarnación Castillo[1], Luis Parrilla[1], Francisco M. Gómez-Campos[1], Antonio Morillas[2], Alejandro Sánchez[3]

1 – Department of Electronics and Computer Technology, University of Granada 18071 Granada, Spain

2 – Hospital Alta Resolución de Guadix, 18500 Guadix, Spain

3 – Mando de Adiestramientro y Doctrina, Ejercito de Tierra, 18010 Granada, Spain

Published in Sensors 2019, vol. 19(7), art. 1590

- Received: 25 February 2019; Accepted: 29 March 2019; Published: 2 April 2019
- DOI: 10.3390/s19071590
- Impact factor: 3.367
- JCR Rank: 77/266, category "Engineering, Electrical Electronic" (Q2)

Wearable System for Biosignal Acquisition and Monitoring Based on Reconfigurable Technologies

Abstract: Wearable monitoring devices are now a usual commodity in the market, especially for the monitoring of sports and physical activity. However, specialized wearable devices remain an open field for high-risk professionals, such as military personnel, fire and rescue, law enforcement, etc. In this work, a prototype wearable instrument, based on reconfigurable technologies and capable of monitoring electrocardiogram, oxygen saturation, and motion, is presented. This reconfigurable device allows a wide range of applications in conjunction with mobile devices. As a proof-of-concept, the reconfigurable instrument was been integrated into ad hoc glasses, in order to illustrate the non-invasive monitoring of the user. The performance of the presented prototype was validated against a commercial pulse oximeter, while several alternatives for QRS complexes detection were tested. For this type of scenario, clustering-based classification was found to be a very robust option.

Keywords: Reconfigurable instrumentation; wearable instruments; ECG; oxygen saturation.

3.1 Introduction

Biomedical instrumentation is increasingly relevant, especially in hospital environments, where these instruments are currently a basic tool. Thanks to this type of instrumentation, it is possible to continuously monitor patients and access their historical clinical data. In this context, portable devices present great advantages since they allow this continuous monitoring without requiring the patient to remain hospitalized, unlike clinical instrumentation, which is not easy to transport and requires medical personnel for its configuration and manipulation [1]. The increase rate in the development of this type of devices is steadily growing, as illustrated by the classical Holter monitor, which has now been reduced to a small ear-worn device that monitors several biomedical signals [2]. Therefore, wearable health monitoring systems (WHMS) are increasingly important, while their complexity continues to grow, since a single device has to combine analog circuitry for signal acquisition, advanced digital signal processing, and ever increasing communications capabilities [3]. In addition, the most recent trends in hospital-oriented wearables are the use of new materials and flexible electronics to obtain nanosensors or even implantable sensors to monitor biosignals or chemicals in the body [4, 5, 6].

This growing interest in health wearables is not only related to hospital and clinical applications. Many commercial devices have appeared in recent years, such as the Apple Watch [7], Samsung's range of smartwatches [8], and a variety of activity monitors from companies, such as Garmin [9] or Polar [10]. While for most of them the main objective is to keep track of physical and sports activities and user performance, part of their functionality is based on the monitoring of some physiological parameters. In some cases, they are even accurate enough to be used for medical diagnosis under certain conditions, as shown in Reference [11].

One of the challenges for these devices is the growing interest in the monitoring of professionals [12, 13], especially in high-risk environments where a health issue during the activity can lead to dangerous situations for both worker and coworkers, such as the case of firemen or military personnel [14]. Any physiological information during this type of situation may help prevent further injuries. In addition, in the case of the military, this information is a really valuable asset for commanders, as they can accordingly manage all available troops and assets. Thus, this work presents a health-monitoring wearable based on reconfigurable technologies. The presented device was aimed at the monitoring of intense activity, such as that of military personnel. The system is capable of simultaneously monitoring electrocardiogram (ECG)), oxygen saturation through photoplestymography (PPG), and user activity, thus providing valuable information about the user's physical state during deployment.

Several portable systems have been developed to measure biosignals in recent years. Sopic et al. [15] proposed a touch-based system to measure ECG combined with ICG (Impedance CardioGram), in which the objective was early detection of Congestive Heart Failure (CHF). Another example is Reference [16], in which a PPG acquisition system was developed over eyeglasses and used to obtain heart rate (HR) and pulse transist time (PTT), although this system does require an external ECG and a PPG finger-clip. In Reference [17], a preliminary study of eyeglasses for ECG acquisition was presented, comparing the head-acquired ECG with an arm-acquired standard ECG, although no performance analysis was provided. In Reference [18], a wearable system for the acquisition of ECG was presented. It was designed to be integrated into clothing and communicate through an ad hoc 2.4-GHz radio that requires a specific base station. All these proposals presented different solutions for the acquisition of biosignals, but the system presented in this work acquired different biosignals using a single device that did not interfere with user activity. This was achieved through the combination of state-of-the-art signal processing and low-cost reconfigurable technology, thus providing a completely wearable platform for biosignal acquisition and monitoring in hazardous environments. The reconfigurability of the presented system allows other applications to be implemented using the same hardware scheme [19], or to integrate different communication protocols. In this way, the main contributions of this work may be summarized as: integration of ECG, SpO_2 and motion monitoring into a single device that does not interfere with the activity of the user; ECG acquisition and detection in noisy situations through state-of-the-art digital signal processing; and use of reconfigurable technologies to easily adapt the system to different applications, communication requirements, and scenarios.

The rest of the manuscript is divided into 3 sections. Section 3.2 is devoted to the materials and methods used in this work, including the description of the proposed system based on reconfigurable technologies. The following section illustrates the performance of the system through experimental results for the different sensing channels of the system. The final section summarizes the main conclusions of this work.

3.2 Materials and Methods

This work presents a prototype wearable instrument based on reconfigurable technologies. As stated above, the main aim of this device was the monitoring of high-risk, high-activity professionals, especially military personnel. For this purpose, the system was created around a Programmable System on Chip (PSoC) 5LP [20], which requires a minimum of external circuitry, but for sensors and electrodes, to manage signal acquisition and processing. Moreover, the inherent reconfigurability of this device allows the implementation of different hardware configurations, enabling a number of applications in this and other fields [21, 22, 23, 19]. In this particular case, the instrument simultaneously monitors ECG, oxygen saturation, and user activity, and can communicate through Bluetooth Low-Energy (BLE) to an external mobile device. The following subsections describe in detail each one of the instrument's subsystems.

3.2.1 System Overview

Figure 3.1 shows a conceptual diagram of the presented system. This system was built around a PSoC 5 device, which hosts the main unit, all the control for the different subsystems, and most of the required analog and digital signal processing. The instrument includes three acquisition subsystems:

- Oxygen saturation monitoring: a PPG sensor, controlled by the main unit through a PWM (Pulse Width Modulation) module and its output later processed in the main unit.
- ECG acquisition: an ECG analog front-end for the electrode signals, which are then directly fed to the PSoC 5 for further analog processing, analog-to-digital conversion, and digital processing.
- Motion monitoring: an accelerometer, which communicates via I^2C (Inter-Integrated Circuit) to the main unit.

Beside those sensing subsystems, the presented instrument also includes:

- Bluetooth module for external communications, managed by the main unit through a UART (Universal Asynchronous Receiver Transceiver).
- Power supply subsystem managing the system battery, recharged through a micro USB connector.
- JTAG (Joint Test Action Group) interface for system programming and debugging.

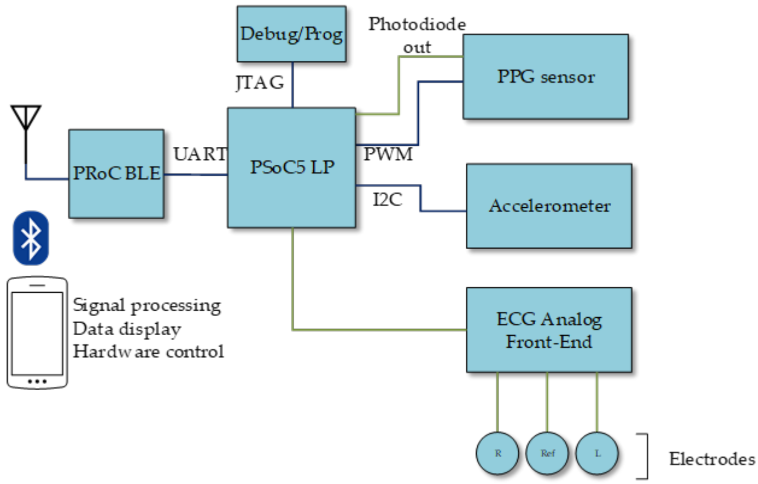

Figure 3.1: Conceptual schematic of the prototype. PSoC = Programmable System on Chip; BLE = Bluetooth Low-Energy; PPG = photoplethysmography; ECG = electrocardiography; PWM = Pulse Width Modulation; UART = Universal Asynchronous Receiver Transceiver; JTAG = Joint Test Action Group.

The reconfigurability of the analog and digital subsystems in the PSoC device allowed efficient implementation of both analog and digital signal datapaths, while also accommodating dedicated digital blocks apart from the microprocessor core. Thus, the PSoC reconfigurable analog cells hosted analog filtering and amplification, as will be detailed later, as well as analog-to-digital conversion. In addition, the reconfigurable digital domain in the PSoC, based in the concept of Universal Digital Block (UDB) [20], can accommodate the UART and I^2C modules required for communication with the Bluetooth unit and the accelerometer, respectively. These UDBs were also used to implement the PWM module. In any case, the reconfiguration capabilities of this technology enable the adaptation of the system to different application scenarios, such as dynamically changing analog parameters like gain or cut-off frequencies, or the implementation of different communication interfaces. At the same time, reconfiguration makes it possible to use the same hardware in different applications, as in Reference [19], where a very similar hardware configuration, but for the amplifier instrumentation and the different communication interfaces, was used to non-intrusively measure the level inside a tank.

Regarding the ergonomics of the system, initial specifications required the integration of the system into the gear of soldiers (combat helmet, protective glasses, earphones of communication equipment, etc.) or pilots (flight helmet, communication equipment, etc.), since prospective applications were referred to the monitoring of military personnel in different simulation, training, and deployment scenarios. Following the input from military personnel, glasses were found to be the best alternative for this proof-of-concept. Therefore, the entire system, including electrodes, sensors, and battery, should be integrated into the glasses. In this way, a PPG sensor could be placed on the temple of the user. However, it is not possible to place ECG electrodes in this same area, since the artifacts from ocular movement make the signal unsuitable for processing. After careful study, the carotid area in the neck was found to be the best place for ECG acquisition while preserving the wearable nature of the system, with a reference electrode placed on the nasal bridge to take advantage of the frame of the glasses. As will be described below, a 3D-printed proof-of-concept frame was developed to host the system.

The different subsystems are described in detail in the following.

3.2.2 Oxygen Saturation Monitoring

The presented device measures oxygen saturation through PPG [24]. This technique makes use of the reflection properties of blood in order to obtain the concentration of oxygen in blood. This is possible thanks to the different reflection properties of oxygenated haemoglobin and deoxygenated haemoglobin [25]. These two, which change their relative concentrations during a cycle of the cardiac and pulmonary functions, have a different response to red (R) and infrared light (IR). This makes it possible to determine the level of oxygen saturation in blood, SpO_2, using a modified version of the Beer–Lambert law [26]:

$$\mathrm{SpO_2} = A + B\frac{V_{AC_R}/V_{DC_R}}{V_{AC_{IR}}/V_{DC_{IR}}}, \tag{3.1}$$

where A and B are calibration constants and V_{AC} and V_{DC} are the components of the waveform obtained by the PPG sensor for both R and IR light, as shown in Figure 3.2.

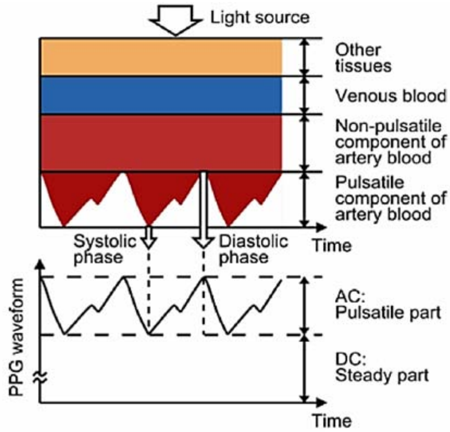

Figure 3.2: Contributing factors to PPG signals and expected waveform [25].

As it can be deduced from Figure 3.2, the heart rate (HR) could also be extracted from the PPG signal, since its basic shape is repeated with each heart beat.

In the presented device, the SFH7060 sensor from OSRAM [27] was used for PPG acquisition. This sensor includes a photodiode and four LEDs: two green, one R, and one IR, although only R and IR LEDs are used. Both the R and IR LEDs, as well as the photodiode, are controlled by the PSoC 5 with a PWM module, which controls the activation time of each LED. The LEDs are thus driven through two digital pins. The output of the photodiode is acquired through a TIA (trans-impedance amplifier), whose gain is controlled adaptively thanks to the reconfigurable nature of the system. This allowed compensation of the sensitivity curve of the sensor. Figure 3.3 shows the configuration of this subsystem.

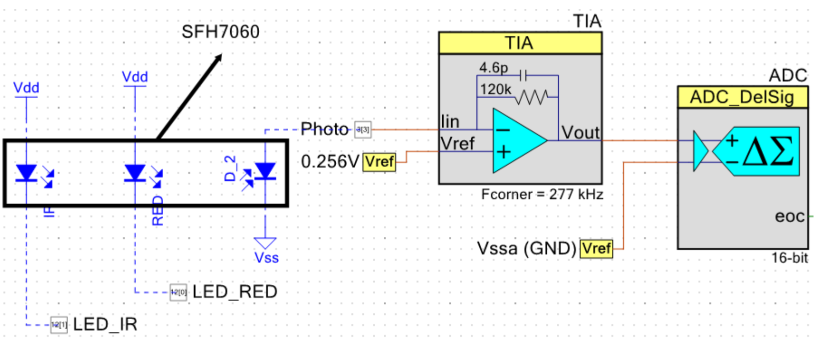

Figure 3.3: Schematic of the PPG subsystem. TIA = Trans-Impedance Amplifier.

The sensor footprint is quite small, only 7.25 × 2.55 mm. It is thus especially suited for these types of wearable applications, even when a development kit version of the sensor has been used for the presented instrument in order to facilitate debugging.

3.2.3 ECG Acquisition

Analysis of the ECG signal is the most widely used diagnostic technique for cardiac diseases. This waveform is measured on the skin and is caused by the electrical response of the different types of cardiac cells during a cardiac cycle. Thanks to this signal, it is possible to detect malfunctions of the heart, which allows the prevention of problems generated by most cardiac conditions [28].

The ECG signal, as shown in Figure 3.4, is the electrical signal produced on the skin by the cardiac dipole generated during the movement of the heart, which is caused by cyclical electrical depolarization and repolarization of the cells of cardiac tissues [29]. Four important points in the signal are typically named QRST and the times between them are one of the main tools for diagnosis. It is clear that having a good and noise-free ECG signal is essential to draw medical conclusions, thus ECG filtering and processing are key tasks, as discussed in the next subsection.

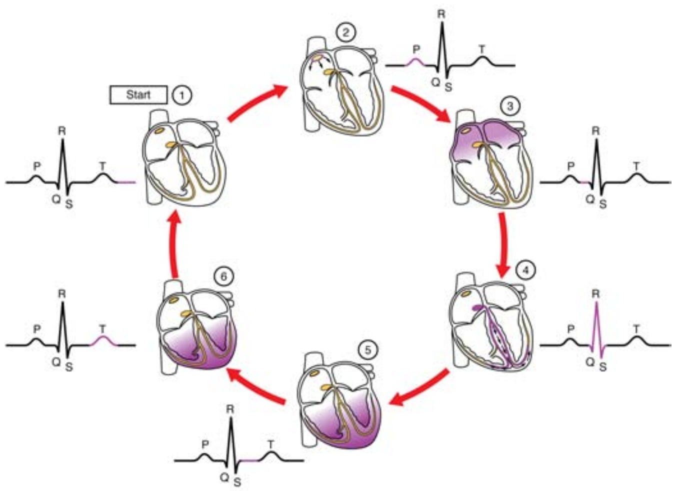

Figure 3.4: ECG waveform composition [30].

ECG is usually acquired using electrodes placed in the so-called Einthoven's triangle [31]. In this way, the three main derivations are obtained depending on the point used as voltage reference. Since the presented device is a prototype for the monitoring of intense activity, the electrodes should be moved to a different position to avoid interference during movement. In this case, the best option for head-mounting both the PPG sensor, placed over the user's temple, and the ECG electrodes is to place these on the neck just over the carotid arteries, with the ECG reference on the nasal bridge. Thanks to the electrical properties of blood [32], it is thus possible to obtain a clean and strong ECG signal from these carotid electrodes. The electrodes used for this prototype are AMBU Blue Sensor VL, from Ambu, and combine an Ag/AgC sensor with wet gel [33].

The ECG acquisition subsystem includes an external INA333 [34] instrumentation amplifier and basic analog filtering, while the rest of the signal datapath is implemented in the PSoC device. Analog filtering is based on two filters, a high-pass filter and a low-pass filter. The high-pass filter is implemented through the reference pin of the instrumentation amplifier [35]. When the low frequency components (below 1 Hz in this case) are introduced in that pin, they will be subtracted from the output signal. In this way, if the low frequency output components are fed back with high gain, it is possible to obtain a high-pass response. To do this, an integrator is used at this pin. As the feedback network needs to amplify the direct current (DC) and low frequency components with high gain, no parallel resistor is placed in the integrator, since limiting DC gain would be a drawback for the filter performance. At the same time, external components are also kept to a minimum. Regarding the low-pass filter, it is a simple resistor–capacitor (RC) network with a cut-off frequency of 100 Hz. The PSoC once again amplifies the acquired signal using a programmable gain amplifier, whose gain can be reconfigured on-the-fly, and finally digitalizes it. Figure 3.5 shows the schematic of the ECG analog front-end, consisting of PSoC Creator blocks and the external instrumentation amplifier and passive components.

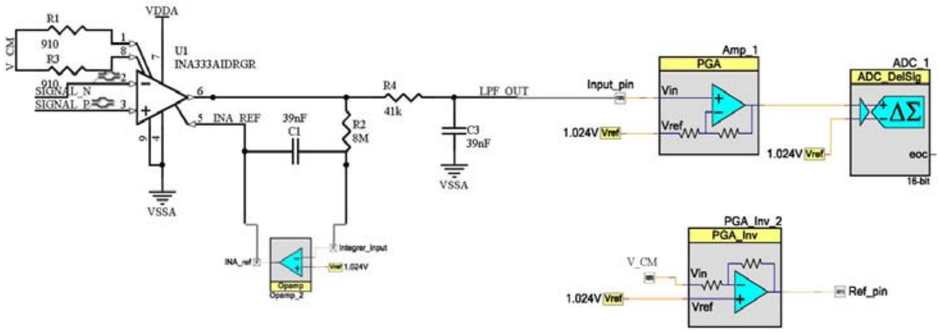

Figure 3.5: ECG acquisition subsystem.

Wavelet-Based ECG Signal Denoising

ECG signals are affected mainly by three types of noise: low frequency noise usually known as baseline wandering, line interferences at 50/60 Hz, and high frequency noise generated by the own electronics and harmonics of the line frequency. Apart from these noise sources, the signal is also affected by artifacts caused by the movement of the subject, while respiration contributes to wandering. The Wavelet Transform was used in the presented instrument to filter and clean the ECG signals, using the same algorithms presented in reference [36] that allow simultaneous reduction of high frequency noise and wandering.

The Wavelet Transform is one of the multi-resolution analysis techniques, which are very useful for signals that vary in time [37] like the ECG. This transform was based on the comparison of the signal to a scaled and time-translated version of a so-called wavelet, which should be adapted to the signal under analysis. In the case of ECG, Daubechies wavelets are usually selected and, in this particular case, the Daubechies wavelet with grade 6, usually known as *db6*, was found to be most appropriate [36].

The discrete version of the Wavelet Transform, DWT (Discrete Wavelet Transform), is based on successive low-pass and high-pass filters combined with decimation of the signal [38]. At each decomposition level, two vectors are obtained, $d_n^{(m)}$ from the high-pass filter and $a_n^{(m)}$ from the low-pass filter. The vector $d_n^{(m)}$ is known as the detail at m level and includes the high frequency information of that decomposition level, while the vector $a_n^{(m)}$ is the corresponding approximation at level m and contains low frequency information. Thus, the higher the number of decomposition levels, the better the frequency resolution is, with the low frequency spectrum expanded at each successive decomposition.

It is possible to suppress low frequency noise (baseline wandering) simply by making zero the approximation at the last decomposed level, while high frequency noise can be removed by modifying any values of the detail vectors of the first levels. This modification [36] can be based on either hard or soft thresholding, zeroing any coefficient below a given threshold and subtracting this same threshold from the remaining coefficients for soft thresholding (those remaining coefficients are unaltered with hard thresholding). The minimum number of levels required for proper processing depends on either the sampling frequency as $L = int(log_2(F_s/2))$, in case no filters are used, or the cut-off frequency as $L = int(log_2(F_{max}))$ in the other case. Therefore, the number of decomposition levels, the thresholding mode, and the threshold are parameters that can be set in the Android application created for the presented instrument, where the wavelet processing is implemented through 12-coefficient finite impulse response (FIR) filters, as determined by the *db6* family.

QRS Complex Detection and HR Determination

Once the ECG signal has been denoised, it is available for performing any feature extraction or further processing. In the case of HR determination, QRS complexes must be located first. For this purpose, two methods have been used: detection based on thresholds, and a method based on the clustering classification of R peaks [39].

The threshold-based method [36] detects an R peak whenever the signal goes over a certain threshold and its distance to the previous R peak is compatible with several time limits, which are set according to the heart rate. This threshold is usually set to 60% of the signal maximum. This is a simple and effective algorithm, but it is very sensitive to noise and amplitude variations of the signal.

On the other hand, clustering detection [39] is based on the classification of so-called candidate R peaks. These candidate points are local maxima followed by a minimum, which are classified through clustering, using amplitude or time×amplitude as the metric. In the presented case, the classification searches for two groups corresponding to R peaks and noise. Additionally, a correction of FP (false positives) and FN (false negatives) further refines the group of selected R peaks, enabling the calculation of the instantaneous heart rate. clustering allows a better detection of QRS complexes since it is less affected by the amplitude variation, while the threshold method is limited by the selected threshold. This threshold is specially critical for low signal signal-to-noise ratios (SNRs), thus reducing the accuracy of the system.

3.2.4 Motion Monitoring

The motion monitoring was based on the MicroElectroMechanical Systems (MEMS) chip MPU6050 [40], which integrates a 3-axis gyroscope and a 3-axis accelerometer. This chip communicates with the PSoC 5 MPU using an I^2C port. The data provided by this sensor can be processed for a variety of applications, especially in the fields the prototype is intended for (military use, law enforcement, etc.), and a simple pedometer was implemented to test the functioning of the sensor and debugging its interface. The algorithm is based on the detection of zero crossing, since the shape of the acceleration signal is similar to that of a sinusoid, and each cycle represents a step. In order to refer the acceleration signal to zero, it is adapted using the mean value as reference. Thus, once a reference crossing is detected, the system checks whether the time from the previous detected step is compatible with a valid step or may be caused by other type of movement. For this particular application, any candidate steps that were closer than 0.2 s to the previous one are discarded. In any case, more sophisticated applications can be developed, from a simple alert when the user is stationary for longer than expected to the automatic counting of ammunition based on the detection of weapon recoil, which requires a more refined processing of the acceleration components.

3.2.5 Proof-of-Concept Prototype

All the subsystems described above have been integrated into a single Prototype Circuit Board (PCB), illustrated in Figure 3.6. The top-side consists mainly of two sections, one devoted to sensors and the PSoC 5 LP (marked in yellow in Figure 3.6), and the other one hosting the power subsystem and battery charging through a micro USB connector (marked in red). The bottom side hosts the communication subsystem and ground planes.

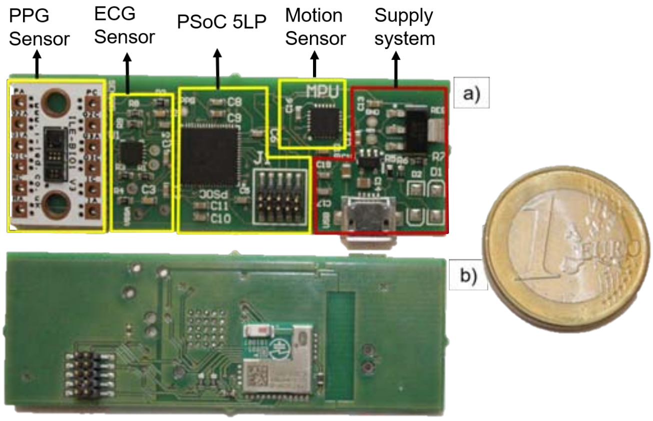

Figure 3.6: Prototype Circuit Board (PCB) of prototype device: (**a**) top side; (**b**) bottom side with the communications system.

Communications Subsystem

Communications were based on BLE. Bluetooth was used in this system because it meets all system requirements in terms of bandwidth and energy consumption. However, alternative communication protocols, such as LoRa, Zigbee, or any other, could be used in this system, depending on the application scenario and providing that the power budget could accommodate them. This change of communication protocols could be easily done thanks to the reconfigurable nature of the system. For this particular application, Bluetooth provides low power consumption while it is widely used in wearable devices. For this, the module PRoC [41] from Cypress Semiconductors was included in the system, which communicates with the main unit through a UART implemented in the PSoC, as described above. Two types of threads are used for communication, depending on whether SpO_2, ECG, or accelerometer information is sent. When transmitting SpO_2, heart rate, or step count information, threads are 5 bytes long, each containing the following information:

- **Byte 1:** type of measurement, whether it is heart rate ("*B*"), oxygen saturation ("*O*"), or steps ("*P*")
- **Byte 2:** hundreds
- **Byte 3:** tens
- **Byte 4:** units

- **Byte 5:** end of thread

In the case of ECG, samples were sent in 24-byte blocks, structured as shown in Figure 3.7. Within each block, only 20 bytes were data, while the rest were used for the initialization, termination, and codification of the thread. Each signal sample was sent using 2 data bytes, so each thread transmitted 10 ECG samples.

Figure 3.7: ECG thread format.

Once these threads were received by the Bluetooth module, they were retransmitted to the mobile device, where the data was decoded and, thus, ready to be used by any apps as required.

Power Subsystem

The power supply system was composed of a small ($19 \times 15 \times 7$ mm), flexible 100-mAh Li-ion battery, which provides 3.7 V, a charger, and a regulator. Thus, the battery is charged by a MCP7383 [42], which is fed through a micro USB connector, while an ADP3338 [43] regulator extracts the energy from the battery and provides a 3.3-V, up to 1-A output to the system. This configuration allowed the system to run for longer than 21 h under a normal operation scenario.

Proof-of-Concept Frame and Mobile App

In order to illustrate the possibilities of the presented instrument, a frame replicating the structure of protective glasses was specially designed and 3D-printed. This frame includes two housings, placed on each side of the head, which are used for the battery and for the prototype PCB, respectively. In addition, the interior of the frame is hollow, so all the wiring for electrodes and power supply are contained in the frame, while also allowing the reference electrode to be placed on the nasal bridge. Additionally, this arrangement directly places the PPG sensor on the user's temple. Figure 3.8 shows an image of the prototype system in the frame during laboratory tests.

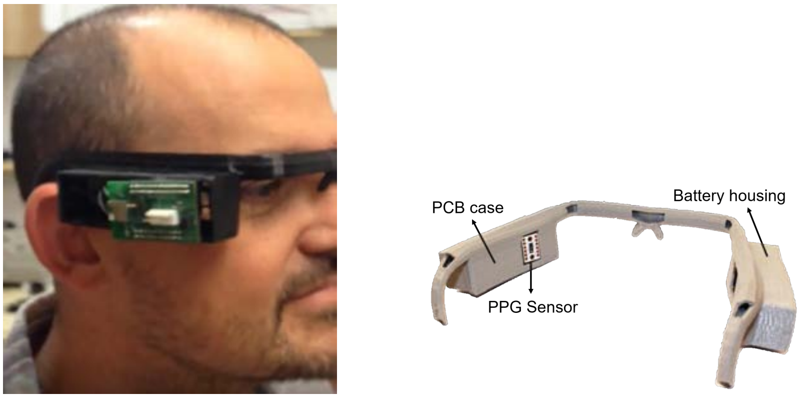

Figure 3.8: Proof-of-concept frame for prototype integration.

This proof-of-concept was completed with the development of an Android app that acts as graphical user interface (GUI) for the prototype system. This app allows configuration of some hardware parameters, such as the amplifier gain or the activation and deactivation of the Analog to Digital Converter (ADC) in the PSoC 5. It also receives and processes the information gathered by the instrument and can transmit that information, or any data extracted from it, to wherever it is required, thanks to the connectivity capabilities of the hosting mobile device. Figure 3.9 shows several screenshots of this app.

Figure 3.9: Android app screenshots.

3.3 Results

The performance of the presented system was evaluated through individual tests of the different sensors included in the system. For this purpose, the performance of the PPG sensing subsystem was compared to that of a commercial pulse oximeter, while ECG acquisition was carried out with different users under different scenarios and evaluated through QRS detection. Finally, as mentioned above, a simple pedometer was implemented to test the functionality of the motion sensor.

3.3.1 PPG Sensor

Data obtained from the system's PPG sensor were compared to those simultaneously obtained with an off-the-shelf clinical pulse oximeter, the Jumper JPD-500 [44]. This was done with twenty sets of 20-second simultaneous measurements from five different subjects, taking the average SpO_2 and HR from each instrument for comparison. Results are shown in Figure 3.10. Most of the readings from the presented system were within the ±3-BPM (beats per minute) range of the pulse oximeter data, with all values in the ±10-BPM range. In the case of oxygen saturation (SpO_2), all measurements but one were in the ±1% range when compared to the clinical pulse oximeter.

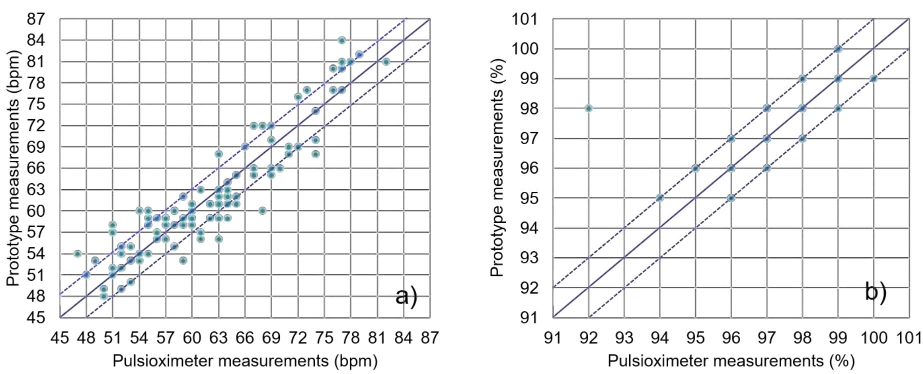

Figure 3.10: Beats per minute (BPM) (**a**) and SpO_2 (**b**) results compared to a clinical pulse oximeter (dotted lines represent ±3-BPM and ±1% deviations, respectively).

3.3.2 ECG Monitoring

The performance of the ECG acquisition system was analyzed with a QRS complexes detection application. For this, the system was tested with seventeen 30-s registers from several subjects. Most of the registers were acquired while the subjects were simulating the usual movements in a flight simulator, as one of the possible applications of the system is the in-cabin monitoring of military pilots. Two additional registers were acquired after the subjects had run up a two-story staircase. Figure 3.11 shows both a raw signal, i.e., the ADC output, and its wavelet-denoised version. As it is shown, the wavelet-based denoising suppresses wandering and removes high frequency noise. It must be noted that the denoising scheme was tuned to six levels of decomposition and universal soft thresholding [36]. All the registers were manually annotated by a cardiologist and the clinical pulse oximeter was used to validate the HR ranges derived from the analysis of ECG registers.

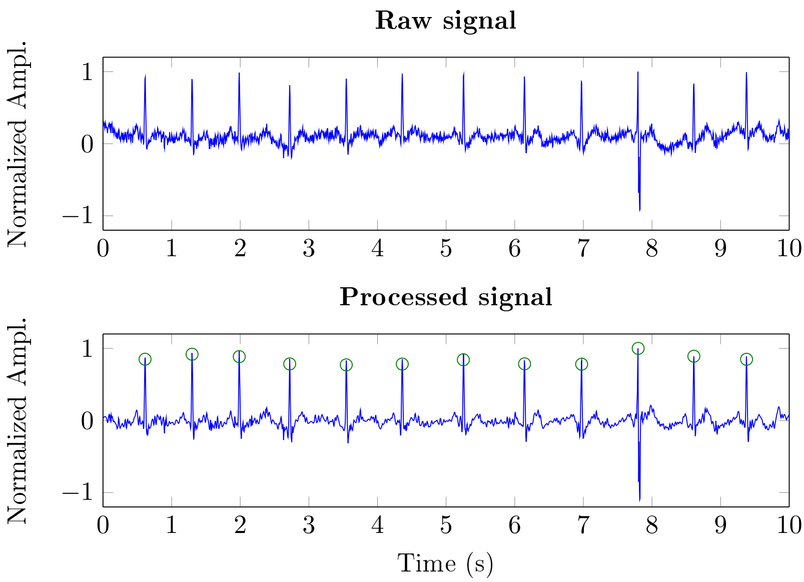

Figure 3.11: Raw and denoised ECG (dots correspond to detected QRS complexes).

In order to assess the extraction algorithm, three performance parameters were used: sensitivity, S_e, positive diagnostic value, PDV, accuracy, A_{cc}, and F_1-measure, which are defined as [45, 46]:

$$S_e = \frac{TD}{TD + FN} \tag{3.2}$$

$$PDV = \frac{TD}{TD + FP} \tag{3.3}$$

$$A_{cc} = \frac{TD}{TD + FP + FN} \tag{3.4}$$

$$F_1 = 2 \cdot \frac{PDV \cdot S_e}{PDV + S_e} = \frac{2TD}{2TD + FN + FP}, \tag{3.5}$$

where TD is the total number of detected QRS complexes, i.e., detected complexes that overlap with manually annotated QRS; FP is the count of false positives, which correspond to detected QRS not present in the manual annotations; and FN is the count of false negatives, which are manual annotations that have not been detected by the algorithm. The performance parameters for the different registers are summarized in Table 3.1 for both threshold-based detection and clustering classification. As shown in Table 3.1, the threshold-based method was not performing adequately for some subjects, especially those resulting in low amplitude registers, while the overall accuracy was limited to 75.41% due to the inherent limitations of this type of algorithms in noisy scenarios (subjects were simulating the behavior of a pilot, with movement artifacts deteriorating the ECG signal). However, clustering classification improved accuracy up to 94.24% for the same registers, while achieving an almost perfect PDV, since the system tended to lose some QRS instead of introducing false positives. This proved the efficiency of this approach for noisy scenarios.

Table 3.1: Results for QRS-complex extraction from ECG registers.

	Threshold							**Clustering**						
Register	**TD**	**FN**	**FP**	**A_{cc}%**	**PDV %**	**S_e%**	**F_1%**	**TD**	**FN**	**FP**	**A_{cc}%**	**PDV %**	**S_e%**	**F_1%**
1	40	3	1	90.91	97.56	93.02	95.24	41	2	0	95.35	100.00	95.35	97.62
2	5	38	2	11.11	71.43	11.63	20.00	41	2	0	95.35	100.00	95.35	97.62
3	40	3	0	93.02	100.00	93.02	96.39	42	1	0	97.67	100.00	97.67	98.82
4	40	3	0	93.02	100.00	93.02	96.39	43	0	0	100.00	100.00	100.00	100.00
5	1	40	1	2.38	50.00	2.44	4.65	40	0	0	100.00	100.00	100.00	100.00
6	6	35	1	14.29	85.71	14.63	25.00	34	6	2	80.95	94.44	85.00	89.47
7	30	16	4	60.00	88.24	65.22	75.00	34	2	0	94.44	100.00	94.44	97.14
8	29	15	0	65.91	100.00	65.91	79.45	41	3	0	93.18	100.00	93.18	96.47
9	33	6	2	80.49	94.29	84.62	89.19	38	1	1	95.00	97.44	97.44	97.44
10	79	2	0	97.53	100.00	97.53	98.75	77	4	0	95.06	100.00	95.06	97.47
11	33	7	0	82.50	100.00	82.50	90.41	36	4	0	90.00	100.00	90.00	94.74
12	34	6	0	85.00	100.00	85.00	91.89	36	4	0	90.00	100.00	90.00	94.74
13	33	7	0	82.50	100.00	82.50	90.41	36	4	0	90.00	100.00	90.00	94.74
14	68	10	2	85.00	97.14	87.18	91.89	78	0	0	100.00	100.00	100.00	100.00
15	35	3	0	92.11	100.00	92.11	95.89	38	0	0	100.00	100.00	100.00	100.00
16	30	6	0	83.33	100.00	83.33	90.91	36	4	0	90.00	100.00	90.00	94.74
17	34	3	1	89.47	97.14	91.89	94.44	37	0	0	100.00	100.00	100.00	100.00
TOTAL	**693**	**212**	**14**	**75.41**	**98.02**	**76.57**	**85.98**	**850**	**47**	**5**	**94.24**	**99.42**	**94.76**	**97.03**

[a] Subjects had previously run up a two-story staircase.

3.3.3 Motion Sensor

As stated above, the motion sensor was tested through the implementation of a pedometer. Thus, tests comprised fourteen registers ranging from 20 to 200 steps by different subjects. Table 3.2 shows the results of the pedometer test. As it can be deduced from the data, the mean error was around 10%, but it must be taken into account that most of this error was derived from the short tests. This was due to the the fact that the initial steps helped calibrate the algorithm, so most of the undetected steps were usually within the first steps of the registers.

Table 3.2: Pedometer test results.

Number of Steps	**Steps Detected**	**Error (%)**
200	188	6
200	178	11
200	206	3
200	196	2
100	83	17
100	98	2
100	100	0
50	36	28
50	54	8
50	48	4
20	14	30
20	16	20
20	16	20
20	20	0
	Mean	**10.78%**

3.3.4 Power and Electric Characterization

Table 3.3 shows power consumption data for the presented system. As stated above, the system includes a 100-mAh battery, so it can operate beyond 2 h 20 min with all modules working simultaneously in non-stop mode. This same battery can supply the system in sleep mode for more than 1200 h. In any case, it must be taken into account that the presented prototype was just a proof-of-concept and was not optimized for energy saving. Moreover, this kind of application scenarios can provide space for larger batteries within the user's gear.

Table 3.3: Power consumption summary for the presented system.

	Consumption (mA)	
Device	**Sleep Mode**	**Active Mode**
CPU@24MHz	0.03	9
Bluetooth	0.002	0.21
INA333	0.05	0.05
PSoC modules	0	12
MPU6050	0	0.5
PPG sensor LEDs	0	20
PPG sensor photodiode	0	0.0012
Total	**0.082**	**42.7612**

The presented system requires 74 mW to perform a 30-s ECG recording, or 105 mW to monitor SpO_2 for 20 s. Thus, it is possible to adapt applications of the presented device to different energy scenarios. For example, the PPG sensor can be used as backup for the determination of HR, since the ECG may be more sensitive to user movement and to noise and interferences and, at the same time, requires more energy (618 μWh vs. 587 μWh). In this way, ECG could be performed only when the user is resting, relying on the motion sensor data, in order to optimize performance and power usage.

3.4 Conclusions

In this work, a low-cost wearable device to monitor ECG, oxygen saturation and activity was presented. The core of the system is a reconfigurable PSoC 5 device, and the instrument was aimed at high-risk, professional applications, such as emergency, law enforcement, or military personnel. The developed system combined different sensors, appropriate signal processing for each sensor subsystem, and Bluetooth communications to achieve a continuous and non-invasive monitoring of the user. A 3D-printed glasses frame was designed to house the instrument as a proof-of-concept for military personnel, while an ad-hoc Android app allowed a mobile device to be used as the user interface for the instrument. The reconfigurable nature of the instrument also allowed some of its hardware parameters to be configured from the app, which could also expand the application scope with enhanced external communications and additional processing and computing capabilities in the mobile device.

The combination of reconfigurable hardware with state-of-the-art signal processing makes this proposal a step forward when compared to other wearable solutions. Thus, the possibility of reconfiguration allows a wide range of applications in different fields without redesigning the system. At the same time, the use of cutting-edge algorithms, such as clustering for QRS classification, allowed the design to overcome traditional limitations of wearable systems caused by noisy application scenarios.

Bibliography

[1] D. I. Fotiadis, C. Glaros, and A. Likas, "Wearable medical devices," *Wiley Encyclopedia of Biomedical Engineering*, 2006.

[2] D. D. He, E. S. Winokur, and C. G. Sodini, "An ear-worn vital signs monitor," *IEEE Transactions on Biomedical Engineering*, vol. 62, no. 11, pp. 2547–2552, nov 2015.

[3] D. D. R. Annalisa Bonfiglio, *Wearable Monitoring Systems*, Springer, Ed. Springer US, 2010. [Online]. Available: https://www.ebook.de/de/product/16204677/wearable_monitoring_systems.html

[4] F. Ershad, K. Sim, A. Thukral, Y. S. Zhang, and C. Yu, "Invited article: Emerging soft bioelectronics for cardiac health diagnosis and treatment," *APL Materials*, vol. 7, no. 3, p. 031301, mar 2019.

[5] H. Lee, T. K. Choi, Y. B. Lee, H. R. Cho, R. Ghaffari, L. Wang, H. J. Choi, T. D. Chung, N. Lu, T. Hyeon, S. H. Choi, and D.-H. Kim, "A graphene-based electrochemical device with thermoresponsive microneedles for diabetes monitoring and therapy," *Nature Nanotechnology*, vol. 11, no. 6, pp. 566–572, mar 2016.

[6] S. Coyle, D. Morris, K.-T. Lau, D. Diamond, F. D. Francesco, N. Taccini, M. G. Trivella, D. Costanzo, P. Salvo, J.-A. Porchet, and J. Luprano, "Textile sensors to measure sweat pH and sweat-rate during exercise," in *Proceedings of the 3d International ICST Conference on Pervasive Computing Technologies for Healthcare*. Institute for Computer Sciences, Social Informatics and Telecommunications Engineering (ICST), 2009.

[7] Apple, "Apple watch," https://www.apple.com/watch/, Visited January 2019. [Online]. Available: https://www.apple.com/watch/

[8] Samsung, “Samsung wearables,” https://www.samsung.com/us/mobile/wearables/, Visited Jaunuary 2019. [Online]. Available: https://www.samsung.com/us/mobile/wearables/

[9] Garmin, “Garmin wearable technology,” https://buy.garmin.com/en-US/US/c10002-p1.html, Visited January 2019. [Online]. Available: https://buy.garmin.com/en-US/US/c10002-p1.html

[10] Polar, “Polar products,” https://www.polar.com/us-en/products, Visited January 2019. [Online]. Available: https://www.polar.com/us-en/products

[11] D. Hernando, S. Roca, J. Sancho, Á. Alesanco, and R. Bailón, “Validation of the apple watch for heart rate variability measurements during relax and mental stress in healthy subjects,” *Sensors*, vol. 18, no. 8, p. 2619, aug 2018.

[12] J. Khakurel, S. Pöysä, and J. Porras, “The use of wearable devices in the workplace - a systematic literature review,” in *Smart Objects and Technologies for Social Good*. Springer International Publishing, 2017, pp. 284–294.

[13] E. Barkallah, J. Freulard, M. Otis, S. Ngomo, J. Ayena, and C. Desrosiers, “Wearable devices for classification of inadequate posture at work using neural networks,” *Sensors*, vol. 17, no. 9, p. 2003, sep 2017.

[14] H. B. Lim, D. Ma, B. Wang, Z. Kalbarczyk, R. K. Iyer, and K. L. Watkin, “A soldier health monitoring system for military applications,” in *2010 International Conference on Body Sensor Networks*. IEEE, jun 2010.

[15] D. Sopic, S. Murali, F. Rincón, and D. Atienza, “Touch-based system for beat-to-beat impedance cardiogram acquisition and hemodynamic parameters estimation,” in *Proceedings of the 2016 Design, Automation & Test in Europe Conference & Exhibition (DATE)*. Research Publishing Services, 2016.

[16] Y. Zheng, B. Leung, S. Sy, Y. Zhang, and C. C. Y. Poon, “A clip-free eyeglasses-based wearable monitoring device for measuring photoplethysmograhic signals,” in *2012 Annual International Conference of the IEEE Engineering in Medicine and Biology Society*. IEEE, aug 2012.

[17] A. Bujnowski, J. Ruminski, M. Kaczmarek, K. Czuszynski, and P. Przystup, "Cardiovascular data analysis using electronic wearable eyeglasses – preliminary study," in *Proceedings of the 2016 Federated Conference on Computer Science and Information Systems.* IEEE, oct 2016.

[18] C. Park, P. H. Chou, Y. Bai, R. Matthews, and A. Hibbs, "An ultra-wearable, wireless, low power ECG monitoring system," in *2006 IEEE Biomedical Circuits and Systems Conference.* IEEE, nov 2006.

[19] A. García, V. Toral, Á. Márquez, A. García, E. Castillo, L. Parrilla, and D. Morales, "Non-intrusive tank-filling sensor based on sound resonance," *Electronics*, vol. 7, no. 12, p. 378, dec 2018.

[20] *PSoC®5LP: CY8C58LP Family Datasheet*, Cypress, Nov. 2018, http://www.cypress.com/file/45906/download.

[21] A. Natarajan and J. Hasler, "Hodgkin–huxley neuron and FPAA dynamics," *IEEE Transactions on Biomedical Circuits and Systems*, vol. 12, no. 4, pp. 918–926, aug 2018.

[22] N. Montealegre, D. Merodio, A. Fernandez, and P. Armbruster, "In-flight reconfigurable FPGA-based space systems," in *2015 NASA/ESA Conference on Adaptive Hardware and Systems (AHS).* IEEE, jun 2015.

[23] A. Salinas-Castillo, D. P. Morales, A. Lapresta-Fernández, M. Ariza-Avidad, E. Castillo, A. Martínez-Olmos, A. J. Palma, and L. F. Capitan-Vallvey, "Evaluation of a reconfigurable portable instrument for copper determination based on luminescent carbon dots," *Analytical and Bioanalytical Chemistry*, vol. 408, no. 11, pp. 3013–3020, feb 2016.

[24] A. Kamal, J. Harness, G. Irving, and A. Mearns, "Skin photoplethysmography — a review," *Computer Methods and Programs in Biomedicine*, vol. 28, no. 4, pp. 257–269, apr 1989.

[25] T. Tamura, Y. Maeda, M. Sekine, and M. Yoshida, "Wearable photoplethysmographic sensors—past and present," *Electronics*, vol. 3, no. 2, pp. 282–302, apr 2014.

[26] E. H. Wood and J. E. Geraci, "Photoelectric determination of arterial oxygen saturation in man." *The Journal of laboratory and clinical medicine*, vol. 34, pp. 387–401, Mar. 1949.

[27] *BioMon Sensor Datasheet*, OSRAM, Apr. 2014, https://dammedia.osram.info/media/resource/hires/osram-dam-2496436/SFH%207060_EN.pdf, Version 1.1. [Online]. Available: https://dammedia.osram.info/media/resource/hires/osram-dam-2496436/SFH%207060_EN.pdf

[28] J. Burnett, "The origins of the electrocardiograph as a clinical instrument," *Medical History*, vol. 29, no. S5, p. 53–76, 1985.

[29] J. G. Webster, *Medical Instrumentation: Application and Design*. John Wiley & Sons Inc, 2009. [Online]. Available: https://www.ebook.de/de/product/6279970/john_g_webster_medical_instrumentation_application_and_design.html

[30] OpenStax College, "Ecg tracing with heart contraction," https://commons.wikimedia.org/wiki/File:2023_ECG_Tracing_with_Heart_ContractionN.jpg, Visited February 2019. [Online]. Available: https://commons.wikimedia.org/wiki/File:2023_ECG_Tracing_with_Heart_ContractionN.jpg

[31] H. A. Snellen, *Willem Einthoven (1860–1927) Father of electrocardiography*. Springer Netherlands, 1995.

[32] R. Pethig and D. B. Kell, "The passive electrical properties of biological systems: their significance in physiology, biophysics and biotechnology," *Physics in Medicine and Biology*, vol. 32, no. 8, pp. 933–970, aug 1987.

[33] *Ambu® BlueSensor L*, Ambu, Apr. 2013, https://www.ambu.com/Admin/Public/DWSDownload.aspx?File=/Files/Files/Downloads/Ambu+com/Cardiology/Long-term_ECG_monitoring_electrodes/BlueSensor+L/Datasheets/IE_L_493100401_V05_0314.pdf. [Online]. Available: https://www.ambu.com/Admin/Public/DWSDownload.aspx?File=/Files/Files/Downloads/Ambu+com/Cardiology/Long-term_ECG_monitoring_electrodes/BlueSensor+L/Datasheets/IE_L_493100401_V05_0314.pdf

[34] *INA333 Micro-Power (50uA), Zero-Drift, Rail-to-Rail Out Instrumentation Amplifier*, Texas Instruments, http://www.ti.com/lit/ds/symlink/ina333.pdf. [Online]. Available: http://www.ti.com/lit/ds/symlink/ina333.pdf

[35] *Getting the most out of your instrumentation amplifier design*, Texas Instruments, 2005, http://www.ti.com/lit/an/slyt226/slyt226.pdf.

[36] E. Castillo, D. Morales, G. Botella, A. García, L. Parrilla, and A. Palma, "Efficient wavelet-based ecg processing for single-lead fhr extraction," *Digital Signal Processing*, vol. 23, no. 6, pp. 1897–1909, 2013. [Online]. Available: http://www.sciencedirect.com/science/article/pii/S105120041300153X

[37] J. Gomes and L. Velho, *From Fourier Analysis to Wavelets.* Springer International Publishing, 2015. [Online]. Available: http://www.ebook.de/de/product/25035026/jonas_gomes_luiz_velho_from_fourier_analysis_to_wavelets.html

[38] I. Daubechies, *Ten Lectures on Wavelets.* Society for Industrial and Applied Mathematics, jan 1992.

[39] E. Castillo, D. P. Morales, A. García, L. Parrilla, V. U. Ruiz, and J. A. Álvarez-Bermejo, "A clustering-based method for single-channel fetal heart rate monitoring," *PLOS ONE*, vol. 13, no. 6, p. e0199308, jun 2018.

[40] *MPU-6000 and MPU-6050 Product Specification*, InvenSense, Aug. 2013, https://www.invensense.com/wp-content/uploads/2015/02/MPU-6000-Datasheet1.pdf, Revision 3.4. [Online]. Available: https://www.invensense.com/wp-content/uploads/2015/02/MPU-6000-Datasheet1.pdf

[41] *EZ-BLE™ Creator Module*, Cypress Semiconductors Corporation, Mar. 2018, document Number: 002-11186 Rev. *G, http://www.cypress.com/file/230691/download. [Online]. Available: http://www.cypress.com/file/230691/download

[42] *MCP73831/2-Miniature Single-Cell, Fully Integrated Li-Ion, Li-Polymer Charge Management Controllers*, Microchip, 2008, https://www.sparkfun.com/datasheets/Prototyping/Batteries/MCP73831T.pdf.

[43] *High Accuracy, Ultralow IQ, 1 A, anyCAP ® Low Dropout Regulator*, Analog Devices, 2005, rev.B, https://www.analog.com/media/en/technical-documentation/data-sheets/adp3338.pdf. [Online]. Available: https://www.analog.com/media/en/technical-documentation/data-sheets/adp3338.pdf

[44] *JPD-500C*, Jumper Medical, Jan. 2019, http://www.jumper-medical.com/enindex.php/pro_view/41.

[45] T. Saito and M. Rehmsmeier, "The precision-recall plot is more informative than the ROC plot when evaluating binary classifiers on imbalanced datasets," *PLOS ONE*, vol. 10, no. 3, p. e0118432, mar 2015.

[46] J. Behar, A. Johnson, G. D. Clifford, and J. Oster, "A comparison of single channel fetal ECG extraction methods," *Annals of Biomedical Engineering*, vol. 42, no. 6, pp. 1340–1353, mar 2014.

Chapter 4

Cost-effective printed electrodes based on emerging materials applied to biosignal acquisition

Víctor Toral[1], Encarnación Castillo[1], Andreas Albretch[2], Francisco J. Romero[1], Antonio García[1], Noel Rodríguez[1], Paolo Lugli[3], Diego P. Morales[1], Almudena Rivadeneyra[1]

1 – Department of Electronics and Computer Technology, University of Granada 18071 Granada, Spain

2 – Institute of Nanoelectronics, Technical University of Munich, 80333, Munich, Germany

3 – Faculty of Science and Technology, Free University of Bozen-Bolzano, 39100, Bolzano, Italy

Published in IEEE Access, vol. 8, pp. 127789-127800

- Received: June 19, 2020; Accepted: July 8, 2020; Published July 13, 2020
- DOI: 10.1109/ACCESS.2020.3008945
- Impact factor: 3.367
- JCR Rank: 94/273, category "Engineering, Electrical Electronic" (Q2)

Cost-effective printed electrodes based on emerging materials applied to biosignal acquisition

Abstract: In this paper flexible printed electrodes applicable to wearable electronics are presented. Using innovative materials as Laser Induced Graphene (LIG) and printed electronics, three type of electrodes based in LIG, silver chloride and carbon inks have been compared during the acquisition of bipotentials as electrocardiogram, electromyogram and electrooculogram. For this last one, a completely new framework for acquisition have been developed. This framework is based in a printed patch which integers 6 electrodes for the EOG acquisitions and an *ad-hoc* signal processing to detect the direction and amplitude of the eye movement. The performance of the developed electrodes have been compared with commercial ones using the characteristics parameters of each signal as comparative variables. The results obtained for the flexible electrodes have shown a similar performance than the commercial electrodes with an improvement in the comfort of the user.

Keywords: Printed Electronics, Flexible Electronics, Electrodes, LIG, Screen Printing, ECG, EOG.

4.1 Introduction

Wearable devices (often simply referred to as "wearables") will play an important role in future paradigms in healthcare [1, 2], as part of the next generation of Internet of Things (IoT)-connected systems. These include the translation of the medical instrumentation to the patients‘ home, with the objective of continuous monitoring to prevent diseases such as cardiovascular conditions [3]. Several challenges arise when trying to achieve this objective, the biggest ones related to communications and acquisition of the biosignals. Regarding communications, security solutions are required since the transmitted data are personal information, while the optimization of IoT networks still remains an issue [4, 5, 6, 7]. On the other hand, the ubiquitous acquisition of signals requires advanced signal processing and wearable devices with capabilities for long-term applications. Biopotential recordings such as Electrocardiogram (ECG), Electromyogram(EMG), Electroencephalogram (EEG) or Electrooculogram (EOG) are basic tools for health monitoring, as they provide valuable information on the health of the user in a non-invasive way. Thus, wearables to acquire this type of signals are key to improve medical systems and patient wellness [8, 9], and can be even used in innovative applications, such as attention monitoring [10].

Flexible electronics are a great tool to achieve the features described above. With these technologies, devices can be conformally adapted to the anatomy of the user without perturbing his/her activity. Thus, flexible electrodes are a key asset for this type of applications, especially for integration in a single device to be attached to the skin and that is able to communicate with healthcare personnel to remotely monitor patients. Traditionally electrical biosignals are acquired using Ag/AgCl wet electrodes. The behaviour of these wet electrodes is well-known and they have been widely studied in signal acquisition. However, they present several problems related to the comfort of the user, especially in cases of extremely sensitive skin and in long-term acquisition [11, 12]. Dry electrodes can mitigate these problems and it is in this field were flexible electronics are of great interest [13]. Moreover, flexible electronics open a wide field for innovative wearable devices [14]. New tools in the field of flexible electronics are currently available, such as printed electronics and, more recently, novel nanomaterials [15, 16, 17].

The most common technologies for printed electronics are screen and ink-jet printing. In the literature several examples of flexible electrodes using printing techniques on different substrates can be found. For example, Geng Yang *et al.* developed an ECG acquisition system over paper substrate using ink-jet printing [18]. Furthermore, Deberner *et al.* developed EEG electrodes printed over polyimide layers. Also, a system for the acquisition of multiple biosignal has been developed by Shustak *et al.*, integrating all the electrodes in a single adhesive patch [19]. Textiles have been also used as printing substrate by Lidón-Roger *et al.* [20] and Xu *et al.* [21].

More recently, graphene-based electronics have expanded the possibilities for flexible devices, since graphene is a biocompatible, conductive material [22]. For example, Celik *et al.* developed ECG electrodes based on chemical vapor deposition (CVD) over Ag/AgCl electrodes [23]. Additionally, Lou *et al.* [24] and Karim *et al.* [25] studied the application of graphene over textiles. Furthermore, Laser-Induced Porous Graphene (LIG) has been also used to create ECG electrodes [26, 27].

In this paper, these two technologies, screen printing and LIG applied to electrodes, are compared to traditional AgCl electrodes for the acquisition of ECG, EMG and EOG signals, since the behavior of this type of traditional electrodes is well-known and they are widely used in real applications. For screen-printing, carbon and silver pastes have been used. In the case of LIG electrodes, the substrate was Kapton, which allows for a cheaper fabrication process than CVD techniques. The electrodes are compared in the acquisition of ECG and EOG signals, using the influence of the electrode on the diagnostic characteristics of each signal as variable of comparison. It must be noted that EOG acquisition with this type of technologies is an innovative solution, demonstrated in this work with an *ad hoc* patch that can enable new possibilities in the use of this technology. As an example of this, measuring the EOG while an activity is carried out is achieved in a more ergonomic way than with traditional electrodes, while also interfering less with the user activity and requiring very simple digital signal processing. In contrast to CVD or stretchable LIG techniques, which require several steps to manufacture the electrode or complex materials as Polydimethylsiloxane (PDMS), the presented electrodes can be fabricated over low-cost materials in just one fabrication step. Furthermore, the required techniques here allow the design of any electrode layout as well as large-scale manufacturing.

The remaining of the paper is structured as follows: section 4.2 provides details of the materials and methods used in this work. The results are then presented and discussed in section 4.3. Finally, section 4.4 summarizes the conclusions derived from this study.

4.2 Materials and methods

4.2.1 Electrode design and fabrication

The presented electrodes were designed with a circular form with a diameter of 10 mm and a small connector wire from the same material as the electrode. The techniques used are screen printing and LIG. In the market there are mainly 3 options for conductive pastes: silver, silver/silver chloride and carbon pastes. In this work, the EDAG 6038E SS E&C silver/silver chloride paste from Loctite (Henkel) [28] was selected, as it is specifically indicated for biosensors and its ratio of silver over silver chloride is 9:1, which results in a sheet resistance of 0.04 Ω/sq. The other selected paste was the carbon paste C-220 from Applied Ink Solutions[29], which is an thixotropic paste for screen printing with a sheet resistance around 16 Ω/sq. All pastes were deposited with a manual screen printer (Siebdruck Versand) using a screen mesh density of 120 threads/cm. Pastes were cured at 115 °C during 10 min. The electrodes are based in a multilayer structure as the one shown in Figure 4.1a. Electrode, wire and isolation layer have been printed over a polyethylene terephthalate (PET) substrate. Later, a stretchable adhesive skin patch and a back cover are added to adhere the electrode to the skin, which results in the electrodes shown in Figure 4.1b. To measure EOG,

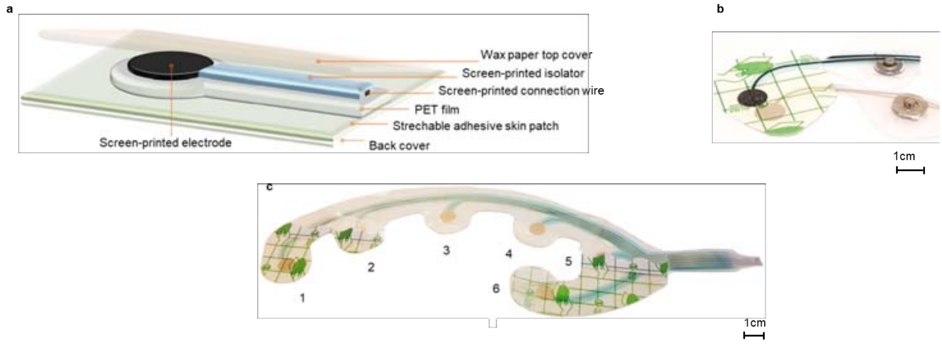

Figure 4.1: Screen printed electrodes. a) multilayer structure used for each electrode. b) Carbon (black) and silver (grey) electrodes for ECG. c) Screen printed patch for terephthalate.

the electrodes have the same multilayer structure but with 6 electrodes integrated in a patch, as Figure 4.1c shows. This patch ensures the proper positioning of the electrodes and avoids cables interfering the user's vision. The designed electrodes have a sheet resistance of 0.062 Ω/cm^2 for silver and 23 Ω/cm^2 for carbon.

In the case of LIG electrodes, Kapton HN polyimide was used to obtain graphene-derived structures. This polyimide, which is produced from the condensation of pyromellitic dianhydride with 4,4-Oxydianiline as cross-linking agent, exhibits an excellent balance of physical, chemical and electrical properties over a wide temperature range. When the laser incises on the Kapton with enough energy to elevate its temperature, it produces a local ablation of the polyimide, thus achieving a conductivity comparable to that of graphene obtained by CVD [18]. Using this technique and the multilayer structure shown in Figure 4.2a, similar electrodes to the ones described above were created with a 2.4-W CO_2 laser. Later, a stretchable adhesive is added along with an AgCl contact for the connection wire, resulting in the electrode shown in Figure 4.2b. In Figure 4.2c, a image of the electrode is shown, where the pattern generated by the laser can be observed. The Raman spectrum is shown in Figure 4.2d, and it can be observed that it is composed of three peaks (D peak: 135 cm^{-1}; G peak: 158 cm^{-1}; 2D peak: 270 cm^{-1}) that confirm the graphene nature of the structure. However, this structure differs from monolayer graphene, as the D and 2D peaks demonstrate. A I_D/I_G ratio close to 1 indicates the presence of defects in the crystalline structure of the graphene. The I_{2D}/I_G ratio confirms the multilayer structure of the graphene generated in the electrode [30]. The sheet resistance of the obtained electrode is 360 Ω/cm^2.

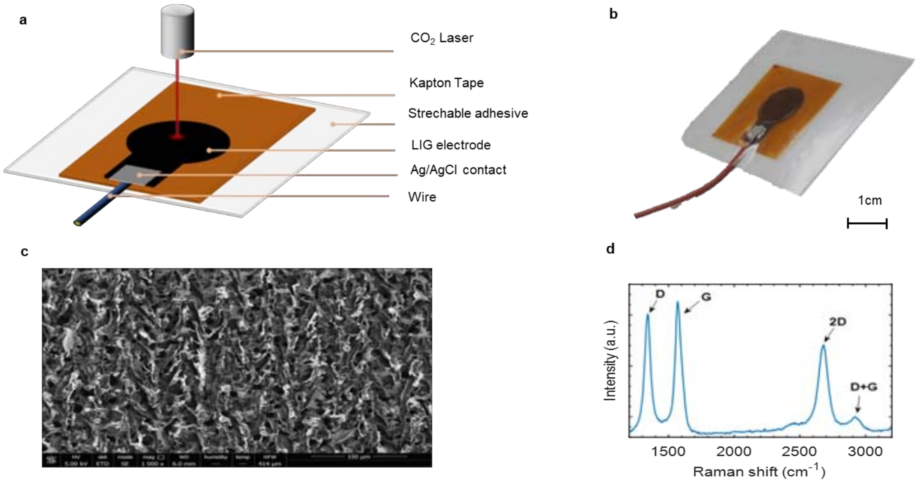

Figure 4.2: LIG electrodes. **a** multilayer structure of the electrode. **b** developed electrode. **c** image. **d** Raman spectrum.

The described electrodes were compared to the commercial EL503 electrodes, manufactured by Biopac [31]. These electrodes are wet type electrodes with an Ag/AgCl contact and 11-mm diameter, along with a 35-mm adhesive patch and an sponge to confine the electrolyte.

In order to study the impedance of the electrodes, they were attached to a metallic plane to contact all the electrode surface. The impedance was thus measured with a Digilent Analog Discovery 2 impedance analyzer between the connection and the metallic plane. For the commercial electrode, electrolyte gel was also added to keep the same conditions than in real applications. In Figure 4.3, the results for all the electrodes are shown. Two main tendencies may be observed: LIG and commercial electrodes tend to have a capacitive behavior while screen printed electrodes have a purely resistive behavior. The one with lower impedance is the silver electrode while the highest is the impedance of the carbon one. Commercial and LIG electrodes have a similar impedance, around 700 Ω.

4.2.2 ECG acquisition

To acquire signals, the sensing platform Biosignalsplux [32], created by PLUX wireless biosignals S.A., was used. This platform allows the acquisition of up to 8 channels of different type of signals. Several probes are available for this device to acquire a wide range of biosignals. In this work, the ECG probes were used to acquire both ECG and EOG signals. These

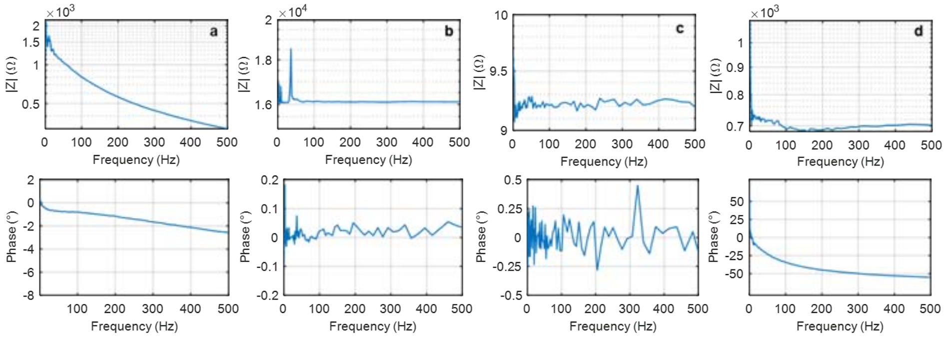

Figure 4.3: Impedance measurement for all the electrodes. a) Module and phase of commercial electrodes. b) Module and phase of carbon electrodes. c) Module and phase for silver electrodes. d) Module and phase for electrode.

probes have a differential input, with a third reference input. Their input range is ±1.5 V, with a gain of 1000 V/V and bandwidth from 0.5 Hz to 100 Hz.

ECG acquisition for all electrodes was carried out during 180 s using Lead 1, which requires to place an electrode on each wrist (the positive electrode is the one on the left arm, LA), and a third reference electrode on the ankle, as shown schematically in Figure 4.4a. All signals were consecutively acquired from two healthy test subjects using the different electrodes. Skin was cleansed with alcohol prior to electrode attachment, in order to remove any dirt or skin secretions that could affect the electrode contact. The electrodes were placed in the same positions in consecutive acquisitions. With this arrangement, the obtained typical ECG signal is shown in Figure 4.4b, where it is possible to observe a baseline deviation, usually refered to as wandering, as well as noise. To process the signal it is essential to suppress these artifacts. In this work, a processing based in the Wavelet Transform is used [33]. This processing obtains very low frequency and high frequency components through wavelet decomposition and later eliminates the bands where noise and wandering are contained. With this, the original signals are denoised, as illustrated in Figure 4.4c. Finally, signals are processed to detect the characteristic points shown in Figure 4.4d, which define the information related to the heart's behavior. The algorithm for this detection and annotation follows these steps, assuming a 1-ksps sampling rate:

1. Detect R-peaks finding maxima separated, at least, by 3000 samples
2. Find minima (Q-peaks) and maxima (P-peaks) 250 ms before the R-peaks

3. Find minima (S-peaks) and maxima (T-peaks) 500 ms after the R-peaks

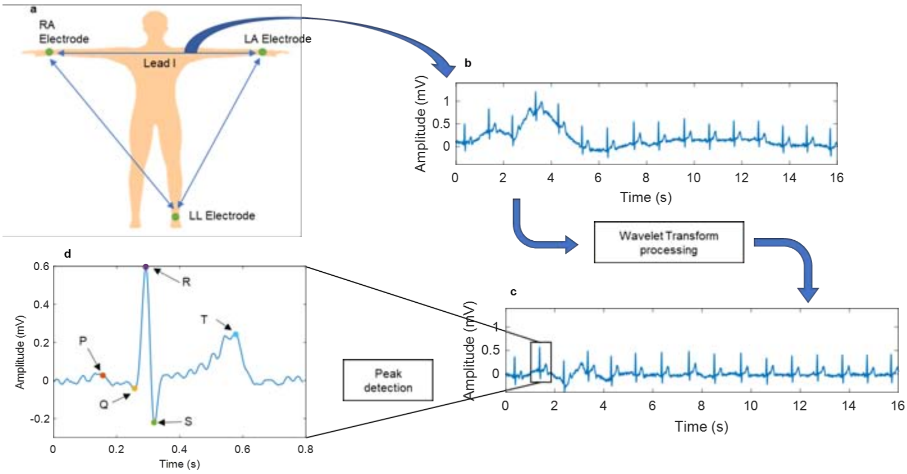

Figure 4.4: ECG acquisition and processing. a) Position of the electrodes and leads.b) Typical signal from Lead I. c) Signal processed with wavelet Transform. d) QRS complex detail.

4.2.3 EOG acquisition

EOG acquisition was carried out with the same system and probes as in the case of ECG. However, in order to perform a more precise comparison, EOG requires an experimental setup that ensures the same amplitude and direction of the eye movement for all measurements. For this purpose, a specific measurement framework has been developed. First, a video (see supporting information) has been created as a guidance for the subject under study. The video consists of a red point describing a certain pattern in the screen, which the subject has to follow with his/her eyes during the experiment, completing the following sequence of movements:

1. Look right for 1 s, then look straight ahead for 1 s, repeat 5 times
2. Look left for 1 s, then look straight ahead for 1 s, repeat 5 times
3. Look up for 1 s, back to straight for 1 s, repeat 5 times
4. Look down for 1 s, back to straight for 1 s, repeat 5 times

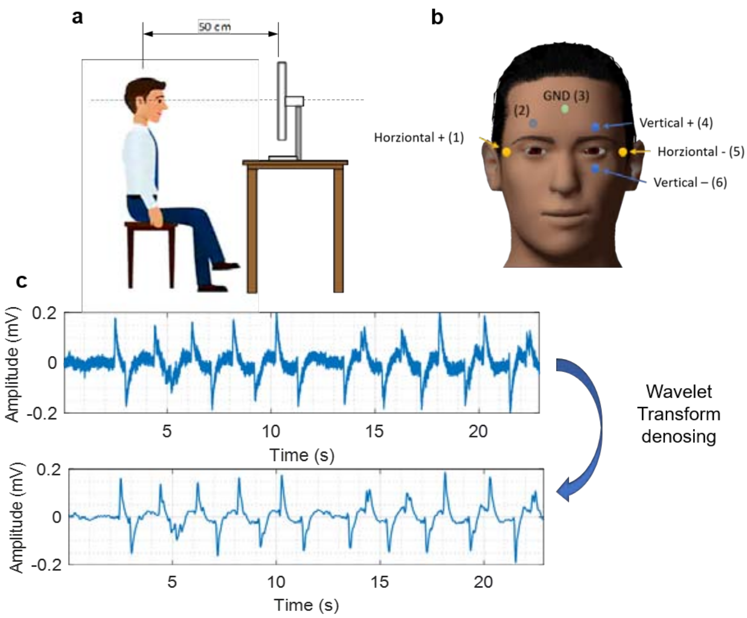

Figure 4.5: ECG acquisition method. a) Position of the user during experiments. b) Positions of the electrodes and signal nomenclature. c) Wavelet denoising.

Additionally to following the video pattern, it is also required that subjects are in the same position with respect to the screen in order to ensure the same movement. Subjects were thus positioned as shown in Figure 4.5a, at 50 cm from the screen and aligning their eyes to the center of the screen. During the tests, winks can affect the subsequent processing of the signal. To avoid this interference, subjects under test were instructed to try to wink only in the intervals between movements, so the interference is easy to detect and can be avoided in the processing. If the user winked during movement, the test was repeated until it was ensured the absence of winks in the processing.

The patch shown in Figure 4.1c ensures the proper location of the electrodes, while two ECG probes, each one acquiring one of the axis of movement, were used. Despite the patch having six electrodes, only five of them were used to simplify the subsequent signal processing. The patch is designed to make the electrodes fall on adequate positions, with two electrodes (4 and 6) for vertical movements and other two (1 and 5) for horizontal movements, while the central electrode (3) is used as reference, as Figure 4.5b shows.

The EOG signals acquired following the same protocol as for ECG. Signals were thus consecutively acquired from two healthy test subjects using the different electrodes, while the skin was cleansed with alcohol to avoid differences in the skin state.

Finally, acquired data are processed using the Wavelet Transform. As shown in Figure 4.5c, the processing is applied only to suppress noise, as the wandering removal is not required and can even be detrimental in EOG signals. Thanks to the Wavelet Transform, almost all the noise is suppressed, thus facilitating the detection of movement direction.

4.2.4 EMG acquisition

EMG signals were acquired with the EMG sensor of Biosignalsplux. This sensor has a differential input with a gain of 1000V/V and a bandwidth from 25 Hz to 500 Hz. The input range is the same as for the other sensor.

Muscles have two types of contractions: isotonic, in which the muscle varies its length, and isometric, in which the muscle does not vary its length. Despite EMG can be measured during both contractions, the isometric contraction is widely used for diagnosis of neurological diseases [34]. Concretely the typical procedure to study the EMG is through Maximum Voluntary Isometric Contraction (MVIC) [35]. In this work, EMG was measured in the biceps brachii at 100% of MVIC. To ensure the isometric contraction of the muscle, the test subject was required to position his elbow at 90° and push up against a fixed table.

The surface EMG measured in this work is a composition of all the evoked potential of the motor units of the muscle [34]. Due to this, the analysis of the signal is usually made by spectrum measurement, like Mean Frequency (MNF) and Median Frequency (MDF), which has been demonstrated to be useful in the study of muscle fatigue [36, 37]. Also, the recruitment of motor units of the muscle, during isometric contraction can be studied through MDF and MNF variations [38].

4.2.5 Comparison parameters

As detailed above, ECG, EMG and EOG signals were acquired, for comparison, with the developed electrodes as well as with the commercial ones. However, a proper numerical comparative must be carried out in order to provide an objective evaluation of the presented electrodes, so two variables have been used to compare the performance of the electrodes in each case.

For the ECG, QRS-complexes detected with the algorithm described above are compared to the annotations made by a cardiologist. The number of false positives (FP), false negatives (FN) and correctly or truly detected (TD) in the determination of QRS-complexes are used to compute the accuracy, A_{cc}, defined as [39]:

$$A_{cc} = \frac{TD}{TD + FN + FP} \tag{4.1}$$

When expressed as a percentage, 100% A_{cc} implies the detection of all the QRS-complexes without any false positives, while a 0% means no detection at all. This variable summarizes the SNR and distortion of the signals, since detection of QRS-complexes using each one of the characteristic points of the signal requires a clear and non-distorted waveform in order to achieve an adequate performance.

In the case of the EOG, the key variable is the direction of the movement. Thus, the comparison variable was the error in the determination of the movement direction. The relative error in the angle is one of the options to compare, but as the expected angles in each direction have different values, the error will be thus relative to different values. With the same absolute error, the relative error will be higher for lower angles, as 0 rad for example. To avoid this, the error is computed relative to a deviation of $\pm\frac{\pi}{4}$ from the expected angle:

$$\varepsilon = \frac{\theta_{expected} - \theta_{measured}}{\pi/4} \tag{4.2}$$

To be consistent with the ECG parameters, the accuracy of the EOG acquisition is defined as:

$$A_{cc} = 1 - \varepsilon \tag{4.3}$$

In this way, a correct determination of direction implies a 100% accuracy while a deviation of $\pi/4$ is represented by 0% accuracy.

For EMG the parameter that has been compared is MDF. Since in this case the real or expected value is unknown, the results from the commercial electrodes will be considered as the reference value. The relative error in MDF for the rest of the electrodes is thus computed as in Equation 4.4.

$$\varepsilon = \frac{MDF_{commercial} - MDF_{measured}}{MDF_{commercial}} \tag{4.4}$$

As with the EOG error and in order to be consistent with ECG values, the accuracy is defined as:

$$A_{cc} = 1 - \varepsilon \tag{4.5}$$

4.3 Results and Discussion

The results obtained from the electrodes presented above and the results of the processing will be compared and discussed in this section. First, the ECG acquisition will be analyzed, later the EOG signals and finally EMG signals.

Although some limitations in the analysis exist, they equally affect all the tested electrodes. The first constrain is the acquisition in static position for both biosignals. This reduces the movement artifacts to low amplitude distortions associated with small movements. Anyway, such artifacts can be eliminated by wavelet processing [33]. These artifacts would increase its amplitude if the subject was moving. Due to this, a stretchable adhesive layer was used to improve adaptability to the skin through an improved skin contact. Furthermore, this contact could be achieved using stretchable substrates and stretchable pastes. However, this option has not been considered due to the size of the electrodes. The second limitation is the lack of acquisition of the smooth pursuit movements in EOG, with only saccadic movement being acquired [40]. Nevertheless, saccadic movements are the most challenging for such electrodes as their frequency spectrum is wider.

4.3.1 Electrocardiogram

In Figure 4.6 a segment of an ECG signal acquired with the new Ag/AgCl electrode is shown. This signal has been processed with the techniques detailed above. It is also possible to observe the characteristic points detected by the algorithm.

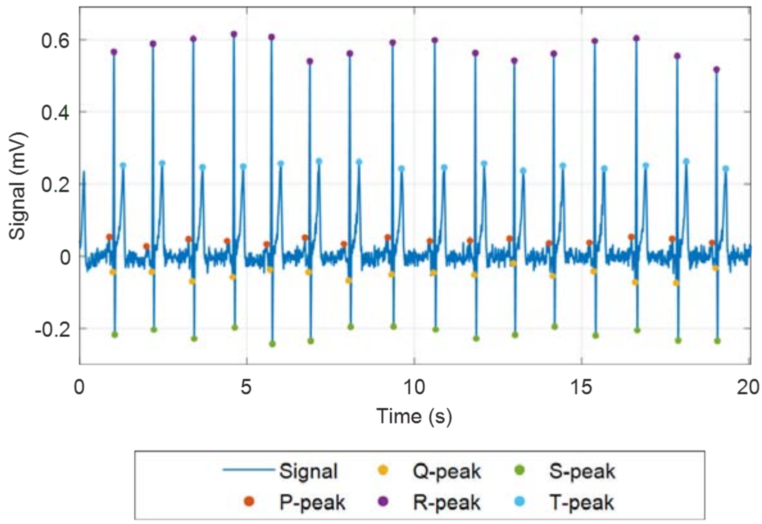

Figure 4.6: ECG signal acquired with the Ag/AgCl electrodes. QRST peaks noted by dots.

Since a graphical comparative of the electrodes is quite difficult with a full 180 s recording, an average QRS has been obtained from the acquired signals. All the QRS-complexes from each recording have been aligned to the R-peak and averaged, resulting in the QRS-complexes shown in Figure 4.7a. The differences are thus quite clear, as the amplitudes are lower for the novel electrodes while the time durations of each peak are equal. The morphology of the signals is the same for all the electrodes but with lower amplitude. In Figure 4.7b and Figure 4.7c the mean amplitudes and mean time distance between peaks are shown, respectively, along with the standard deviation. As it can be seen, the amplitudes are reduced with the different electrodes, while the time segments are similar. It must be noted the variability of the R-S segment for carbon electrodes, due to noise and artifacts during acquisition. In Figure 4.7d, a comparison of a QRS complex without averaging is shown. It can be observed how the amplitudes are similar to the ones obtained with averaging. However, the noise can affect the lowest peaks (P and Q peaks). These results show that the electrodes with lower impedance have higher amplitude except for commercial electrodes, which can be due to a better contact thanks to electrode gel.

This comparison shows interesting results, but it does not cover some issues such as noise. In order to solve this, the accuracy in detection of QRS-complexes is shown in Table 4.1. The results confirm what it was

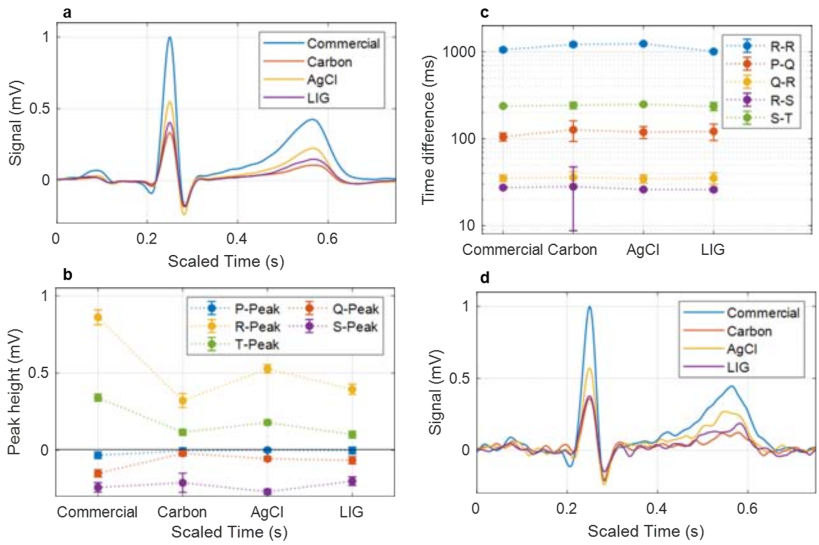

Figure 4.7: ECG comparative. **a)** Mean QRS-complex of each electrode. **b)** Amplitude comparison. **c)** Time segments comparison **d** QRS-complex comparative without averaging.

Table 4.1: Accuracy for ECG acquisitions.

	FP	**FN**	**TD**	**ACC**
Commercial	0	0	840	100.00%
Carbon	18	5	712	96.87%
Ag/Cl	5	0	715	99.31%
LIG	8	0	877	99.10%

expected from the graphical comparison, since the accuracy is reduced with the amplitude of the signals. In the case of carbon electrodes, the accuracy is lower when compared to the other alternatives, which is consistent with the higher variability in amplitudes and time segments previously observed. When compared to the commercial electrodes, a 3.13% reduction in accuracy is the worst case that has been observed.

4.3.2 Electrooculogram

An example of the signals obtained from the acquisition of EOG are shown in Figure 4.8, although for the sake of clarity only “look right” and “look down” movements are shown. Comparing the registers for each material, they are similar in terms of amplitude and pulse duration. As the frequency of these signals is so low and the position of the electrodes is so close to the origin of the signal, the impedance has lower influence. However, AgCl electrodes still shows slightly lower amplitude. In terms of noise, AgCl and LIG electrodes were observed to have worse SNR, despite the fact the Wavelet Transformform was able to correct this lower SNR, as it is shown in Figure 4.8.

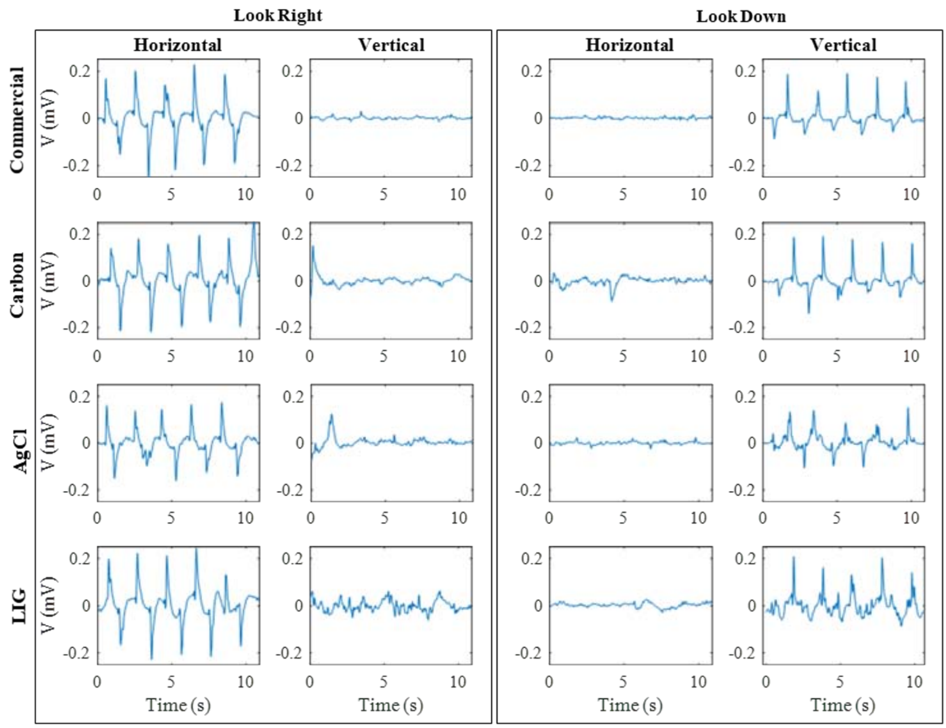

Figure 4.8: EOG signals for different materials and eye movements.

With the two channels acquired, detection of movement is a straight procedure, just composing both channels into a vector that determines the direction and amplitude of the movement. The determination is divided in two parts, first detect the movement in a given direction followed by the opposite direction and, second, detect the amplitude. As in each movement of the eye there will be two contiguous peaks, one for one direction and another one for the opposite, the detection first analyses the first peak sign and then determines the amplitude. The amplitude in this work is determined averaging the amplitude of the five peaks, according to the procedure described above, and normalizing it to their maximum amplitude. With this processing applied to each channel and combining both components in a vector it is possible to determine the direction as shown in Figure 4.9.

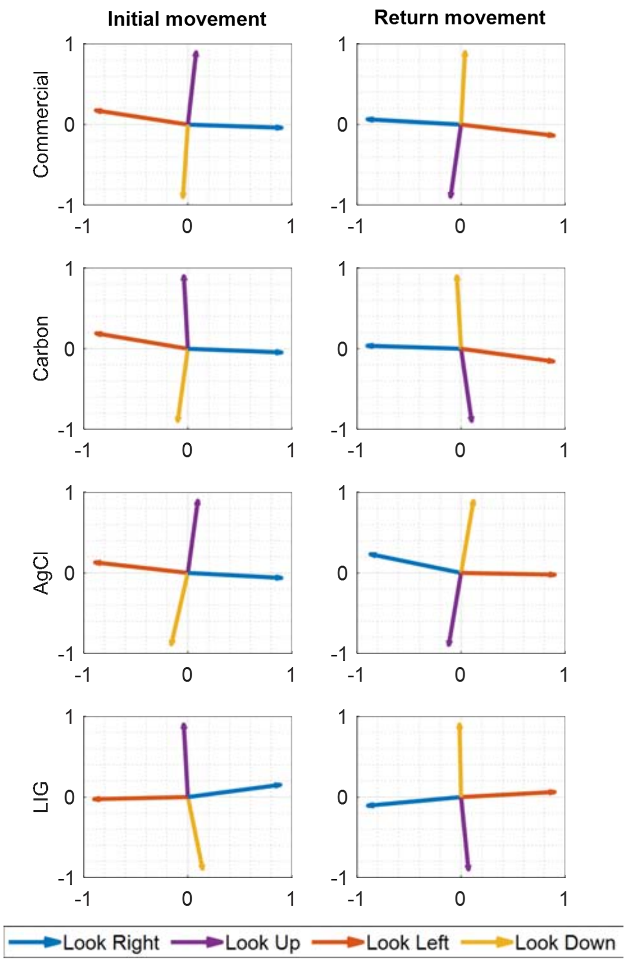

Figure 4.9: Vectors of movement obtained from the processing.

In Table 4.2 the accuracy of the results, obtained as detailed in the Methods section, is shown. The values are higher than 84% in all cases, and up to 87.87% in the best case for commercial electrodes. Among the developed electrodes, LIG electrodes are the closer to the results of the commercial alternative with 87.27% accuracy.

It must be noted that, despite the error, the vectors of movement in one direction and its opposite should be parallel. Thus, any differences in

Table 4.2: Accuracy in the determination of movement direction from EOG acquisitions.

	Look right	Look left	Look down	Look up	Mean	θ
Commercial	94.44%	74.88%	93.38%	88.78%	**87.87%**	**9.00%**
Carbon	93.51%	72.81%	86.22%	94.50%	**86.76%**	**10.0%**
AgCl	91.24%	81.49%	77.39%	86.39%	**84.13%**	**6.00%**
LIG	78.45%	96.30%	79.97%	94.36%	**87.27%**	**9.36%**

Table 4.3: Parallelism error between initial and return movement of EOG.

	Look rigth	Look left	Look down	Look up	Mean	θ
Commercial	0.94%	1.44%	0.28%	0.77%	**0.862%**	**0.478%**
Carbon	0.30%	1.22%	4.87%	2.21%	**2.16%**	**1.97%**
AgCl	6.10%	3.85%	1.43%	0.77%	**3.04%**	**2.43%**
LIG	1.60%	1.30%	4.49%	1.08%	**2.12%**	**1.59%**

the orientation of these vectors can be due to a non-perfect alignment of the electrodes' axis to the orientation of the cornea dipole. In this way, this difference in orientation can be used to correct the detected vectors by adding or subtracting this difference to the movement vectors. In Table 4.3 the relative parallelism error is shown. As it can be observed, the largest errors occur for the AgCl electrode with 6.1% "look right" movement. The rest of the movements and electrodes present lower errors, achieving a mean parallelism error of 2.04% ± 1.78%.

4.3.3 Electromyogram

Figure 4.10 shows the acquired EMG signals. While all the signals have an amplitude in the order of millivolts, commercial and LIG electrodes obtain higher amplitudes than screen printed electrodes. Commercial and LIG electrodes acquired an RMS value of 0.98 mV, while carbon electrodes resulted in an RMS value of 0.49mV and AgCl in 0.34 mV. In terms of noise, carbon and especially AgCl electrodes capture more noise than commercial and LIG electrodes. The spectrum of EMG signals extends over higher frequencies than the other signals studied so far, so the impedance has higher influence. As the results show, electrodes with capacitive behavior, as LIG and commercial ones, seem to have better performance while silver electrodes show lower amplitude.

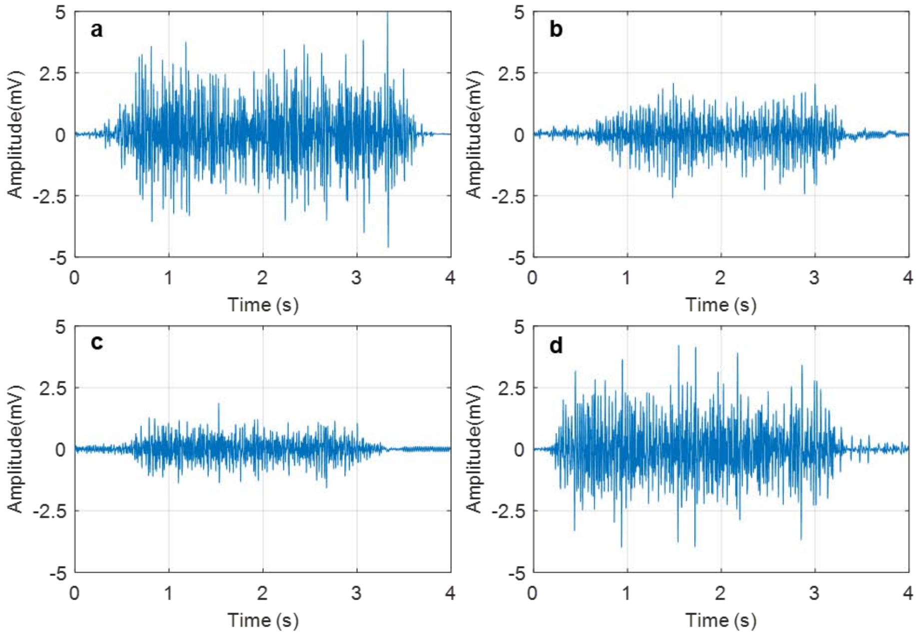

Figure 4.10: Raw EMG signals acquired a)Commercial, b)Carbon, c)AgCl, d)LIG.

As in the section 4.2, EMG is typically analyzed through his spectrum, Figure 4.11 shows the power spectrum density (PSD) of the acquired EMG signals. Results show that there are no significant variances between them, but for the level of the signals that, as discussed above, is lower for AgCl and carbon electrodes. The information of the signal is focused below 100Hz and above 20Hz. In the cases of commercial and LIG electrodes, a local maximum around 150 Hz is observed, which can be explained as a 50 Hz noise harmonic.

Table 4.4: EMG spectrum analysis results.

	MNF (Hz)	MDF (Hz)	RMS (mV)
Commercial	67.11	63.68	0.98
Carbon	69.20	61.67	0.49
AgCl	71.11	65.35	0.34
LIG	65.70	62.44	0.97

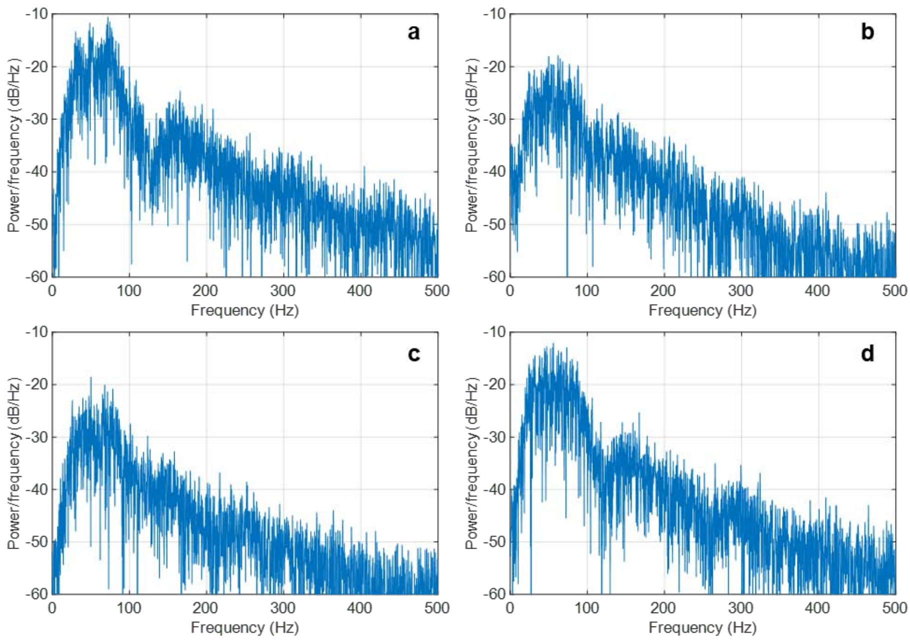

Figure 4.11: Power espectral density of the EMG signals acquired for each electrode a)Commercial, b)Carbon, c)AgCl, d)LIG.

Typical parameters that are analyzed in EMG diagnosis are Mean Frequency (MNF) and Median Frequency (MDF). In Table 4.4 these parameters obtained from the acquired signals are shown. Mean frequency is around 70 Hz, with the LIG electrode showing more deviation from this value with a mean value of 65.70 Hz. Median frequencies are between 60 and 65 Hz. In this case, the AgCl electrodes is the one that differs from the others, but it is consistent with the mean values as it provides the higher mean value. In any case, as expected, all the electrodes provided similar frequencies without noticeable differences.

Table 4.5: Summary of results obtained in this work.

	Commercial	**Carbon**	**AgCl**	**LIG**
Manufacturing complexity	High	Low	Low	Lowest
Sheet Resistance (Ω/cm^2)	0.255	23	0.062	360
ECG Accuracy	100 %	99.31 %	99.10 %	96.87 %
EOG Precision	87.87 %	86.76 %	84.13 %	87.27 %
EMG Accuracy	100 %	96.85%	97.38 %	98.05 %

4.3.4 Cost Analysis

Regarding the cost of the electrodes, as the substrates are not expensive, the main cost is derived from the pastes, which is a big advantage for the LIG electrodes. These electrodes have a unit cost of 0.27€, while Ag/AgCl ones have a unit cost of 1.02€. The price of carbon electrodes is intermediate, as the price of the carbon paste is lower than the silver paste's, keeping thus the unit cost at 0.56€. The unit cost of the commercial electrodes is around 0.50€, which is a similar price to carbon ones. Even if cost does not seem to be improved except for the LIG electrodes, it should be noted that the commercial electrodes are fabricated in mass, which results in much lower unit price when compared to the cost of the presented prototype electrodes. The electrodes developed in this work require techniques that can be easily moved to mass production, which will reduce their cost specially for screen printed electrodes.

Finally, Table 4.5 summarizes the main characteristics and results form each one of the presented electrodes.

4.4 Conclusions

Three types of printed flexible electrodes have been presented in this work. Two technologies have been used, LIG over Kapton and screen printing with AgCl and carbon pastes. The electrodes have been compared acquiring ECG and EOG, showing a comparable performance to that of commercial electrodes, while they are much more comfortable for the user and their manufacturing costs are also lower.

In the case of ECG acquisition, all the tested systems were able to acquire ECG without distorting it, even if a reduction of the amplitude is observed. The accuracy obtained with these electrodes in ECG-point detection is higher than 96.9%, which is the worst case value obtained for carbon electrodes. The best-performing electrode has been the AgCl electrode, with

99.3% of accuracy. It should be noted that the commercial electrodes were wet type electrodes, while the developed electrodes are dry, which has some influence in their performance due to the skin-electrode contact resistance.

For EOG, the electrodes were integrated in an *ad hoc* adhesive patch, and a custom measurement procedure was developed. With this integration, not only the ability to track eye motion was shown but also ergonomics were improved thanks to this flexible electronics technology. In this test, all the electrodes acquired similar waveforms, with the only differences lying in the acquisition noise, which was in any case corrected with wavelet-based processing. Regarding the accuracy in direction detection, LIG electrodes showed the best performance with 87.3% accuracy, very close to commercial electrodes (87.9% accuracy). Parallelism between movements in opposite directions was also analysed. It must be noted too that the presented measurement procedure may help define new applications based on EOG acquisition, due to its simplicity and reproducibility.

Electrodes were also tested during the acquisition of surface EMG. All the electrodes were able to obtain EMG signals with different amplitudes but without noticeable differences in the obtained spectrums. Typical EMG parameters, MDF and MNF, were compared for all the electrodes obtaining similar values in all the cases with a maximum deviation lower than 5Hz.

Thus, it has been demonstrated that the electrodes developed in this work could be used in cost-effective wearable devices to monitor biomedical variables. In addition, the techniques used in this work provide several advantages regarding high volume production for the industry and user comfort, while maintaining an equivalent performance to that of conventional electrodes.

Bibliography

[1] J. Andreu-Perez, D. R. Leff, H. M. D. Ip, and G.-Z. Yang, "From Wearable Sensors to Smart Implants-–Toward Pervasive and Personalized Healthcare," *IEEE Transactions on Biomedical Engineering*, vol. 62, no. 12, pp. 2750–2762, Dec. 2015. [Online]. Available: http://ieeexplore.ieee.org/document/7084595/

[2] P. J. Soh, G. A. Vandenbosch, M. Mercuri, and D. M.-P. Schreurs, "Wearable Wireless Health Monitoring: Current Developments, Challenges, and Future Trends," *IEEE Microwave Magazine*, vol. 16, no. 4, pp. 55–70, May 2015. [Online]. Available: http://ieeexplore.ieee.org/document/7072588/

[3] E. Wilkins, L. Wilson, K. Wickramasinghe, P. Bhatnagar, J. Leal, R. Luengo-Fernandez, R. Burns, M. Rayner, and N. Townsend, *European Cardiovascular Disease Statistics 2017*. Brussels: European Heart Network, Feb. 2017.

[4] X. Sun, S. Wang, Y. Xia, and W. Zheng, "Predictive-trend-aware composition of web services with time-varying quality-of-service," *IEEE Access*, vol. 8, pp. 1910–1921, 2020.

[5] H. Zhang, H. Zhang, S. Pirbhulal, W. Wu, and V. H. C. D. Albuquerque, "Active balancing mechanism for imbalanced medical data in deep learning–based classification models," *ACM Transactions on Multimedia Computing, Communications, and Applications*, vol. 16, no. 1s, pp. 1–15, mar 2020.

[6] S. Pirbhulal, O. W. Samuel, W. Wu, A. K. Sangaiah, and G. Li, "A joint resource-aware and medical data security framework for wearable healthcare systems," *Future Generation Computer Systems*, vol. 95, pp. 382–391, jun 2019.

[7] S. Pirbhulal, W. Wu, K. Muhammad, I. Mehmood, G. Li, and V. H. C. de Albuquerque, "Mobility enabled security for optimizing IoT based intelligent applications," *IEEE Network*, vol. 34, no. 2, pp. 72–77, mar 2020.

[8] A. K. Yetisen, J. L. Martinez-Hurtado, B. Ünal, A. Khademhosseini, and H. Butt, "Wearables in Medicine," *Advanced Materials*, vol. 30, no. 33, p. 1706910, Aug. 2018. [Online]. Available: http://doi.wiley.com/10.1002/adma.201706910

[9] D. Y. Kim, C.-H. Han, and C.-H. Im, "Development of an electrooculogram-based human-computer interface using involuntary eye movement by spatially rotating sound for communication of locked-in patients," *Scientific Reports*, vol. 8, no. 1, p. 9505, Dec. 2018. [Online]. Available: http://www.nature.com/articles/s41598-018-27865-5

[10] J. Arnin, D. Anopas, M. Horapong, P. Triponyuwasi, T. Yamsa-ard, S. Iampetch, and Y. Wongsawat, "Wireless-based portable EEG-EOG monitoring for real time drowsiness detection," in *2013 35th Annual International Conference of the IEEE Engineering in Medicine and Biology Society (EMBC)*. IEEE, jul 2013.

[11] R. J. Cochran and T. Rosen, "Contact Dermatitis Caused by ECG Electrode Paste:," *Southern Medical Journal*, vol. 73, no. 12, pp. 1667–1668,

Dec. 1980. [Online]. Available: http://content.wkhealth.com/linkback/openurl?sid=WKPTLP:landingpage&an=00007611-198012000-00043

[12] W. Uter and H. J. Schwanitz, "Contact dermatitis from propylene glycol in ECG electrode gel," *Contact Dermatitis*, vol. 34, no. 3, pp. 230–231, Mar. 1996. [Online]. Available: http://doi.wiley.com/10.1111/j.1600-0536.1996.tb02190.x

[13] S. L. Kappel, M. L. Rank, H. O. Toft, M. Andersen, and P. Kidmose, "Dry-contact electrode ear-EEG," *IEEE Transactions on Biomedical Engineering*, vol. 66, no. 1, pp. 150–158, jan 2019.

[14] Y. M. Chi, T.-P. Jung, and G. Cauwenberghs, "Dry-Contact and Noncontact Biopotential Electrodes: Methodological Review," *IEEE Reviews in Biomedical Engineering*, vol. 3, pp. 106–119, 2010. [Online]. Available: http://ieeexplore.ieee.org/document/5598518/

[15] Z. Cui, *Printed electronics: materials, technologies and applications.* Singapore: Wiley, 2016.

[16] S. Yao and Y. Zhu, "Nanomaterial-Enabled Dry Electrodes for Electrophysiological Sensing: A Review," *JOM*, vol. 68, no. 4, pp. 1145–1155, Apr. 2016. [Online]. Available: http://link.springer.com/10.1007/s11837-016-1818-0

[17] F. Romero, A. Salinas-Castillo, A. Rivadeneyra, A. Albrecht, A. Godoy, D. Morales, and N. Rodriguez, "In-Depth Study of Laser Diode Ablation of Kapton Polyimide for Flexible Conductive Substrates," *Nanomaterials*, vol. 8, no. 7, p. 517, Jul. 2018. [Online]. Available: http://www.mdpi.com/2079-4991/8/7/517

[18] Geng Yang, Li Xie, M. Mantysalo, Jian Chen, Hannu Tenhunen, and Li-Rong Zheng, "Bio-Patch Design and Implementation Based on a Low-Power System-on-Chip and Paper-Based Inkjet Printing Technology," *IEEE Transactions on Information Technology in Biomedicine*, vol. 16, no. 6, pp. 1043–1050, Nov. 2012. [Online]. Available: http://ieeexplore.ieee.org/document/6216418/

[19] S. Shustak, L. Inzelberg, S. Steinberg, D. Rand, M. David Pur, I. Hillel, S. Katzav, F. Fahoum, M. De Vos, A. Mirelman, and Y. Hanein, "Home monitoring of sleep with a temporary-tattoo EEG, EOG and EMG electrode array: a feasibility study," *Journal of Neural Engineering*, vol. 16, no. 2, p. 026024, Apr. 2019. [Online]. Available: http://stacks.iop.org/1741-2552/16/i=2/a=026024?key=crossref.a24c8829bc55dad299193824a6b25dda

[20] J. Lidón-Roger, G. Prats-Boluda, Y. Ye-Lin, J. Garcia-Casado, and E. Garcia-Breijo, "Textile Concentric Ring Electrodes for ECG Recording Based on Screen-Printing Technology," *Sensors*, vol. 18, no. 1, p. 300, Jan. 2018. [Online]. Available: http://www.mdpi.com/1424-8220/18/1/300

[21] X. Xu, M. Luo, P. He, X. Guo, and J. Yang, "Screen printed graphene electrodes on textile for wearable electrocardiogram monitoring," *Applied Physics A*, vol. 125, no. 10, p. 714, Oct. 2019. [Online]. Available: http://link.springer.com/10.1007/s00339-019-3006-x

[22] R. You, Y. Liu, Y. Hao, D. Han, Y. Zhang, and Z. You, "Laser Fabrication of Graphene-Based Flexible Electronics," *Advanced Materials*, p. 1901981, Aug. 2019. [Online]. Available: https://onlinelibrary.wiley.com/doi/abs/10.1002/adma.201901981

[23] N. Celik, N. Manivannan, A. Strudwick, and W. Balachandran, "Graphene-Enabled Electrodes for Electrocardiogram Monitoring," *Nanomaterials*, vol. 6, no. 9, p. 156, Aug. 2016. [Online]. Available: http://www.mdpi.com/2079-4991/6/9/156

[24] C. Lou, R. Li, Z. Li, T. Liang, Z. Wei, M. Run, X. Yan, and X. Liu, "Flexible Graphene Electrodes for Prolonged Dynamic ECG Monitoring," *Sensors*, vol. 16, no. 11, p. 1833, Nov. 2016. [Online]. Available: http://www.mdpi.com/1424-8220/16/11/1833

[25] N. Karim, S. Afroj, A. Malandraki, S. Butterworth, C. Beach, M. Rigout, K. S. Novoselov, A. J. Casson, and S. G. Yeates, "All inkjet-printed graphene-based conductive patterns for wearable e-textile applications," *Journal of Materials Chemistry C*, vol. 5, no. 44, pp. 11 640–11 648, 2017. [Online]. Available: http://xlink.rsc.org/?DOI=C7TC03669H

[26] B. Sun, R. N. McCay, S. Goswami, Y. Xu, C. Zhang, Y. Ling, J. Lin, and Z. Yan, "Gas-Permeable, Multifunctional On-Skin Electronics Based on Laser-Induced Porous Graphene and Sugar-Templated Elastomer Sponges," *Advanced Materials*, vol. 30, no. 50, p. 1804327, Dec. 2018. [Online]. Available: https://onlinelibrary.wiley.com/doi/abs/10.1002/adma.201804327

[27] F. J. Romero, E. Castillo, A. Rivadeneyra, A. Toral-Lopez, M. Becherer, F. G. Ruiz, N. Rodriguez, and D. P. Morales, "Inexpensive and flexible nanographene-based electrodes for ubiquitous electrocardiogram monitoring," *npj Flexible Electronics*, vol. 3, no. 1,

p. 12, Dec. 2019. [Online]. Available: http://www.nature.com/articles/s41528-019-0056-2

[28] Henkel, "INKS AND COATINGSPRINTED ELECTRONICS." [Online]. Available: https://dm.henkel-dam.com/is/content/henkel/Brochure_Printed_Electronics_Inks___Coatingspdf

[29] A. I. Solutions, "TECHNICAL DATA SHEETC-220 CARBON RESISTIVEINK." [Online]. Available: https://www.appliedinksolutions.com/pdf/c220-carbon-filled-ink.pdf

[30] Y. Hao, Y. Wang, L. Wang, Z. Ni, Z. Wang, R. Wang, C. K. Koo, Z. Shen, and J. T. L. Thong, "Probing layer number and stacking order of few-layer graphene by raman spectroscopy," *Small*, vol. 6, no. 2, pp. 195–200, jan 2010.

[31] Biopac, *El500 series – disposable electrodes*, BIOPAC Systems Inc., 2018. [Online]. Available: https://www.biopac.com/wp-content/uploads/EL500-Series.pdf

[32] PLUX, *Biosignal acquisition tool-kit for advancedresearch applicationsuser manual*, PLUX wireless biosignals S.A, 2018. [Online]. Available: https://www.biosignalsplux.com/downloads/biosignalsplux_User_Manual_v.1.0.pdf

[33] E. Castillo, D. P. Morales, A. García, Martínez-Martí, L. Parrilla, and A. J. Palma, "Noise Suppression in ECG Signals through Efficient One-Step Wavelet Processing Techniques," *Journal of Applied Mathematics*, vol. 2013, p. e763903, Jun. 2013. [Online]. Available: http://www.hindawi.com/journals/jam/2013/763903/abs/

[34] D. Farina, R. Merletti, and R. M. Enoka, "The extraction of neural strategies from the surface EMG," *Journal of Applied Physiology*, vol. 96, no. 4, pp. 1486–1495, apr 2004.

[35] D. Meldrum, E. Cahalane, R. Conroy, D. Fitzgerald, and O. Hardiman, "Maximum voluntary isometric contraction: Reference values and clinical application," *Amyotrophic Lateral Sclerosis*, vol. 8, no. 1, pp. 47–55, jan 2007.

[36] A. N. Pujari, R. D. Neilson, and M. Cardinale, "Fatiguing effects of indirect vibration stimulation in upper limb muscles- pre, post and during isometric contractions superimposed on upper limb vibration," sep 2018.

[37] L. Qi, J. M. Wakeling, A. Green, K. Lambrecht, and M. Ferguson-Pell, "Spectral properties of electromyographic and mechanomyographic signals during isometric ramp and step contractions in biceps brachii," *Journal of Electromyography and Kinesiology*, vol. 21, no. 1, pp. 128–135, feb 2011.

[38] D. Farina, M. Fosci, and R. Merletti, "Motor unit recruitment strategies investigated by surface EMG variables," *Journal of Applied Physiology*, vol. 92, no. 1, pp. 235–247, jan 2002.

[39] E. Castillo, D. P. Morales, A. García, L. Parrilla, V. U. Ruiz, and J. A. Álvarez-Bermejo, "A clustering-based method for single-channel fetal heart rate monitoring," *PLoS ONE*, vol. 13, p. e0199308, Jun. 2018. [Online]. Available: https://journals.plos.org/plosone/article?id=10.1371/journal.pone.0199308

[40] D. Purves, G. J. Angustine, D. Fitzpatrick, L. C. Katz, A.-S. LaMantia, J. O. McNamara, and S. M. Williams, Eds., *Neuroscience*. Sunderland, Mass: Sinauer Associates, 2001.

Chapter 5

Properties of silver chloride and carbon screen printed patterns on different textiles

Víctor Toral[1], Andreas Albretch[2], Encarnación Castillo[1], Antonio García[1], Markus Becherer[2], Almudena Rivadeneyra[1]

1 – Department of Electronics and Computer Technology, University of Granada 18071 Granada, Spain

2 – Institute of Nanoelectronics, Technical University of Munich, 80333, Munich, Germany

Published in Textile Research Journal. 2022, vol. 92(15-16), pp. 2711-2718

- Received: Published April 15, 2021
- DOI: 10.1177/00405175211005039
- Impact factor: 2.455
- JCR Rank: 7/26, category "Material Science, Textiles" (Q2)

Properties of silver chloride and carbon screen printed patterns on different textiles

Abstract: Smart textiles, known also as e-textiles, are of great interest for the development of healthcare and wellness applications, which require the embedding of electronic devices into the fabrics. Despite many prototype proposals may be found in the literature, the generalization and commercialization of e-textiles is limited by the lack of cost-effective, standard fabrication processes that can be applied to a large variety of fabrics. In this contribution, we analyze the deposition of silver and carbon pastes by screen printing methods on a wide selection of daily-use textiles, in order to gain insight over the main features to be considered when developing cost-effective smart textiles. Results show the prospects offered by screen printing to create conductive patterns over textile and flexible materials with sheet resistances lower than 1 Ω/sq and a good repeatability in the dimensions of the patterns

Keywords: e-textiles, screen printing, silver chloride, carbon, sheet resistance

5.1 Introduction

The boom of wearable electronics has driven the research on new materials applied to electronics, focusing on flexible and biocompatible electronic devices. Since many wearable devices are meant to be integrated in the clothing of the user, or even the body, new electronic devices are required to adapt to this environment and to place the focus on user comfort. Contrary to traditional rigid electronics, flexible electronics offer great advantages in this situation [1, 2].

These technologies can be applied to several real-life applications. One of the principal uses is the acquisition of biosignals, such as the electrocardiogram (ECG) [3] or the electromyogram (EMG), in this last case with applications to different kinds of prostheses [4]. Examples of clothing for biosignal acquisition oriented to sport and health monitoring can be found in the literature [5]. This is not limited to the academic field and commercial products such as the socks developed by Sensoria® [6] or the smart hat from 2XU [7] are already available. E-textiles can be applied to other fields such as chemical analysis, where applications for sweat analysis during physical activity [8] haven been presented.

Within this framework, conductive textiles allow to create devices directly on the clothing of the user instead of attaching them to the fabric, thus improving integration and opening a wide range of new applications [9, 10]. Several methods for the development of these materials can be found in the literature through the fabrication of conductive fibers. These methods range from the use of novel 2D materials based on graphene, like carbon nanotubes or graphene derivates, to the integration of conductive materials in the fibers of the textiles [11, 12, 13] . Conductive polymers, such as poly(3,4-ethylenedioxythiophene) polystyrene sulfonate (PEDOT) have been also used to create this kind of fibers [14, 15]. While these methods can provide high levels of integration and conductivity, they are expensive and not efficient when large-area elements are needed. Printing techniques with conductive inks and pastes can be much more efficient, as they are able to overcome those drawbacks. Multiple techniques are available, such as screen, inkjet, gravure or flexographic printing, or by coating the substrates [16, 17]. Spray deposition of conductive coatings can also be used for this purpose [18]. However, screen printing is the technique that best adapts to different textiles substrates. Even more, it requires fewer complex systems than gravure, flexographic or inkjet printing. Compared to spray coating, the availability of inks is also higher for screen printing. For these reasons this technique is widely used to create conductive patterns on textiles [19, 20, 21]. It has been used in the creation of wearable antennas and transmission lines [22, 23], or wearable flexible electrodes [24, 25, 26].

With all the above in mind, the use of screen printing with a wide range of fabric substrates is studied in this contribution, using carbon and silver pastes to print the patterns. This study first covers the physical characteristics of the patterns, such as thickness and conductivity, with different pastes. After that, the influence of the substrate over conductivity is studied over different substrates, from latex gloves to sanitary napkins, using silver chloride printed patterns for the measurements.

5.2 Materials and methods

As detailed in section 5.1, screen printing was selected for this study due to its versatility to print on different substrates. A manual screen printer from Siebdruck Versand was used to deposit the pastes [27]. In order to print the conductive sections, the silver chloride paste EDAG 6038E SS E&C from Loctite [28] and the carbon paste C220 form Applied Ink Solutions [29] were

Table 5.1: Selected materials (non-textiles marked with *).

Stretchable	Flexible	Non-stretchable
Bandage	Dishcloth (cross-linked cellulose and cotton)	Bandage interior
Rubber glove*	Kleenex*	Diaper
Latex glove*		PET*
Acrylic wool glove		Sanitary napkin
Nylon tights		

selected. Three different screens were used, depending on the viscosity of the paste. To achieve the maximum printing accuracy, the highest possible number of threads per centimeter, or mesh, is needed. However, this type of screen is not suitable for high viscosity pastes. For this reason, a 120 T/cm screen was used with the silver chloride paste, while a 47 T/cm screen was used for the carbon paste. Dielectric sections were also printed using the 47 T/cm screen and the TD-642 dielectric paste from Applied Ink Solutions. Furthermore, the silver paste CI-1036 from Engineered Conductive Materials, LLC with an 80 T/cm screen was used for simpler lines [30]. These pastes were selected in order to cover a wide range of applications, and they were used without any modification in their formulation. Since they are biocompatible, they are widely used in the fabrication of electrodes for biosignal acquisition. The application of these materials directly on textiles could enable their use for long-term monitoring [31].

In this study different types of substrates were also considered. The selection was done aiming to cover a wide range of stretchable materials, flexible materials, and non-stretchable porous materials, all of them usually present in industry or daily life, including some non-textiles. The chosen materials are shown in Table 5.1. This selection was intended to show a realistic representation of the applicability of smart textiles and the conversion of regular textiles into smart textiles. The layer arrangement shown in Figure 5.1 was printed over these substrates, including the conductive wiring with a dielectric covering on top.

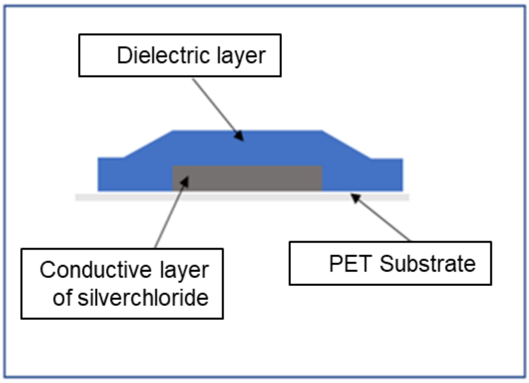

Figure 5.1: Cross-section scheme of the printed layers using the example of the printing of a conductor made of silver chloride with an overlying insulator.

Two aspects were analyzed in order to study the created patterns: first, the profile of a printed line, focusing on the height, the roughness and the reproducibility of the pattern, and, additionally, the ohmic resistance of the patterns printed over different substrates. For the profile measurements, a Dektak XT surface profilometer from Bruker was used, while microscope images of the printed structures were acquired with a DinoLite AM4115ZT microscope. For the roughness, the surface parameter R_a of the printed line was analyzed. This parameter is defined as:

$$R_a = \frac{1}{l} \int_0^l |z(x)| \; dx \tag{5.1}$$

where l is the length of the analyzed profile and $z(x)$ is the deviation from the average height of the measured profile.

On the other hand, the sheet resistance was also analyzed on the different substrates. This measurement was carried out using a four-point probe head from Jandel connected to a B2901A Keysight source measuring unit (SMU). A constant current of 10 µA was sourced for all measurements. The sheet resistance can then be measured following the same method described by Valdes [32]. As the roughness of the substrate can affect the sheet resistance and in order to have a reference, the same patterns were printed over PET films, where roughness is much lower than on the rest of substrates. Thus, on PET, the carbon paste exhibited a sheet resistance of 15 Ω/sq. while the silver chloride's was 0.05 Ω/sq.

For stretchable materials, bending tests were carried out in addition to static tests. The bending tests were done with a custom-made setup as the one described by Albretch *et al.* [33]. This bending test was thus started with small strains of 0.1%, which were gradually increased until the breaking point. For the materials enduring more strain, the sheet resistance was measured after 10 consecutive bending cycles with strains below the breaking point, to study how the mechanical efforts in the substrate impacted the sheet resistance.

5.3 Results and Discussion

5.3.1 Profile characteristics

The first study is referred to the profile characteristics of the printed lines. In order to avoid any influence in this regard from the properties of the different substrates, several sets of lines, as it will be described below, were printed on the reference PET substrate. It must be also noted that the solid content of the silver chloride paste, according to the manufacturer's data sheet [28], is 66%, with a 9:1 ratio of silver and silver chloride, and a mixture of diethylene glycol monobutyl ether and methoxypropyl acetate as solvents. In the case of the carbon paste, the solid content of graphite is 42%, with gamma-butyrolactone and dimetyl glutarate as solvents [29].

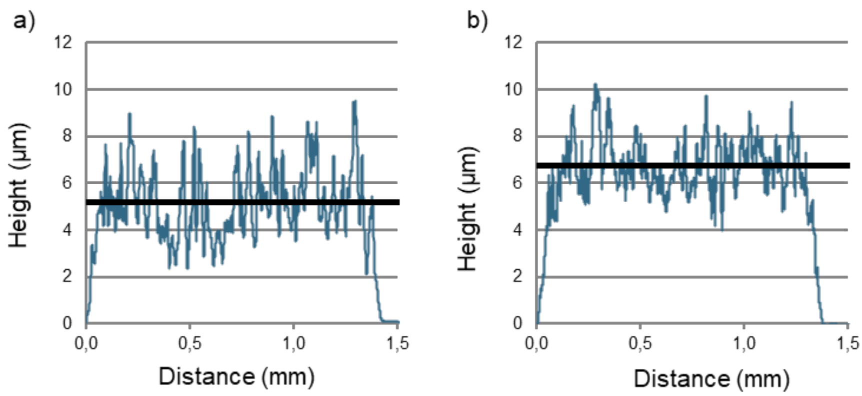

Figure 5.2: Comparison of the profile diagram of a printed line: a) carbon, b) silver chloride (profilometer measurements in blue, mean values in black).

Figure 5.2 shows the thickness comparison between a printed line of carbon paste and a one printed with the silver chloride paste. Black lines represent the average thickness of these lines. In the case of the carbon paste, this average is only referred to the thickness measured between 0.02

mm and 1.38 mm in the Distance axis of Figure 5.2, while for silver chloride the average thickness covers measurements from 0.054 mm to 1.33 mm in the Distance axis of Figure 5.2. The thickness measured in the carbon line was 5.18 µm, while the silver chloride line thickness was 6.73 µm. The silver chloride paste line was thus approximately 30% thicker than the carbon paste one, which is mostly due to the lower solid content of the carbon paste.

The roughness of the patterns was compared to the R_a values of each profile. Thus, carbon ink printed lines showed an R_a value of 1.19 µm, while for the silver chloride it was 0.93 µm. Carbon lines were thus 22% rougher than silver paste ones and, taking into account that the carbon lines were thinner, this results in a much irregular surface.

Comparing the line widths, silver chloride lines were 1.24-mm wide, while for carbon this width was 1.36 mm. Both differ from the 1-mm width of the mask in approximately 0.3 mm, because the paste is pushed slightly beyond the edges of the mask.

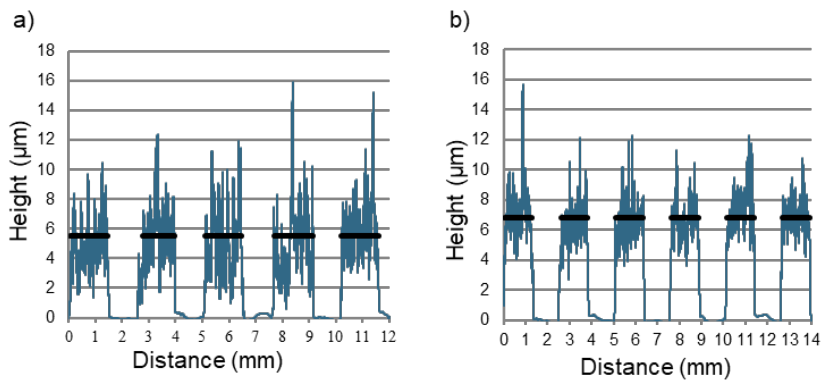

Figure 5.3: Comparison of the profile diagrams of several printed lines: a) carbon, b) silver chloride (profilometer measurements in blue, mean values in black).

To compare the reproducibility of the lines, a pattern with several adjacent lines was printed. In Figure 5.3, the profiles measured with both carbon and silver pastes are shown. The average line height was calculated discarding the gaps between the lines, thus calculating the individual thickness of the lines and averaging all of them. The mean height of silver lines was 6.86 µm with a standard deviation of 0.44 µm, while for carbon lines, the mean was 5.42 µm with a standard deviation of 0.67 µm. From these values, it may be noticed that the individual lines of both printed structures presented uniform thickness. However, the silver lines showed higher thickness than the carbon ones, being 1.44 µm thicker, which is consistent with the results obtained above for single lines. The variability of the lines was under 12% in both cases, while carbon lines were more variable than silver chloride lines, as expected from the roughness results. Regarding the width of the lines, the carbon lines were 1.40-mm wide in average with standard deviation of 38 µm, and the silver chloride lines were 1.24-mm wide with standard deviation of 34 µm. The variation in both cases was 2.7% of the mean value.

To create multilayer structures, dielectric layers are required between consecutive conductive layers in order to avoid short circuits. Thus, the profile of a dielectric layer printed over a line of silver chloride, as the one shown in Figure 5.4a, was also studied. In this type of structures, since the dielectric layer is the base for the next conductive layer, the roughness of the printed dielectric is key. A possible solution to reduce the roughness of the dielectric is to print several layers of dielectric over the silver chloride line. Figure 5.4b shows the profile of such structure. The average thickness was studied in those zones that did not have silver chloride under the dielectric. The results showed a thickness of 4.85 µm for a single layer and 11.52 µm for the multiple-layer print.

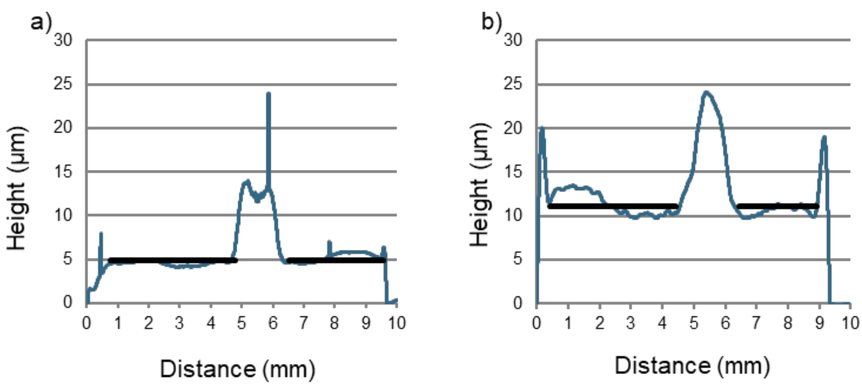

Figure 5.4: Comparison of the profile diagrams of a printed silver chloride line with: a) single-layer printed dielectric, b) multiple-layer printed dielectric (profilometer measurement in blue, mean in black).

The standard deviation of the measured values was 0.56 µm for a single layer and 1.95 µm for four layers. The surface of the single layer was quite smooth with a R_a value of 0.43 µm, while the four-layer structure showed some roughness, with R_a of 1.42 µm, that can be explained by the highest thickness measured between 0.5 mm and 2.5 mm (in the Distance axis of Figure 5.4b) and probably due to a lower pressure in this zone during printing. Two elevations at the printing edges are noticeable, as there is always more paste at the end of the screen, *i.e.*, at the transition from the permeable to the impermeable part of the sieve, than in the middle part of the screen. Since this multilayer structure was printed several times and the squeegee was thus drawn from right to left and left to right over the screen, the increase found on both sides is higher.

The results of the bending test showed noticeable differences between materials. The maximum possible strain, *i.e.*, the strain at the breaking point, for the bandage was below 2%, while the maximum strain for the acrylic wool glove and the nylon tights was up to 12%. The rubber and latex substrates could bear even higher strains, up to 32% and 35% respectively.

Finally, preliminary manual rubbing tests were carried out over the PET substrate with both pastes, carbon and silver chloride. The different printings were rubbed for 70 cycles using a microfiber cloth, while the ohmic resistance was measured after every 10 cycles. With this, results showed two differentiated behaviors: the silver chloride paste did not change its resistance after 70 cycles, while the carbon paste increased its resistance by around a 20% after 70 cycles. Even with wear begin visually appreciable in both pastes, only the carbon paste's resistance was altered.

5.3.2 Substrate influence on ohmic resistance.

After the study above on the reference PET substrate, silver chloride conductive lines were printed on the different substrates in order to measure printed sheet resistances. Since the silver chloride paste resulted in smoother, more conductive and more durable patterns, only silver chloride was considered on the different substrates in Table 5.1 for this evaluation of the influence of the substrate on the ohmic resistance. Microscope images of the most representative substrates are shown in Figure 5.5 5. These enable a closer examination of the surface structures of the substrates, as well as of the printed structures, in order to draw possible conclusions regarding the respective conductivity of the printing. The same magnification was chosen for all substrates. The rubber glove (Figure 5.5a) presents a very smooth surface compared to the other substrates, as well as the layer printed on it. This means that there are no irregularities, in the form of holes or the like, recognizable in the layer. It is thus possible to print a precise edge on this material. Apparently, there are no indications of a reduced conductivity. The images of the sanitary napkin (Figure 5.5b), the acrylic wool glove (Figure 5.5c) and the nylon tights (Figure 5.5d) reveal a thread-like structure, with a significantly coarser fabric in the sanitary napkin and the acrylic wool glove. These substrates are characterized by the multi-layered nature of the material, *i.e.*, the fact that several fibers lie on top of and underneath each other, which is confirmed by the partially blurred microscope images.

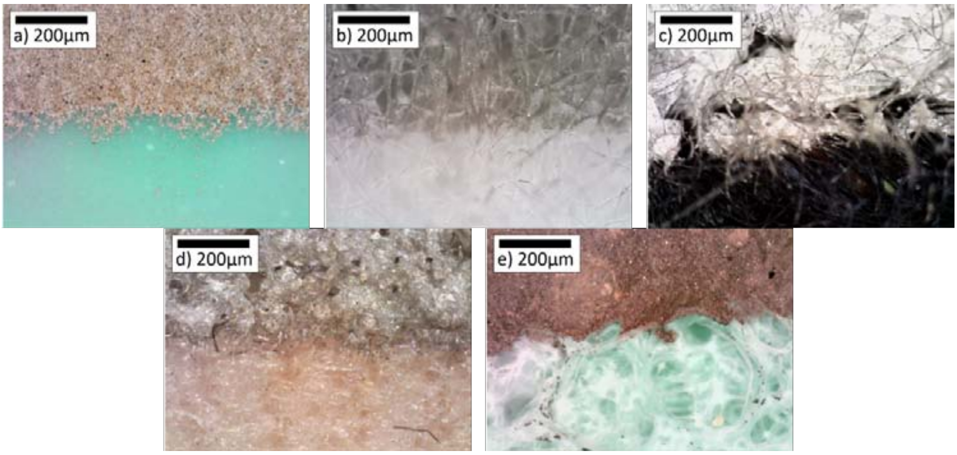

Figure 5.5: Selected microscope images of different substrates with printed silver paste: a) rubber glove; b) sanitary napkin; c) fabric glove; d) nylon tights; e) dishcloth. The printed silver can be observed in the top half of the images, the unprinted substrate in the bottom areas.

The dishcloth textile (Figure 5.5e) is characterized by a coarse-pored structure, so larger air gaps can be observed and the surface is therefore uneven. The printed layer, on the other hand, presents little unevenness and few holes or other defects.

Table 5.2 lists all the measured sheet resistances of the printed silver on the respective materials. The results show that all printed structures were conductive but presented different sheet resistances. Apart from the values measured for the nylon tights, all values are under 1 Ω/sq. It is striking that the printed silver paste conducts best on the dishcloth, even better than on the PET reference. This can be attributed to the fact that the substrate material itself is slightly conductive, as a resistance in the mega-ohm range can be measured for this material without any deposited conductive layer. In addition, the holes visible in Figure 5.5e are filled with conductive paste and the sponge-like tissue is able to absorb paste, thus resulting in many contact points between the silver layers even deeper in the tissue. Thin fabrics with a fine structure like the bandage and the kleenex also show low sheet resistances when compared to the rest of the tested substrates. These are comparable to the values on PET. Although less paste can be

Table 5.2: Sheet resistance of printed silver on different materials. Errors are calculated as the standard deviation of 5 different samples.

Material	R (mΩ/sq)
Dishcloth	100 ± 50
Bandage	320 ± 80
Kleenex	380 ± 70
Bandage interior	430 ± 50
Diaper	540 ± 50
PET	586 ± 5
Sanitary napkin	630 ± 60
Rubber glove	660 ± 30
Latex glove	790 ± 30
Acrylic wool glove	940 ± 10
Nylon tights	5000 ± 200

absorbed here, the relatively smooth surfaces are a good prerequisite for a layer with few holes, which reduces the resistance. In any case, as illustrated by the standard deviations of the measurements in Table 5.2, measurement dispersion is observed for all the materials when compared to PET, which is a specially smooth substrate and ideal for printing applications. These deviations could thus be reduced flattening the substrates with a preprint of a dielectric layer.

Coarser materials, such as the diaper, the sanitary napkin or the acrylic wool glove, generate more and larger holes (Figure 5.5b and Figure 5.5c), which could be related to a higher sheet resistance. However, this is not observed in all cases. For example, although the fibers in the nylon tights are thinner than in the fabrics just mentioned (see Figure 5.5d), the sheet resistance is higher in this case. As more paste can penetrate deeper into some of the fibrous materials that are more absorbent due to their purpose, such as the dishcloth and the bandage, and, although the structure reveals holes from above, they can still provide enough contact points. The rubber and latex gloves also confirm the effect of a smooth surface, as they show a comparatively high sheet resistance.

Bending tests showed low influence of the mechanical effort on the sheet resistance. For the latex gloves, the variation in the sheet resistance was 10% and the change in sheet resistance for the rubber ones was 8%. This small difference is probably due to the lower stretchability of rubber gloves. Finally, despite no deep study on the useful life of the patterns was carried out, some surface oxidation was observed in some patterns that were not encapsulated with dielectric. Thus, a dielectric coating should avoid this effect.

5.4 Conclusions

Screen printing with conductive pastes over different flexible and stretchable substrates was studied in this work. Firstly, thickness, roughness and width of the printed patterns were analyzed. The results show uniform and highly reproducible patterns for both of the used pastes. In terms of thickness and width of the patterns, printed variability was less than 12% in thickness and less than 2.7% in width. Regarding the roughness of the patterns, it was under 1.19 µm, with carbon patterns the roughest. This all demonstrates how the printings can be easily replicated with consistent repeatability. Also, the capability to create multilayer structures was illustrated through the use of the dielectric paste TD-642 between conductive layers. The best option to create this multilayer structure was to only print a dielectric layer as it resulted in a 30 % smoother surface.

Additionally, the sheet resistance of the patterns was studied over several textile materials using the silver chloride paste, since it provided the most uniform patterns. For all of the materials, but for nylon, the resistances were under 1 Ω/sq. The materials with lower resistance were those capable to absorb the paste, thus creating a conductive surface that penetrates in the material. Materials with coarser fibrous substrates, such as the acrylic wool gloves, were those with lower performance, since the paste over those materials created a surface with many defects and uneven surfaces.

With all of the above, it has been demonstrated the capability of screen printing to easily create conductive flexible patterns over textile and flexible materials with sheet resistances lower than 1 Ω/sq and with a good repeatability of the patterns, even when created with multiple layers of dielectric. With these results, the possibilities to create circuits on textile and flexible materials has been illustrated, thus opening a wide range of applications. Direct applications may include the acquisition of biosignals through electrodes printed on the clothing, or the use of textiles for interconnection with other developed patches, which can create a complete body sensor network in the user clothing. Furthermore, the combination of these conductive patterns with sensitive substances could allow the development of wearable sensors for chemical substances, biomechanical analysis, or environmental variable sensing.

Bibliography

[1] A. Nathan, A. Ahnood, M. T. Cole, S. Lee, Y. Suzuki, P. Hiralal, F. Bonaccorso, T. Hasan, L. Garcia-Gancedo, A. Dyadyusha, S. Haque, P. Andrew, S. Hofmann, J. Moultrie, D. Chu, A. J. Flewitt, A. C. Ferrari, M. J. Kelly, J. Robertson, G. A. J. Amaratunga, and W. I. Milne, "Flexible electronics: The next ubiquitous platform," *Proceedings of the IEEE*, vol. 100, no. Special Centennial Issue, pp. 1486–1517, 5 2012.

[2] F. Axisa, P. Schmitt, C. Gehin, G. Delhomme, E. McAdams, and A. Dittmar, "Flexible technologies and smart clothing for citizen medicine, home healthcare, and disease prevention," *IEEE Transactions on Information Technology in Biomedicine*, vol. 9, no. 3, pp. 325–336, 9 2005.

[3] W. Wu, S. Pirbhulal, A. K. Sangaiah, S. C. Mukhopadhyay, and G. Li, "Optimization of signal quality over comfortability of textile electrodes for ecg monitoring in fog computing based medical applications," *Future Generation Computer Systems*, vol. 86, pp. 515–526, 9 2018.

[4] E. L. Secco, C. Moutschen, A. T. Maereg, M. Barrett-Baxendale, D. Reid, and A. K. Nagar, "Development of a sustainable and ergonomic interface for the emg control of prosthetic hands," 2017, pp. 321–327.

[5] R. Paradiso, G. De Toma, and C. Mancuso, "Smart textile suit," in *Seamless Healthcare Monitoring*. Cham: Springer International Publishing, 2018, pp. 251–277.

[6] "Sensoria fitness," 0, [Online; accessed 2020-12-20]. [Online]. Available: https://store.sensoriafitness.com/one-additional-pair-of-smart-sock-v2-0/

[7] "2xu," 0, [Online; accessed 2020-12-20]. [Online]. Available: https://www.2xu.com/us/p/tracking-hat/UQ4194f.html?lang=en_US

[8] S. Coyle, K.-T. Lau, N. Moyna, D. O'Gorman, D. Diamond, F. Di Francesco, D. Costanzo, P. Salvo, M. G. Trivella, D. E. De Rossi, N. Taccini, R. Paradiso, J.-A. Porchet, A. Ridolfi, J. Luprano, C. Chuzel, T. Lanier, F. Revol-Cavalier, S. Schoumacker, V. Mourier, I. Chartier, R. Convert, H. De-Moncuit, and C. Bini, "Biotex—biosensing textiles for personalised healthcare management," *IEEE Transactions on Information Technology in Biomedicine*, vol. 14, no. 2, pp. 364–370, 3 2010.

[9] K. KelvinFu, R. Padbury, O. Toprakci, M. Dirican, and X. Zhang, “Conductive textiles,” in *Engineering of High-Performance Textiles.* Elsevier, 9 2018, pp. 305–334.

[10] R. Wu, L. Ma, A. Patil, C. Hou, S. Zhu, X. Fan, H. Lin, W. Yu, W. Guo, and X. Y. Liu, “All-textile electronic skin enabled by highly elastic spacer fabric and conductive fibers,” *ACS Applied Materials and Interfaces*, vol. 11, no. 36, pp. 33 336–33 346, 9 2019.

[11] A. I. Neves, D. P. Rodrigues, A. De Sanctis, E. T. Alonso, M. S. Pereira, V. S. Amaral, V. L. Melo, S. Russo, I. De Schrijver, H. Alves, and M. F. Craciun, “Towards conductive textiles: Coating polymeric fibres with graphene,” *Scientific Reports*, vol. 7, no. 1, pp. 1–10, 12 2017.

[12] C. H. Xue, J. Chen, W. Yin, S. T. Jia, and J. Z. Ma, “Superhydrophobic conductive textiles with antibacterial property by coating fibers with silver nanoparticles,” *Applied Surface Science*, vol. 258, no. 7, pp. 2468–2472, 1 2012.

[13] Y. Zhao, J. Wang, Z. Li, X. Zhang, M. Tian, X. Zhang, X. Liu, L. Qu, and S. Zhu, “Washable, durable and flame retardant conductive textiles based on reduced graphene oxide modification,” *Cellulose*, vol. 27, no. 3, pp. 1763–1771, 2 2020.

[14] H. H. Kuhn, W. C. Kimbrell, J. E. Fowler, and C. N. Barry, “Properties and applications of conductive textiles,” *Synthetic Metals*, vol. 57, no. 1, pp. 3707–3712, 4 1993.

[15] D. Knittel and E. Schollmeyer, “Electrically high-conductive textiles,” *Synthetic Metals*, vol. 159, no. 14, pp. 1433–1437, 7 2009.

[16] S. Khan, L. Lorenzelli, and R. S. Dahiya, “Technologies for printing sensors and electronics over large flexible substrates: A review,” *IEEE Sensors Journal*, vol. 15, no. 6, pp. 3164–3185, 6 2015.

[17] N. Maheshwari, M. Abd-Ellah, and I. A. Goldthorpe, “Transfer printing of silver nanowire conductive ink for e-textile applications,” *Flexible and Printed Electronics*, vol. 4, no. 2, p. 025005, 6 2019.

[18] A. Samanta and R. Bordes, “Conductive textiles prepared by spray coating of water-based graphene dispersions,” *RSC Advances*, vol. 10, no. 4, pp. 2396–2403, 1 2020.

[19] A. Hobby, “Fundamentals of screens for electronics screen printing,” *Circuit World*, vol. 16, no. 4, pp. 16–28, 3 1990.

[20] G. Nisato, D. Lupo, and S. Ganz, *Organic and printed electronics: Fundamentals and applications*, 2016.

[21] I. Kazani, C. Hertleer, G. De Mey, A. Schwarz, G. Guxho, and L. Van Langenhove, "Electrical conductive textiles obtained by screen printing," *Fibres and Textiles in Eastern Europe*, vol. Nr 1 (90), pp. 57–63, 2012.

[22] I. Locher and G. Tröster, "Screen-printed textile transmission lines," *Textile Research Journal*, vol. 77, no. 11, pp. 837–842, 11 2007.

[23] M. L. Scarpello, I. Kazani, C. Hertleer, H. Rogier, and D. Vande Ginste, "Stability and efficiency of screen-printed wearable and washable antennas," *IEEE Antennas and Wireless Propagation Letters*, vol. 11, pp. 838–841, 2012.

[24] G. Paul, R. Torah, S. Beeby, and J. Tudor, "The development of screen printed conductive networks on textiles for biopotential monitoring applications," *Sensors and Actuators, A: Physical*, vol. 206, pp. 35–41, 2 2014.

[25] K. Yang, C. Freeman, R. Torah, S. Beeby, and J. Tudor, "Screen printed fabric electrode array for wearable functional electrical stimulation," *Sensors and Actuators A: Physical*, vol. 213, pp. 108–115, 7 2014.

[26] K. Yang, R. Torah, Y. Wei, S. Beeby, and J. Tudor, "Waterproof and durable screen printed silver conductive tracks on textiles," *Textile Research Journal*, vol. 83, no. 19, pp. 2023–2031, 11 2013.

[27] S. Versand, "Siebdruck-versand webpage," 0, [Online; accessed 2020-05-19]. [Online]. Available: https://www.siebdruck-versand.de/

[28] "Safety datasheet edag 6038e," 0, [Online; accessed 2020-10-21]. [Online]. Available: https://mysds.henkel.com/SAP_GATEWAY/odata/SAP/YPSSWH_DOO_SRV//DocContentSet(Appid='YPSSW_SDSUA',Matnr='000000000001837601',Matnrcomp='',Subid='000000487422',Subidcomp='',Sbgvid='MSDS_UT_US',Laiso='EN')/DocContentData/$value

[29] "C-220 safety data sheet," 0, [Online; accessed 2020-10-21]. [Online]. Available: https://kayakuam.com/wp-content/uploads/2020/03/SDS-C-220-Carbon-Resistive-Ink-US.pdf

[30] "Ci-1036 technical data sheet," 0, [Online; accessed 2020-10-21]. [Online]. Available: http://www.conductives.com/pdfs/CI-1036.pdf

[31] A. Ankhili, X. Tao, C. Cochrane, V. Koncar, D. Coulon, and J.-M. Tarlet, "Comparative study on conductive knitted fabric electrodes for long-term electrocardiography monitoring: Silver-plated and pedot:pss coated fabrics," *Sensors*, vol. 18, no. 11, p. 3890, 11 2018.

[32] L. Valdes, "Resistivity measurements on germanium for transistors," *Proceedings of the IRE*, vol. 42, no. 2, pp. 420–427, 2 1954.

[33] A. Albrecht, M. Bobinger, J. Salmerón, M. Becherer, G. Cheng, P. Lugli, and A. Rivedeneyra, "Over-stretching tolerant conductors on rubber films by inkjet-printing silver nanoparticles for wearables," *Polymers*, vol. 10, no. 12, p. 1413, 12 2018.

Chapter 6

Optimization of Cost-Effective and Reproducible Flexible Humidity Sensors Based on Metal-Organic Frameworks

Víctor Toral[1], Florin C. Loghin[2], Antonio Rodríguez-Diéguez[3], Alejandro Lapresta-Fernández[4], Diego P. Morales[1], Almudena Rivadeneyra[1], Alfonso Salinas-Castillo[4]

1 – Department of Electronics and Computer Technology, Faculty of Science, University of Granada 18071 Granada, Spain

2 – Institute of Nanoelectronics, Technical University of Munich, 80333 Munich, Germany

3 – Department of Inorganic Chemistry , University of Granada, 18071 Granada, Spain

4 – Department of Analytic Chemistry, Faculty of Science, University of Granada, 18071, Granada, Spain

Published in Sensors 2020, vol. 20(23), art. 6981

- Received: 16 October 2020; Accepted: 3 December 2020; Published: 7 December 2020
- DOI: 10.3390/s20236981

- Impact factor: 3.576
- JCR Rank: 82/273, category "Engineering, Electrical and electronics" (Q2)

Optimization of Cost-Effective and Reproducible Flexible Humidity Sensors Based on Metal-Organic Frameworks

Abstract: In this letter, we present the extension of a previous work on a cost-effective method for fabricating highly sensitive humidity sensors on flexible substrates with a reversible response, allowing precise monitoring of the humidity threshold. In that work we demonstrated the use of three-dimensional Metal-Organic Framework (MOF) film deposition based on the perylene-3,4,9,10-tetracarboxylate linker, potassium as metallic center and the inter-spacing of silver interdigitated electrodes (IDEs) as humidity sensors. In this work, we study one of the most important issues in efficient and reproducible mass production, which is to optimize the most important processes' parameters in their fabrication, such as controlling the thickness of the sensor's layers. We demonstrate this method not only allows for the creation of humidity sensors, but it also is possible to change the humidity value that changes the actuator state.

Keywords: interdigitated electrodes; metal-organic frameworks; flexible electronics; printed electronics

6.1 Introduction

Many industrial processes are sensitive to water content in the air. For this reason, humidity sensors are crucial for several industries, such as electronics or food that need to control Relative Humidity (RH) during manufacturing or transportation [1, 2, 3]. Moreover, not only does industry need these sensors, domotic systems or intelligent control in household applications, for example, also require this type of sensor to control and accommodate ambient conditions for comfort. For these needs, lowering the cost and size of these sensors can be a great benefit, especially in this era of massive Internet of Thing (IoT) connected devices collecting a huge amount of data that requires a massive distribution of sensors [4].

RH sensors are typically based on ceramic materials such as aluminum oxide, semiconducting materials such as SiO_2, or polymers [5, 6]. Moreover, 1D and 2D materials have appeared as solutions to flexible and highly integrable sensors, as for example carbon nanotubes [7] or silicon nanosheets [8]. In the same context of novel materials, carbon-based materials have been also widely used [9]. Furthermore, in novel miniaturized sensors, the use of a printed layer of different materials like organic compounds or nanoparticles over Inter-Digitated Electrodes (IDE) is common [10, 11]. Due to their structural features, Metal-Organic Framework (MOF) have properties that have attracted great interest in recent years [12, 13, 14, 15]. These types of materials can also be used as RH sensors because of their luminescence or impedance [16, 17].

Typically, RH sensors have been passive, based on the variation in capacitance or resistance of the materials employed. Several works have treated active devices that react to RH; they are based on the variation of threshold voltage in Field Effect Transitor (FET) or the resistivity of the channel. However, these devices are indirect measures of RH, as the device does not react to the RH values [18, 19]. In a previous work, we demonstrated the potential use of the perylene-3,4,9,10-tetracarboxylate linker with potassium (K-Pery) for humidity actuators [20]. Silver IDE were drop-casted with K-Pery water solution, showing a drastic change in impedance response at 40% RH from capacitive to resistive response. However, it did not cover the influence of the deposition of the K-Pery solution, the IDEs' dimensions, or if these parameters could help to tune the RH level that triggers the device from capacitive to resistive mode. In this paper, we fabricate similar devices but with more controllable processes and analyze their responses.

We studied the influence of two aspects in the fabrication of sensors: the deposition of K-Pery solution and the interspacing of IDEs. For the deposition of K-Pery, in previous work we employed drop-casting, which despite its simplicity did not allow us to control the thickness of the deposited layer with accuracy. To solve this problem, multiple techniques are available [21, 22]. For example, roller coating is widely used in industries with high production volumes; however, it is quite expensive for small volumes of production [23]. Another possibility is spin coating, the same technique used for the fabrication of CD-R photo sensible layers [24]. However, in this case the presence of IDEs could affect the roughness and uniformity of the surface of thin layers. In terms of cost, despite being better than roller coating techniques, it is not the least expensive solution. Spray coating was found to be the most adequate for this application; it is a low-cost technique, and the thickness of the layer is more controllable just by varying the mixed portion of air and coating material [25, 26].

The other fabrication parameter that can be studied is the IDEs' interspacing. As the system detects humidity through conductivity, with a higher interspacing, better conductivity of K-Pery will be needed to have the same conductivity between IDE fingers. This could allow us to control the trigger level for the device.

6.2 Materials and Methods

6.2.1 K-Pery Preparation

The compound was obtained by conventional routes by using reagents from commercial sources as received in a similar way as it was done in the previous work [20]. The perylenetetracarboxylic derivative ligand (0.1 mmol) was added to 5 mL of H_2O. The resulting red solution was sonicated for 30 min, and then 5 mL of an aqueous solution with KOH (0.1 mmol) was incorporated into it. The resulting solution was heated for 24 h under a 150W IR lamp at 25 cm distance. Orange hexagonal crystals were obtained totally pure, whose composition was $C_{72}H_{36}K_8O_{28}$ (See Figure A.4 in Appendix A). The yield was normally close to 65%.

6.2.2 Sensor Fabrication

For the device fabrication, K-Pery powder was brought into the solution by dissolving it in deionized water (Di H_2O) in a ratio of 1:10 (K-Pery: Di H_2O), followed by sonication in an ultrasonic bath for 15 min. The K-Pery powder is a 3D metal-organic framework based on the perylene-3,4,9,10-tetracarboxylate linker and potassium as the metallic center. For

Table 6.1: Conditions during fabrication for each of the deposited K-Pery layers.

Name	Volume(mL)	Temperature (°C)
Type 1	2	70
Type 2	2	90
Type 3	2	110
Type 4	4	70
Type 5	4	110

the deposition of the K-Pery solution, a handheld airbrush was used. The control parameters were K-Pery solution, airbrush sample spacing and airbrush opening, while the hotplate temperature was varied from 70°C to 110°C. These temperatures were selected to generate two scenarios for the evaporation of the solvent at the other fixed process parameters. At 70°C, evaporation was relatively slow with a visible wet film forming allowing for the merging of droplets, which can be referred to as a wet spray, while at 110°C the film instantaneously dried without droplets merging. This can be referred to as dry spraying. Table 6.1 summarizes the combinations of dry scenarios and volume deposited used in this work. The selection of the volume was to cover as much of the available space as possible.

After the deposition of the solution onto the substrate, an interdigitated electrode structure patterned onto the Polyethilene terephthalate (PET) substrate. The deposition of the electrodes was done by printing a silver conductive paste (Sigma Aldrich, Darmstadt, Germany) with a manual screen printer (Siebdruck Versand). The sensor area was fixed to 25 mm^2 and a fixed finger width of 200μm, while for finger spacing, 300μm and 400μm were used for comparison. The drying of the Ag layer was performed at 60°C for 10 min in a UF55 oven from Memmert (Schwabach, Germany). Figure 6.1 represents schematically the sensor composition and the dimensions of the IDE fabricated.

6.2.3 Characterization

An optical microscope DM2500 equipped with a DFC295 camera (Leica Microsystems, Germany) was employed for the images. For the electrical characterization, an impedance analyzer E4990A (KeysightTechnologies, Boeblingen, Germany) in combination with an impedance probe kit (42941A) was controlled with LabView 2016. The interface with the sensor was a SubMiniature version A (SMA) male connector glued with silver paste. The

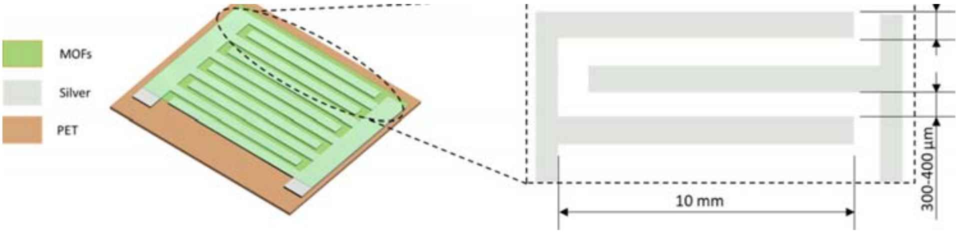

Figure 6.1: Optical microscope images for the spray coating with the different fabrication parameters: type 1 (a); type 2 (b); type 3 (c); type 4 (d); type 5 (e).

excitation applied was VDC = 0 and VAC = 500 mV in the range of 100 Hz to 10 MHz. Calibration was done to compensate the parasitic elements, as performed previously [27]. To control temperature and humidity, a climatic chamber VCL4006 (Vötsch Industrietechnik GmbH, Balingen, Germany) was used to place the sensor. The monitoring was performed over the climatic sensor system. During experiments, moisture content was ramped up from 20% to 80% in 10% steps with pauses of 1 h to stabilize the value in the whole chamber volume.

6.3 Results

6.3.1 Physical Characterization

Optical microscope images of the different types of sprayed K-Pery layers are shown in Figure 6.2. They show the differences in deposition method, especially in the size and morphology of the crystalized MOFs. Figure 6.2a displays a clear coffee stain effect that can be attributed to a solvent evaporation time frame that was too long, allowing for such effects to happen. Microscopically the material was transported to the edge of the droplets, leaving void areas. For further reference see [28]. Figure 6.2c displays a time frame that was too short, as these individual droplets did not merge as the solvents evaporated prior to inter-droplet flow.

6.3.2 Response to Moisture Content

The impedance of the fabricated devices was characterized towards RH at different frequencies. After checking the response of type 1, we discarded it because it did not show a consistent response during consecutive tests, which can be attributed to the fact that these fabrication parameters resulted in

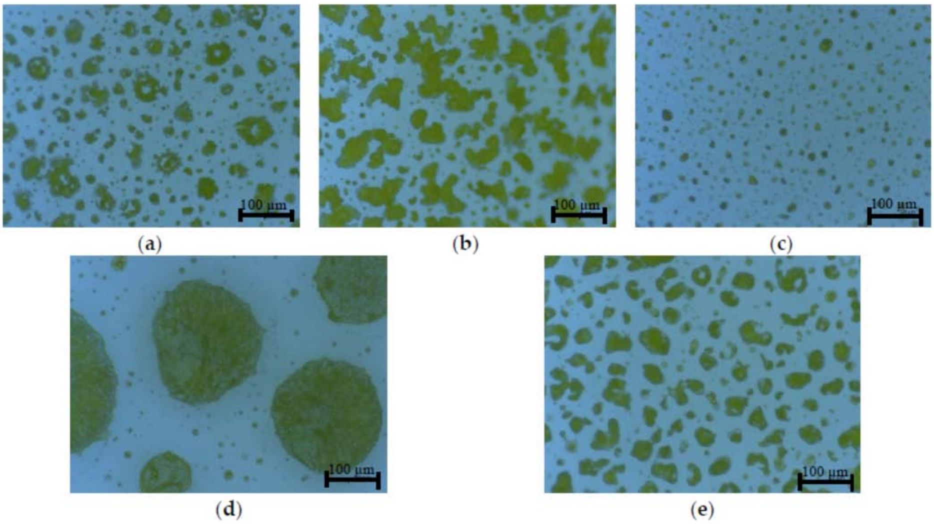

Figure 6.2: Optical microscope images for the spray coating with the different fabrication parameters: type 1 (a); type 2 (b); type 3 (c); type 4 (d); type 5 (e).

a too sparsely deposited film. From now on, the manuscript only presents the characterization data of type 2–5 sensors. Figure 6.3 illustrates the impedance response at 100 Hz for IDEs with an interspacing of 300μm. The individual frequency response of each device is shown in Figure A.2 (see Appendix A). As can be seen, the responses were as expected; the sensor started with a capacitive behavior, and when the RH increased, it changed to a resistive one. In a previous work [20], the device changed its behavior at a RH value of 60%; however, in this work the RH value at which this change occurred varied from 40% to 60% depending on the type of deposition. For deposition types 2 and 4, the trigger value was similar (around 40%), and the same happened with types 3 and 5 which changed around 60%.

As can be appreciated in Figure 6.2, deposition types 2 and 4 were more uniform than the other two. The drop size was medium, around 50μm in type 4 and 100μm in type 2. In the case of type 3 the drops were smaller, around 10μmand more expatiated. This means that to reach the same conductivity between the IDE fingers, K-Pery needs to be more conductive as there will be less conductive surface area between fingers. In the case of type 5, the drops had a diameter of around 250μm and big spaces between them. Due to these big spaces, the fingers can contact only one drop or part of them; thus, as occurs with type 3, there is less active surface area between fingers that needs to be compensated for with higher RH values. Apart from the trigger

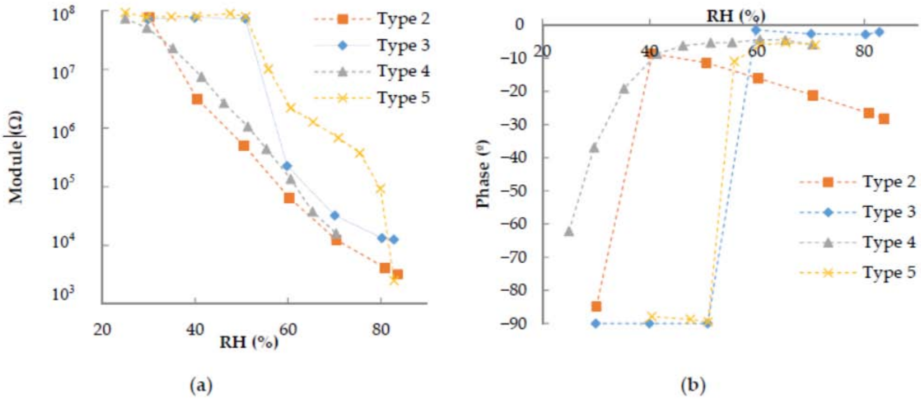

Figure 6.3: Impedance response towards RH at 100 Hz and 40 °C for the different deposited layers with distance between consecutive fingers of 300 μm: (a) module and (b) phase.

value, there are other differences in the response of the devices. For example, the type 4 coating response was smoother than others. This behavior can be explained by the different drop density with respect to type 2. The same process seen in type 3 to reach enough conductivity between the IDE fingers happened here; however, as the distribution in type 4 was more uniform and with bigger drops than in type 3, the response was a smoother change instead of a higher trigger value.

The other fabrication parameter that we studied in this work was the interspacing of IDEs. Figure 6.4 presents the impedance response for type 3 and 5 with interspacing of 300μm and 400μm. The finger width was fixed at 200μm in both cases, and the measuring frequency was 100 Hz. The individual response in frequency is shown in Figure A.3 (see Appendix A). In the case of type 3 (Figure 6.4a,b), the increase in interspacing implies an increase in the trigger value. As happened with higher spaces between drops, with increasing interspacing, the increase in resistance has to be compensated with more RH, so the trigger is at a higher RH value.

In the case of type 5, the interspacing changed the response in the opposite direction, the trigger value was reduced to 50%, and the response was less abrupt than in the other cases.

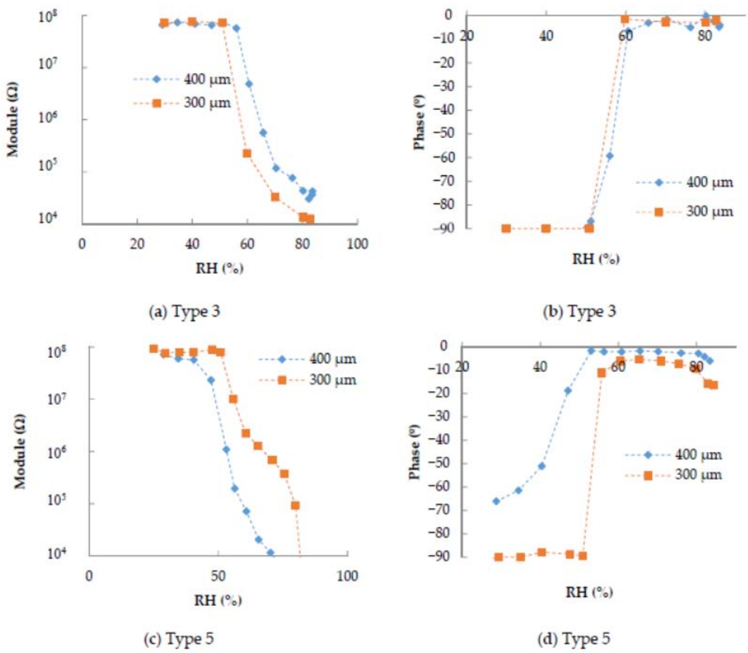

Figure 6.4: Impedance response towards RH at 100 Hz and 40 °C for different spacing: (a) module and (b) phase for type 3; (c) module and (d) phase for type 5.

6.4 Conclusions

Starting from a previous work [20], here two fabrication parameters of K-Pery humidity sensors were analyzed with the objective of being able to control the trigger value of the devices during the fabrication process. The study was centered on the coating parameters and the interspacing of IDEs.

The results show that spray coating allows for the varying of drop sizes and dispersion, which results in different trigger values. These values depend on the amount of material between fingers. As the K-Pery between fingers reduces, bigger RH values are needed to change the state of the device. In this way, we were able to change the trigger value from an RH value of 20% up to a value of 60% depending on the spray parameters used.

The interspacing analysis results showed that the trigger value is also controllable as the increase in the interspace of the IDE reflects an increase in the RH trigger value of the device. By varying this parameter, we were able to change the trigger value; however, the results were not consistent in the different spray parameters tested.

With these results, we demonstrate that K-Pery not only allows for the creation of a humidity actuator, but it is also possible to change the humidity value, which modifies the actuator state, by changing the parameters of the sprayed layer.

Bibliography

[1] C. Costa, F. Antonucci, F. Pallottino, J. Aguzzi, D. Sarriá, and P. Menesatti, "A review on agri-food supply chain traceability by means of rfid technology," *Food and Bioprocess Technology*, vol. 6, no. 2, pp. 353–366, 2 2013.

[2] B. Song, M. H. Azarian, and M. G. Pecht, "Effect of temperature and relative humidity on the impedance degradation of dust-contaminated electronics," *Journal of The Electrochemical Society*, vol. 160, no. 3, pp. C97–C105, 2013.

[3] J. Paasi, S. Nurmi, R. Vuorinen, S. Strengell, and P. Maijala, "Performance of esd protective materials at low relative humidity," *Journal of Electrostatics*, vol. 51-52, pp. 429–434, 5 2001.

[4] I. Khajenasiri, A. Estebsari, M. Verhelst, and G. Gielen, "A review on internet of things solutions for intelligent energy control in buildings

for smart city applications," *Energy Procedia*, vol. 111, pp. 770–779, 3 2017.

[5] Z. Chen and C. Lu, "Humidity sensors: A review of materials and mechanisms," *Sensor Letters*, vol. 3, no. 4, pp. 274–295, 12 2005.

[6] E. Traversa, "Ceramic sensors for humidity detection: the state-of-the-art and future developments," *Sensors and Actuators B: Chemical*, vol. 23, no. 2-3, pp. 135–156, 2 1995.

[7] H.-S. Kim, J. H. Kim, S.-Y. Park, J.-H. Kang, S.-J. Kim, Y.-B. Choi, and U. S. Shin, "Carbon nanotubes immobilized on gold electrode as an electrochemical humidity sensor," *Sensors and Actuators B: Chemical*, vol. 300, p. 127049, 12 2019.

[8] A. Lyuleeva, T. Helbich, M. Bobinger, B. Rieger, M. Becherer, P. Lugli, and A. Rivadeneyra, "Functionalized and oxidized silicon nanosheets: Customized design for enhanced sensitivity towards relative humidity," *Sensors and Actuators B: Chemical*, vol. 283, pp. 451–457, 3 2019.

[9] J.-M. Tulliani, B. Inserra, and D. Ziegler, "Carbon-based materials for humidity sensing: A short review," *Micromachines*, vol. 10, no. 4, p. 232, 3 2019.

[10] M. A. Najeeb, Z. Ahmad, and R. A. Shakoor, "Organic thin-film capacitive and resistive humidity sensors: A focus review," *Advanced Materials Interfaces*, vol. 5, no. 21, p. 1800969, 11 2018.

[11] G. Dubourg, A. Segkos, J. Katona, M. Radović, S. Savić, G. Niarchos, C. Tsamis, and V. Crnojević-Bengin, "Fabrication and characterization of flexible and miniaturized humidity sensors using screen-printed tio2 nanoparticles as sensitive layer," *Sensors*, vol. 17, no. 8, p. 1854, 8 2017.

[12] J.-R. Li, J. Sculley, and H.-C. Zhou, "Metal–organic frameworks for separations," *Chemical Reviews*, vol. 112, no. 2, pp. 869–932, 2 2012.

[13] J. Lee, O. K. Farha, J. Roberts, K. A. Scheidt, S. T. Nguyen, and J. T. Hupp, "Metal–organic framework materials as catalysts," *Chemical Society Reviews*, vol. 38, no. 5, p. 1450, 2009.

[14] J. Cepeda, S. Pérez-Yáñez, G. Beobide, O. Castillo, A. Luque, P. A. Wright, S. Sneddon, and S. E. Ashbrook, "Exploiting synthetic conditions to promote structural diversity within the scandium(iii)/pyrimidine-4,6-dicarboxylate system," *Crystal Growth & Design*, vol. 15, no. 5, pp. 2352–2363, 5 2015.

[15] V. Guillerm, D. Kim, J. F. Eubank, R. Luebke, X. Liu, K. Adil, M. S. Lah, and M. Eddaoudi, "A supermolecular building approach for the design and construction of metal–organic frameworks," *Chem. Soc. Rev.*, vol. 43, no. 16, pp. 6141–6172, 7 2014.

[16] Y. Gao, P. Jing, N. Yan, M. Hilbers, H. Zhang, G. Rothenberg, and S. Tanase, "Dual-mode humidity detection using a lanthanide-based metal–organic framework: towards multifunctional humidity sensors," *Chemical Communications*, vol. 53, no. 32, pp. 4465–4468, 2017.

[17] J. M. Stangl, D. Dietrich, A. E. Sedykh, C. Janiak, and K. Müller-Buschbaum, "Luminescent mof polymer mixed matrix membranes for humidity sensing in real status analysis," *Journal of Materials Chemistry C*, vol. 6, no. 34, pp. 9248–9257, 2018.

[18] M. Zhuo, Y. Chen, J. Sun, H. Zhang, D. Guo, H. Zhang, Q. Li, T. Wang, and Q. Wan, "Humidity sensing properties of a single sb doped sno2 nanowire field effect transistor," *Sensors and Actuators B: Chemical*, vol. 186, pp. 78–83, 9 2013.

[19] S. P. Lee and K.-J. Park, "Humidity sensitive field effect transistors," *Sensors and Actuators B: Chemical*, vol. 35, no. 1-3, pp. 80–84, 9 1996.

[20] J. M. Seco, E. San Sebastián, J. Cepeda, B. Biel, A. Salinas-Castillo, B. Fernández, D. P. Morales, M. Bobinger, S. Gómez-Ruiz, F. C. Loghin, A. Rivadeneyra, and A. Rodríguez-Diéguez, "A potassium metal-organic framework based on perylene-3,4,9,10-tetracarboxylate as sensing layer for humidity actuators," *Scientific Reports*, vol. 8, no. 1, 12 2018, [Online; accessed 2019-03-07]. [Online]. Available: http://www.nature.com/articles/s41598-018-32810-7

[21] N. Y. Abu-Thabit and A. S. H. Makhlouf, "Fundamental of smart coatings and thin films: synthesis, deposition methods, and industrial applications," in *Advances in Smart Coatings and Thin Films for Future Industrial and Biomedical Engineering Applications*. Elsevier, 2020, pp. 3–35, dOI: 10.1016/B978-0-12-849870-5.00001-X. [Online]. Available: https://linkinghub.elsevier.com/retrieve/pii/B978012849870500001X

[22] G. Barroso, Q. Li, R. K. Bordia, and G. Motz, "Polymeric and ceramic silicon-based coatings – a review," *Journal of Materials Chemistry A*, vol. 7, no. 5, pp. 1936–1963, 2019.

[23] J. Park, K. Shin, and C. Lee, "Roll-to-roll coating technology and its applications: A review," *International Journal of Precision Engineering and Manufacturing*, vol. 17, no. 4, pp. 537–550, 4 2016.

[24] V. Chernikova, O. Shekhah, and M. Eddaoudi, "Advanced fabrication method for the preparation of mof thin films: Liquid-phase epitaxy approach meets spin coating method," *ACS Applied Materials & Interfaces*, vol. 8, no. 31, pp. 20 459–20 464, 8 2016.

[25] N. Malik, N. Elool Dov, G. de Ruiter, M. Lahav, and M. E. van der Boom, "On-surface self-assembly of stimuli-responsive metallo-organic films: Automated ultrasonic spray-coating and electrochromic devices," *ACS Applied Materials & Interfaces*, vol. 11, no. 25, pp. 22 858–22 868, 6 2019.

[26] H. K. Arslan, O. Shekhah, J. Wohlgemuth, M. Franzreb, R. A. Fischer, and C. Wöll, "High-throughput fabrication of uniform and homogenous mof coatings," *Advanced Functional Materials*, vol. 21, no. 22, pp. 4228–4231, 11 2011.

[27] A. Rivadeneyra, J. Fernández-Salmerón, M. Agudo, J. A. López-Villanueva, L. F. Capitan-Vallvey, and A. J. Palma, "Design and characterization of a low thermal drift capacitive humidity sensor by inkjet-printing," *Sensors and Actuators B: Chemical*, vol. 195, pp. 123–131, 5 2014.

[28] T. Breinlinger and T. Kraft, "A simple method for simulating the coffee stain effect," *Powder Technology*, vol. 256, pp. 279–284, 4 2014.

Chapter 7

Selectivity of Relative Humidity Using CP Based on S-Block Metal Ions

Amalia García-García[1], Víctor Toral[2], José F. Quílez del Moral[3], Alberto Galisteo Pretel[3], Diego P. Morales[2], Alfonso Salinas-Castillo[4], Javier Cepeda[5], Duane Choquesillo-Lazarte[6], Marco Bobinger[7], José F. Salmerón[2], Almudena Rivadeneyra[2], Antonio Rodríguez-Diéguez[1]

1 – Department of Inorganic Chemistry, Faculty of Science, University of Granada, 18071 Granada, Spain;

2 – Department of Electronics and Computer Technology, Faculty of Science, University of Granada 18071 Granada, Spain

3 – Department of Organic Chemistry, Faculty of Science, University of Granada, 18071 Granada, Spain

4 – Department of Analytical Chemistry, Faculty of Science, University of Granada, 18071 Granada, Spain

5 – Department of Applied Chemistry, Faculty of Chemistry, University of the Basque Country (UPV/EHU)

6 – Laboratorio de Estudios Cristalográficos, IACT, CSIC-Universidad de Granada, Avda. de las Palmeras 4, Armilla, 18100 Granada, Spain

7 – Institute for Nanoelectronics, Technical University of Munich, 80333 Munich, Germany

Published in Sensors 2022, vol. 22, art. 1664

- Received: 16 October 2020; Accepted: 3 December 2020; Published: 7 December 2020
- DOI: 10.3390/s22041664
- Impact factor: 3.847
- JCR Rank: 16/76, category "Instruments and Instrumentation" (Q1, 2021)

Abstract: Herein, we present the syntheses of a novel coordination polymer (CP) based on the perylene-3,4,9,10-tetracarboxylate (pery) linkers and sodium metal ions. We have chosen sodium metal center with the aim of surmising the effect that the modification of the metal ion may have on the relative humidity (RH) experimental measurements of the material. We confirm the role of the ions in the functionalization of the deposited layer by modifying their selectivity towards moisture content, paving the way to the generation of sensitive and selective chemical sensors.

Keywords: flexible substrate; spray deposition; moisture content; interdigitated electrodes; screen printing; sodium; perylene

7.1 Introduction

Water vapor is present in the air and is the most varied component. At the same time, atmospheric conditions are essential for many processes of our daily life, especially in an industry environment [1]. For example, electronics or food industry need this type of control during fabrication and transportation. Due to this fact, the sensing of Relative Humidity (RH) with integrated and cost-effective solutions is of great interest for broad types of industries.

RH sensors are typically based on ceramic materials, such as aluminum oxide, semiconducting materials, such as SiO_2, or polymers [1, 2]. Additionally, 2D materials have appeared as a solution to flexible and highly integrable sensors such as, for example, carbon nanotubes [3] or silicon nanosheets [4]. More recently, Coordination Polymer (CP), including Metal-Organic Framework (MOF), are a relatively new class of materials that have attracted great interest due to their structural and topological diversity, as well as the properties that arise from their structural features [5, 6, 7, 8]. This class of materials has also been used for RH sensors, as shown in [9], where a MOF is used to create a luminescent and impedance spectroscopy sensor. In [10], a luminescent RH based on MOF polymer is presented.

These sensors are typically based on a variation of capacitance or resistance of the materials, *i.e.*, they are passive sensors. Active devices that react to RH variations are not so common and are normally oriented to mechanical systems [11]. In the case of electronics devices, several works exist on RH sensing based on Field Effect Transitor (FET) [12, 13]. Additionally, organic field effect transistors (OFETs) used as humidity sensor can be found in the literature [14, 15, 16, 17]. However, these devices are mainly based on the variation of threshold voltage or conductivity of the channel, so they cannot be considered an active device. MOFs have been demonstrated to open the possibility of an electronic humidity actuator [18, 19]. In previous works, the use of K-Pery MOF to create a humidity actuator was uncovered [20]. However, it was not studied if the response of K-Pery was due to the response of the perylene or the metal center employed.

For this reason, we decided to study this point, demonstrating the possibility of modifying perylene-based MOF to react to humidity by using different metal centers. In this work, we present a new CP based on the perylene derivative (pery) ligand and sodium metal ions to investigate the possibilities to control the selectivity to RH of this material. Sodium was used to modulate the metal–organic architecture of the K-Pery material due to the smaller ion size. Furthermore, spray coating was employed as a more repeatable method to preserve the material, and the temperature dependence was

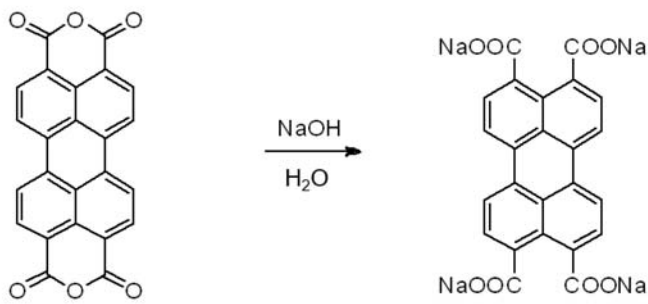

Figure 7.1: Synthesis of Na-Pery

also analyzed. Spray coating is also a scalable fabrication method, which brings the possibility of easily translating these devices for mass production. The rest of the paper continues with materials and methods in section 7.2. Then, in section 7.3, the results are presented. section 7.4 continues with the discussion of the results. Finally, conclusions derived from this work are exposed in section 7.5.

7.2 Materials and Methods

7.2.1 Synthesis of Sodium-Based Metal-Organic Framework

To a solution of perylene dianhydride (392 mg, 1 mmol) in 20 mL of distilled water, a solution of 166 mg (4 mmol) of NaOH in 10 mL of distilled water (Figure 7.1) was added. The mixture reaction was stirred at room temperature for 15 min. After this time, the color of the solution, initially dark red, turned to orange. This green solution was UV active. Solvent was then removed under infrared light for 24 h to afford a 96% yield (498 mg, 0.96 mmol) of micro-crystalline powders of Na-Pery.

The resulting solid was studied by elemental analysis (ELEMENTAR VARIO EL III, equipped with a thermal conductivity detector) combined with inductively coupled plasma (ICP-AES, carried out on a Horiba Yobin Yvon Activa spectrometer), from which the content of the solid could be estimated. The obtained results are concordant with the $C_{48}H_{80}Na_5O_{47}$ formula (Calcd.: C, 37.83; H, 5.29; Na, 7.54. Found: C, 38.05; H, 4.92; Na, 7.68), confirming the purity of the sample.

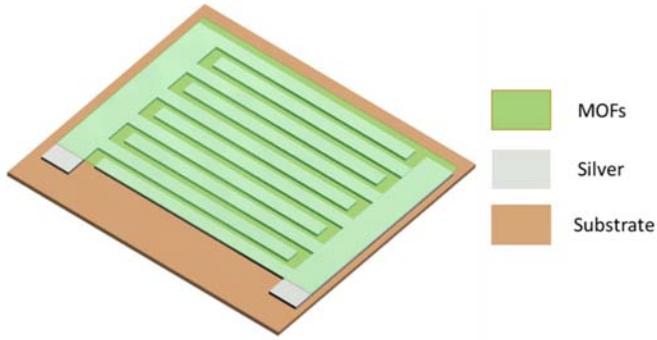

Figure 7.2: Schematic representation of sensing device.

7.2.2 Preparation of the Ink and Spray Coating

The tested sensing material, Na-Pery, was dissolved in deionized (DI) water in a weight content of 0.6 wt%, respectively. In order to dissolve the material, a bath sonication treatment for a duration of 5 min was applied (Bransonic® Ultrasonic Baths). The as-prepared solution was used as inks and sprayed onto polyimide (KaptonHN) substrate from DuPontTM, employing a hand-held airbrush Triplex II from Gabbert (Leipzig, Germany). The sample was attached to a hot plate Rt2 from Thermofisher Scientific™at a temperature of 90 °C to evaporate the solvent. Without any post-treatment, the sample was used as a sensor, after the deposition.

7.2.3 Contacting the films

Electrical contacts were formed to the sensing materials by screen printing highly conductive silver-based (product name: 1010 from Loctite) Inter-Digitated Electrodes (IDE) structures using a polyester-based mesh with a mesh count of 120 T/cm, as described [21]. The device is based in three layers, a polyimide substrate, silver screen-printed IDE and deposited CP. Over this IDE, the compound is deposited covering all the fingers to create a uniform layer. In Figure 7.2, the device is shown schematically. The flexibility and conformability area are desired features in many applications, such as wearables and packaging. The conformal substrate employed in this device provides the fabricated sensor with a certain level of both characteristics, expanding the range of applications where such device can be integrated.

The dimensions were selected after printing tests of several combinations of IDE finger widths and spacing (starting from 50 μm to 400 μm). We selected the best compromise of minimal dimensions and high reproducibility.

Table 7.1: Comparison of theoretical and experimentally determined atomic concentrations for Na-Pery.

Element	Atomic Mass	Theoretical Atomic Conc.	Experimental Atomic Conc.
C	12	67 %	60 %
O	16	22 %	28 %
Na	22	11 %	12 %

In the case of the selected layout, more than 95% of the fabricated IDEs were fully printed without a short circuit and high resolution.

7.2.4 Single crystal X-ray Diffraction

Measured crystal was prepared under inert conditions immersed in perfluoropolyether as a protecting oil for manipulation. A suitable crystal was mounted on MiTeGen Micromounts™, and this sample was used for data collection. Data for the compound were collected with a Bruker D8 Venture diffractometer with a photon detector equipped with graphite monochromated MoKα radiation (λ = 0.71073 Å). The data were processed with APEX3 suite [22]. The structure was solved by Intrinsic Phasing using the ShelXT program [23], which revealed the position of all non-hydrogen atoms. These atoms were refined on F2 by a full-matrix least-squares procedure using anisotropic displacement parameters [24]. All hydrogen atoms were located in difference Fourier maps and included as fixed contributions riding on attached atoms with isotropic thermal displacement parameters 1.2 or 1.5 times those of the respective atom. The OLEX2 software was used as a graphical interface [25]. As a consequence of the pseudosymmetries, the least-squares refinements of the structure are not stable, and the use of restraints was required. Some ISOR and RIGU commands had to be used to obtain reasonable displacement parameters for selected non-hydrogen atoms. Crystallographic data for the reported structure have been deposited with the Cambridge Crystallographic Data Center as supplementary publication no. CCDC 2130794. Additional crystal data are shown in Table 7.1. Copies of the data can be obtained free of charge at http://www.ccdc.cam.ac.uk (accessed on 24 December 2021).

7.2.5 Powder XR Diffraction

The single crystals of Na-Pery were gently ground mixed within oil in an agate mortar and then deposited with care in the hollow of an aluminum holder equipped with a zero-background plate. Diffraction data (Cu Kα, λ =

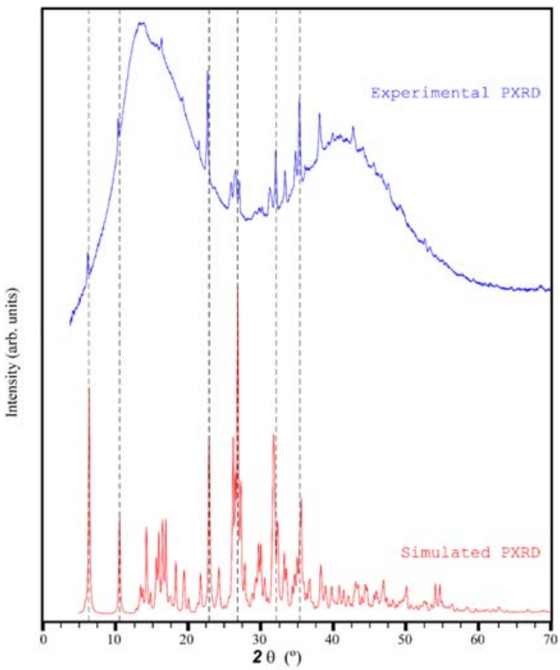

Figure 7.3: Comparison of the experimental and simulated PXRD patterns of Na-Pery.

1.5418 Å) were collected on a $\theta : \theta$ Bruker AXS D8 vertical scan diffractometer equipped with primary and secondary Soller slits, a secondary-beam-curved graphite monochromator, a Na(Tl)I scintillation detector, and pulse height amplifier discrimination. The generator was operated at 40 kV and 40 mA. A visual comparison of the experimental and simulated (from single crystal structure) patterns confirms the purity of the bulk. It must be taken into account that only the most intense peaks could be identified due to the strong background signal derived from the oil used in the preparation of the sample, although their positions fit well with those of the simulated pattern (Figure 7.3).

7.2.6 X-ray Photoelectron Spectroscopy

X-ray photoelectron spectroscopy (XPS) measurements were performed at a base pressure of 5×10^{-10} mbar using monochromatic Kα radiation from an aluminum anode that is operated at an electrical input power of 350 W. The spectra were acquired using a SPECS (SPECS GmbH) Phoibos hemispherical analyzer at a pass energy of 30 eV with an energy resolution of 0.05 eV. The raw data were processed using the software CasaXPS from Casa Software Ltd. (Teignmouth, UK). The backgrounds of the spectra were removed by Shirley background subtraction [26].

7.2.7 SEM Imaging

Scanning electron microscope (SEM) images were recorded with an NVision40 FESEM from Carl Zeiss (Oberkochen, Germany) at an acceleration voltage of 7 kV, an extraction voltage of 5 kV, and a working distance of 5–6 mm, which was optimized to achieve the best image quality.

7.2.8 Device characterization

The sheet resistances were measured using a four-point probe head from Jandel (Linslade, UK) connected to a B2901A Keysight (Santa Rosa, CA, USA) source measuring unit (SMU). A constant current of 1 mA was sourced for all measurements. The thicknesses were measured using a DekTak XT profilometer from Bruker (Billerica, MA, USA).

To measure the impedance of the device, a SubMiniature version A (SMA) male connector was glued to electrodes using silver paste. Measurement was carried out with an impedance analyzer (Keysight E4990A). The measurement was conducted at frequencies from 100 Hz to 10 MHz and an amplitude of 500 mV with 0 DC voltage. A calibration was carried out to compensate parasitic elements, as the one performed previously [27]. To automatize the measurements, LabVIEW 2016 was used to control the impedance analyzer.

Temperature and humidity during measurements were controlled in a climatic chamber (VLC4006), and monitorization was conducted with the climatic chamber sensors system. The moisture content was ramped up in 10% steps and kept for 1 h to ensure uniform distribution in the whole chamber volume. All tests were performed 3 times for 2 different fabricated devices.

7.3 Results

7.3.1 Structural description of the CP

The conventional reaction of the appropriate amount of 3,4,9,10-perylenetetracarboxylic acid (1 mmol) with NaOH (4 mmol) in water produced prismatic orange crystals of Na-Pery. The crystal structure was determined using single-crystal X-ray diffraction, and its molecular formula is:

$\{[Na_5(ptca)(H_2O)_{18}]\cdot{}_{13}H_2O\cdot H_2ptca\}_n$

This compound, unlike the previous published K-Pery MOF [20], crystallizes in the P-1 space group and is described as a 2D-layered structure made of sodium atoms bridged by $(ptca)^{4-}$ linkers and water molecules (Figure 7.4). In this CP, three different six-coordinated ions are present, all of which possess NaO_6 environments formed by water and/or carboxylate oxygen atoms. Na1 and Na2 atoms are bridged to one another by some of the water molecules, which act as $\mu{-}OH_2$ double bridges, giving rise to infinite chains that run parallel to the a axis. On the other hand, one of the water molecules coordinated to Na2 atom that does not take part in the mentioned chain acts as bridge to join to Na3 atoms which, being disordered into two equivalent positions close to an inversion center, complete their hexa-coordination by coordinating to (ptca)4- linkers. Therefore, each $(ptca)^{4-}$ linker bridges two Na3 atoms through carboxylate groups sited on opposite sides of the ligand to render 1D arrays in the [0-1-1] direction, which are, hence, cross-linked with the chains involving Na1 and Na2 atoms to build the 2D layers. Between $(ptca)^{4-}$ linkers, where there is a distance of 6.79 Å, additional protonated ligand (H_2ptca) molecules are intercalated by means of strong π–π interactions involving the electron clouds of the aromatic rings. Finally, crystallization water molecules occupy the voids of the crystal structure by establishing hydrogen bonding interactions with protonated/deprotonated carboxylate groups and coordinated water molecules.

7.3.2 Characterization of the CP

The XPS survey scan and the high resolution XPS scan of the C 1 s transition are shown in Figure 7.5 and Figure 7.6 for Na-Pery, respectively. The material was deposited onto polished and doped p-type silicon substrate to prevent charging. From these spectra, it can be seen that Na is present for the Na-Pery sample, which can be recognized by the large peak with a binding energy around 1074 eV [28] that is associated with the Na 1 s transition. Besides this contribution, there is only a negligible amount of carbon associated with the C 1 s transition at a binding energy of 284 eV [29], which is due to contamination and trace residuals by organic solvents. For the C 1 s spectrum, multiple contributions at higher binding energies that are in accordance with the structural formula shown in Figure 7.1 can be seen in the high-resolution scans shown in Figure 7.5. The C 1 s spectra

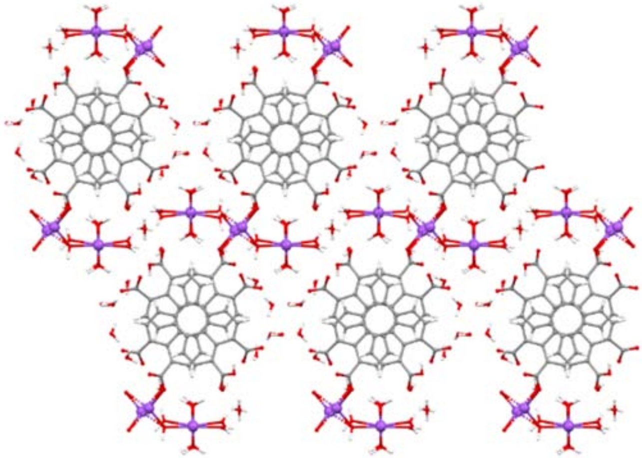

Figure 7.4: View down the a axis of Na-Pery. Color code: H = white, O = red, C = grey, Na = purple.

are composed of C−C sp^2 hybridized carbon bonds (284.6 eV), C−C sp^3 hybridized carbon bonds (285.6 eV), the carbon-oxygen compounds C−O (286.6 eV), O−C−O (287.6 eV) and O−C=O (289 eV) as well as π-$\pi*$ transitions (291 eV). The atomic concentrations for Na-Pery were determined from the XPS survey scan and are summarized in Table 7.1 along with the theoretical atomic concentrations. The experimental and theoretical values are similar. The increased contribution from carbon in the experimental concentration can be ascribed to organic residuals.

The peak at 534 eV is due to the O 1 s transition and attributed partially to a residual thin water layer that is present on all samples [30]. Besides the water film, there are also contributions from oxygen atoms in the Na-Pery sample. SEM images of the deposited films on the substrate are shown in Figure 7.7.

In Figure 7.8, the deposited layers of Na-Pery are shown by using the microscope at a magnification of 20 ×. In this photograph, it may be observed that the solid possesses low crystallinity in view of the small particle size, which is in agreement with the wide diffraction maxima and the irregular background observed in the diffractogram.

7.3.3 Response to Moisture Content

After printing the electrodes, they showed a thickness of 3.9 μm and a sheet resistance of 79 ± 10 mΩ/sq. The new CP material was drop-casted to

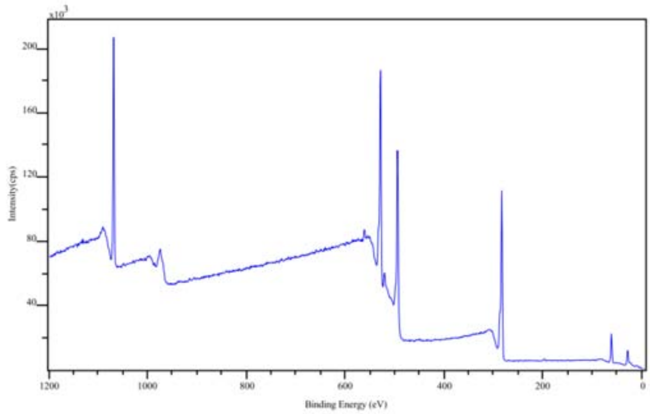

Figure 7.5: XPS survey scan for Na-Pery sample

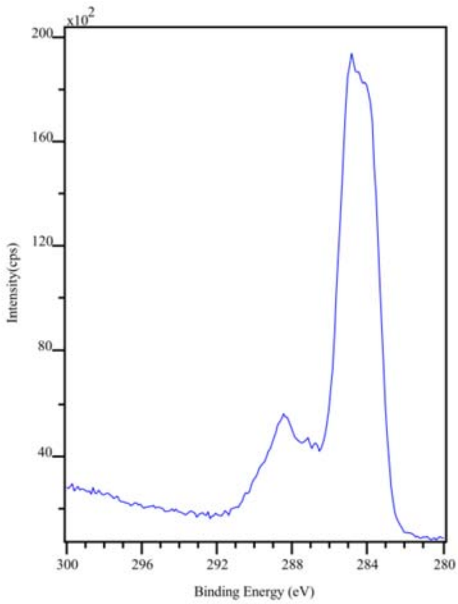

Figure 7.6: High-resolution XPS scan of the C 1 s transition for (left) Na-Pery. See the text for the contributions at higher-binding energies.

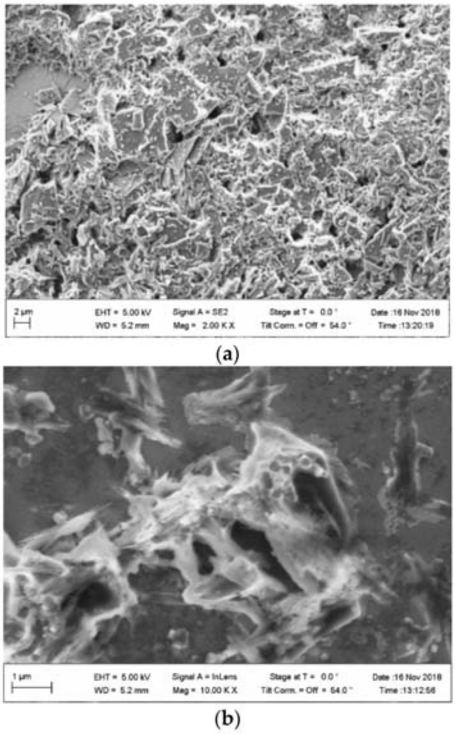

Figure 7.7: SEM image of Na-Pery (a) at 2 kx and (b) at 10 kx.

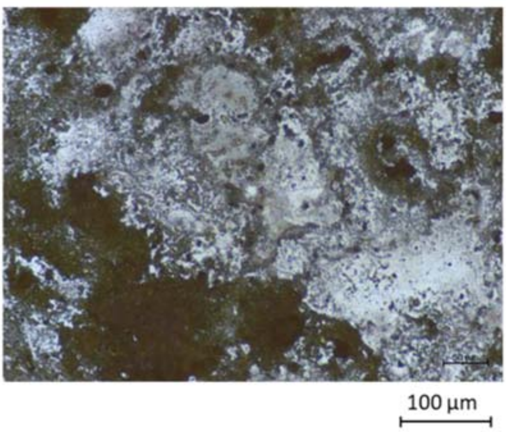

Figure 7.8: Microscope images of Na-Pery

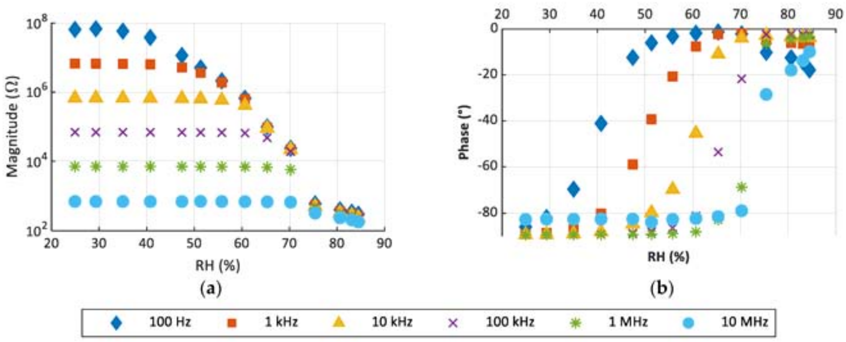

Figure 7.9: Impedance response towards RH at 40 °C. (a) Magnitude and (b) phase for Na-Pery drop-casted.

test its response to RH. Given that Na-Pery responded, it was tested with spray deposition. Figure 7.9 shows the response of the material tested when drop-casted. As can be seen in Figure 7.9a,b, Na-Pery responds to RH as expected from previous work [20]. In this sense, the response of both Na-Pery and K-Pery below 40% is mainly capacitive, whereas the sensors show a drastic change in the behavior for higher RHs, where the resistive component drops about 5 orders of magnitude, and they become quite conductive. As happened with K-Pery, the response of Na-Pery varies with the frequency excited but always in isolating the state for low RH values and conducting states with higher RH.

Spray coating is a more controllable and repeatable system to deposit CP. Na-Pery was tested with spray coating too. In Figure 7.10, the results for this deposition are shown. As happened with the drop-casted device, a response to RH is observed. However, small differences in this response are appreciated. First, lower conductivity is observed in the case of spray coating as the maximum phase for spray coating is -6.5°, while for drop-casted it is -1.27°. Additionally, the response of the drop-casted device is slightly more abrupt as the high conductive state is reached with less change in RH. These two differences can be explained as a result of the deposition method. With spray coating, the resulted layer has small drops with gapes in between them; this makes it so that when the sensing layer changes its state, less conducting surface is available, so to reach the same state a higher RH level is needed.

The sensitivity of the sensor was studied in the region where the phase changes from capacitive (about -80°) to resistive (about -10°). Actually, outside this region, the sensor response barely varies. The sensitivity at different operating frequencies is shown in Table 7.2, where the curves were

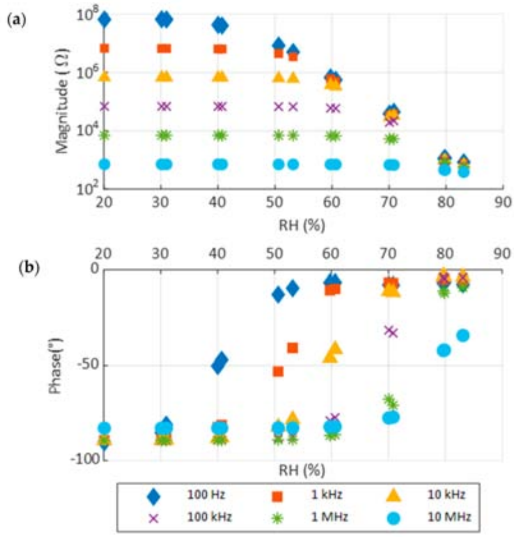

Figure 7.10: Impedance response towards RH at 40 °C. (a) Magnitude and (b) phase for spray-deposited Na-Pery.

Table 7.2: Sensitivity of the sensor in the linear response for the different frequencies and range of RH of the linear phase.

Frequency	Sensitiviy(Ω/%RH)	Range of RH (%)
100 Hz	-2.89×10^6	29-51
1 kHz	-2.91×10^5	41-61
10 kHz	-3.90×10^5	51-65
100 kHz	-4.38×10^3	61-75
1 MHz	-610	65-75
10Mhz	-501	71-83

fitted with an exponential model. As can be seen, the sensitivity drastically reduces its value as the frequency increases, achieving a maximum sensitivity of 2.89 × 106 (Ω/%RH) in the range of 29% to 51% at 100 Hz. It should be noted that the range of RH in which the variation can be linearized is reduced as the frequency increases. In addition, the initial value of this range is higher as the frequency increases

7.3.4 Response to Temperature

Tests above were carried out at controlled temperature of 40 °C; however, the variation of response with temperature was not analyzed. In Figure 7.11,

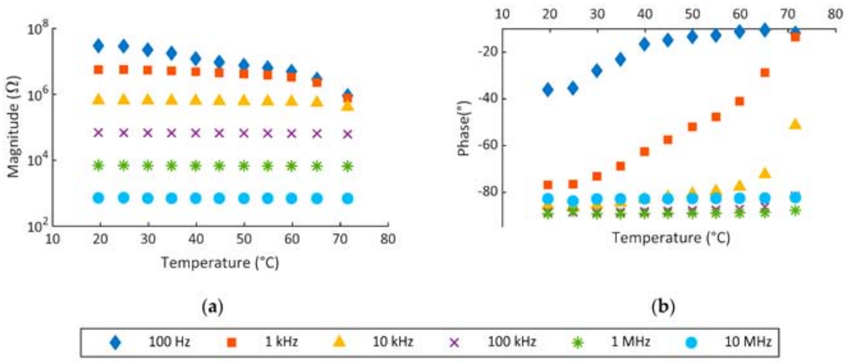

Figure 7.11: Impedance response towards temperature at RH of 55%. (a) Magnitude and (b) phase for spray-deposited Na-Pery.

the results of these tests are shown. These tests were conducted under an RH controlled condition of 55%. As can be seen, the temperature increases conductivity, especially at lower frequencies. This response is not enough to make the device totally conductive; however, this variation will make the system react at lower RH. At 100 Hz, a saturation effect in phase response is observed for temperatures above 35 °C. Magnitude variation is also higher at lower frequencies; however, it is much lower in comparison to RH response.

7.4 Discussion

The results demonstrate that perylene is not reactive to RH on its own. However, it is possible to functionalize it using different metallic centers. As seen before, perylene combined with sodium reacts to humidity increasing drastically its conductivity when RH is over 40%. The impedance measurements show that the magnitude impedance is reduced up to 5 orders of magnitude and phase changes from -90° to 0°, which is equivalent to pass from a capacitive response to a resistive one, in the case of Na-Pery. This difference in response can be explained due to the different crystalline structure presented by these materials, which directly affects the solubility of alkali metals in water. While in the case of perylene, the structure must present strong stacking interactions between the aromatic rings of the ligand, making their dissolution difficult, in the case of Na-Pery, there are no such interactions, and the coordination to the metal ion generates a trigonal structure with many molecules of water housed in the canals. In this case, sodium is a monovalent ion, similar to the published material of potassium. The sensitivity of the Na-Pery sensor shows higher values when operating at low frequencies, while the range in which the variation is exponential is reduced as the frequency is increased. This behavior of the sensor is consistent with the impedance values: its magnitude is lower with frequency, and the absolute variation in RH is also lower.

In previous work, K-Pery was shown as a RH actuator [20]. In such work, the K-Pery was drop-casted on screen-printed IDEs in an area of about 2 cm2. The response is quite similar to the one shown by Na-Pery, reacting around 40% RH and with a resistance in on mode around 100 Ω. In terms of temperature, both materials respond, reducing its resistivity, while for Na-Pery, the reduction is higher. Furthermore, in this work, we have made an optimization of the fabrication process by using spray coating and miniaturizing the sensor size. The deposit method employed to deposit the composite does not affect to our results and just modifies the smoothness of the device reaction. This difference is due to the characteristics of the layers created. When using spray coating, Na-Pery keeps in small drops so the electric currents found more resistance to travel from one to another electrode of IDE. Contrarily, when drop-casting, Na-Pery covers the IDE completely; therefore, the current has a bigger amount of material to travel for. However, the use of spray coating is very advantageous in terms of reproducibility and control of the process. Temperature usually affects the humidity sensors. In the case of Na-Pery, the temperature produces a small reaction of the device, increasing its conductivity, especially when the impedance is measured at low frequencies. Despite this reaction, it is much lower than the one by RH. The magnitude is reduced around 1 order of magnitude, which, in comparison to the 5 orders of RH response, is almost negligible.

7.5 Conclusions

In this paper, functionalization of CPs for humidity sensing has been studied. To do so, a CP with Na as metallic centers was created, and its impedance was measured at different RH values. The results show that Na-Pery reacts to humidity when RH is over 40%. These results demonstrate that the center used in the CP is able to modify its sensibility to ambient RH, comparing with the published potassium material. Additionally, the sensibility at temperature changes is modified with the center utilized. Na-Pery has a similar behavior to those with RH but with lower sensibility.

In the case of Na-Pery, the affection of using a different coating method, spray coating, was also analyzed. The study concluded with a similar behavior for drop-casting and spray coating while the spray coating response was less abrupt than the drop-casted sensor.

The use of CPs uncovered in this work can be extremely useful for many applications that need threshold humidity detection. This device can be used in circuits without powering it, which is a great advantage in front of typical RH sensors, which need external devices to read the sensor and check if it crosses the threshold. Furthermore, this device is flexible thanks to the use of conformal substrates, and it can be manufactured with printing techniques. New materials based on alkaline earth ions are being developed in our laboratory to study the effect of the charge of metal ion in modifying the physical properties of these systems.

Bibliography

[1] E. Traversa, "Ceramic sensors for humidity detection: the state-of-the-art and future developments," *Sensors and Actuators B: Chemical*, vol. 23, no. 2-3, pp. 135–156, feb 1995.

[2] Z. Chen and C. Lu, "Humidity sensors: A review of materials and mechanisms," *Sensor Letters*, vol. 3, no. 4, pp. 274–295, dec 2005.

[3] H.-S. Kim, J. H. Kim, S.-Y. Park, J.-H. Kang, S.-J. Kim, Y.-B. Choi, and U. S. Shin, "Carbon nanotubes immobilized on gold electrode as an electrochemical humidity sensor," *Sensors and Actuators B: Chemical*, vol. 300, p. 127049, dec 2019.

[4] A. Lyuleeva, T. Helbich, M. Bobinger, B. Rieger, M. Becherer, P. Lugli, and A. Rivadeneyra, "Functionalized and oxidized silicon nanosheets: Customized design for enhanced sensitivity towards relative humidity," *Sensors and Actuators B: Chemical*, vol. 283, pp. 451–457, mar 2019.

[5] J.-R. Li, J. Sculley, and H.-C. Zhou, "Metal–organic frameworks for separations," *Chemical Reviews*, vol. 112, no. 2, pp. 869–932, oct 2011.

[6] J. Lee, O. K. Farha, J. Roberts, K. A. Scheidt, S. T. Nguyen, and J. T. Hupp, "Metal–organic framework materials as catalysts," *Chemical Society Reviews*, vol. 38, no. 5, p. 1450, 2009.

[7] J. Cepeda, S. Pérez-Yáñez, G. Beobide, O. Castillo, A. Luque, P. A. Wright, S. Sneddon, and S. E. Ashbrook, "Exploiting synthetic conditions to promote structural diversity within the scandium(III)/pyrimidine-4,6-dicarboxylate system," *Crystal Growth & Design*, vol. 15, no. 5, pp. 2352–2363, apr 2015.

[8] V. Guillerm, D. Kim, J. F. Eubank, R. Luebke, X. Liu, K. Adil, M. S. Lah, and M. Eddaoudi, "A supermolecular building approach for the design and construction of metal–organic frameworks," *Chem. Soc. Rev.*, vol. 43, no. 16, pp. 6141–6172, jul 2014.

[9] Y. Gao, P. Jing, N. Yan, M. Hilbers, H. Zhang, G. Rothenberg, and S. Tanase, "Dual-mode humidity detection using a lanthanide-based metal–organic framework: towards multifunctional humidity sensors," *Chemical Communications*, vol. 53, no. 32, pp. 4465–4468, 2017.

[10] J. M. Stangl, D. Dietrich, A. E. Sedykh, C. Janiak, and K. Müller-Buschbaum, "Luminescent MOF polymer mixed matrix membranes for humidity sensing in real status analysis," *Journal of Materials Chemistry C*, vol. 6, no. 34, pp. 9248–9257, 2018.

[11] H. Arazoe, D. Miyajima, K. Akaike, F. Araoka, E. Sato, T. Hikima, M. Kawamoto, and T. Aida, "An autonomous actuator driven by fluctuations in ambient humidity," *Nature Materials*, vol. 15, no. 10, pp. 1084–1089, jul 2016.

[12] M. Zhuo, Y. Chen, J. Sun, H. Zhang, D. Guo, H. Zhang, Q. Li, T. Wang, and Q. Wan, "Humidity sensing properties of a single sb doped SnO2 nanowire field effect transistor," *Sensors and Actuators B: Chemical*, vol. 186, pp. 78–83, sep 2013.

[13] S. P. Lee and K.-J. Park, "Humidity sensitive field effect transistors," *Sensors and Actuators B: Chemical*, vol. 35, no. 1-3, pp. 80–84, sep 1996.

[14] N. V. V. Subbarao, M. Gedda, P. K. Iyer, and D. K. Goswami, "Enhanced environmental stability induced by effective polarization of a polar dielectric layer in a trilayer dielectric system of organic field-effect transistors: A quantitative study," *ACS Applied Materials & Interfaces*, vol. 7, no. 3, pp. 1915–1924, jan 2015.

[15] S. Wu, G. Wang, Z. Xue, F. Ge, G. Zhang, H. Lu, and L. Qiu, "Organic field-effect transistors with macroporous semiconductor films as high-performance humidity sensors," *ACS Applied Materials & Interfaces*, vol. 9, no. 17, pp. 14 974–14 982, apr 2017.

[16] Q. Zafar, S. M. Abdullah, M. I. Azmer, M. A. Najeeb, K. W. Qadir, and K. Sulaiman, "Influence of relative humidity on the electrical response of PEDOT:PSS based organic field-effect transistor," *Sensors and Actuators B: Chemical*, vol. 255, pp. 2652–2656, feb 2018.

[17] N. V. Subbarao, M. Gedda, P. K. Iyer, and D. K. Goswami, "Organic field-effect transistors as high performance humidity sensors with rapid response, recovery time and remarkable ambient stability," *Organic Electronics*, vol. 32, pp. 169–178, may 2016.

[18] A. Weiss, N. Reimer, N. Stock, M. Tiemann, and T. Wagner, "Surface-modified CAU-10 MOF materials as humidity sensors: impedance spectroscopic study on water uptake," *Physical Chemistry Chemical Physics*, vol. 17, no. 33, pp. 21 634–21 642, 2015.

[19] M. A. Andrés, M. T. Vijjapu, S. G. Surya, O. Shekhah, K. N. Salama, C. Serre, M. Eddaoudi, O. Roubeau, and I. Gascón, "Methanol and humidity capacitive sensors based on thin films of MOF nanoparticles," *ACS Applied Materials & Interfaces*, vol. 12, no. 3, pp. 4155–4162, jan 2020.

[20] J. M. Seco, E. S. Sebastián, J. Cepeda, B. Biel, A. Salinas-Castillo, B. Fernández, D. P. Morales, M. Bobinger, S. Gómez-Ruiz, F. C. Loghin, A. Rivadeneyra, and A. Rodríguez-Diéguez, "A potassium metal-organic framework based on perylene-3,4,9,10-tetracarboxylate as sensing layer for humidity actuators," *Scientific Reports*, vol. 8, no. 1, sep 2018.

[21] A. Albrecht, J. F. Salmeron, M. Becherer, P. Lugli, and A. Rivadeneyra, "Screen-printed chipless wireless temperature sensor," *IEEE Sensors Journal*, vol. 19, no. 24, pp. 12 011–12 015, dec 2019.

[22] B. APEX3, "Apex3 v2019. 1," 2019.

[23] G. M. Sheldrick, "Shelxt– integrated space-group and crystal-structure determination," *Acta Crystallographica Section A Foundations and Advances*, vol. 71, no. 1, pp. 3–8, jan 2015.

[24] ——, "Crystal structure refinement with shelxl," *Acta Crystallographica Section C Structural Chemistry*, vol. 71, no. 1, pp. 3–8, jan 2015.

[25] O. V. Dolomanov, L. J. Bourhis, R. J. Gildea, J. A. K. Howard, and H. Puschmann, "Olex2: a complete structure solution, refinement and analysis program," *Journal of Applied Crystallography*, vol. 42, no. 2, pp. 339–341, jan 2009.

[26] A. Herrera-Gomez, M. Bravo-Sanchez, O. Ceballos-Sanchez, and M. O. Vazquez-Lepe, "Practical methods for background subtraction in photoemission spectra," *Surface and Interface Analysis*, vol. 46, no. 10-11, pp. 897–905, mar 2014.

[27] A. Rivadeneyra, J. Fernández-Salmerón, M. Agudo, J. A. López-Villanueva, L. F. Capitan-Vallvey, and A. J. Palma, “Design and characterization of a low thermal drift capacitive humidity sensor by inkjet-printing,” *Sensors and Actuators B: Chemical*, vol. 195, pp. 123–131, may 2014.

[28] D. Briggs, R. Marbrow, and R. Lambert, “An XPS and UPS study of the interaction of oxygen with sodium-dosed ag(110),” *Surface Science*, vol. 65, no. 1, pp. 314–324, jun 1977.

[29] M. Seifert, J. E. B. Vargas, M. Bobinger, M. Sachsenhauser, A. W. Cummings, S. Roche, and J. A. Garrido, “Role of grain boundaries in tailoring electronic properties of polycrystalline graphene by chemical functionalization,” *2D Materials*, vol. 2, no. 2, p. 024008, may 2015.

[30] M. Bobinger, J. Mock, P. L. Torraca, M. Becherer, P. Lugli, and L. Larcher, “Tailoring the aqueous synthesis and deposition of copper nanowires for transparent electrodes and heaters,” *Advanced Materials Interfaces*, vol. 4, no. 20, p. 1700568, aug 2017.

Chapter 8

A versatile wearable based on reconfigurable hardware for biomedical measurments

Víctor Toral[1], Francisco J. Romero[2], Encarnación Castillo[1], Diego P. Morales[1], Almudena Rivadeneyra[1], Alfonso Salinas-Castillo[3], Luis Parrilla[1], Antonio García[1]

1 – Department of Electronics and Computer Technology, Faculty of Science, University of Granada 18071 Granada, Spain

2 – Eesy-Innovation Spain S.L., 18014 Granada, Spain

3 – Department of Analytical Chemistry, Faculty of Science, University of Granada, 18071, Granada, Spain

Published in Measurements 2022, vol. 201, art. 111744

- Received: 17 May 2022; Accepted: 7 August 2022; Published: 11 August 2022
- DOI: 10.1016/j.measurement.2022.111744
- Impact factor: 5.131
- JCR Rank: 17/92, category "Engineering, Multidisciplinary" (Q1, 2021)

A versatile wearable based on reconfigurable hardware for biomedical measurments

Abstract: In this work a versatile hardware platform based on reconfigurable devices is presented. This platform it intended for the acquisition of multiple biosignals, only requiring a reconfiguration to switch applications. This prototype has been combined with graphene-based, flexible electrodes to cover the application to different biosignals presented in this paper, which are electrocardiogram, electrooculogram and electromyogram. The features of this system provide to the user and to medical personnel a complete set of diagnosis tools, available both at home and hospitals, to be used as a triage tool and for remote patient monitoring. Additionally, an Android application has been developed for signal processing and data presentation to the user. The results obtained demonstrate the wide range of possibilities in portable/wearable applications of the combination of reconfigurable devices and flexible electronics, especially for the remote monitoring of patients using multiple biosignals of interest. The versatility of this device makes it a complete set of monitoring tools integrated in a reduced size device.

8.1 Introduction

Wearable devices have entered in our lives as usual, daily-life complements. The use of smartwatches and wristbands is now almost universal in monitoring activity and sports. However, medical applications are not yet fully supported by these devices. Continuous monitoring, which is the usual aim of wearable devices, is of special interest for chronic conditions such as diabetes or coronary diseases. This continuous monitoring has been usually carried out in hospital facilities or with relatively complex devices like Holter monitor, which can have a considerable impact on the daily life of the user. Furthermore, these devices do not usually provide remote connection or communication with the medical professional requesting the data, so the acquired data have to be processed off-line, after acquisition.

The use of medical wearables is an useful tool to confront the challenge of remote healthcare [1]. This can be useful in many scenarios, ranging from healthcare in spaces with restricted or difficult access, to avoiding saturation of healthcare systems due to ageing population [2, 3]. The former will be one of the main challenges for healthcare systems in the future, with an expected noticeable increase of healthcare needs that can be mitigated with remote healthcare technologies [4]. Thanks to the use of wearables, it is possible to displace patient monitoring, or even some treatments, from hospital infrastructures to home environments [5, 6, 7]. Home monitoring can also be used either as a triage tool or as preventive diagnosis to determine whether the user requires further treatments and diagnosis tests in a hospital or can be treated at home. To do so, it is needed to have multiple devices available for the different signals required by the medical personnel. The most common biosignals are electrocardiogram (ECG) and electroencephalogram (EEG), but this last one needs of complex devices and controlled conditions for acquisition. Other typical signals are electromyogram (EMG) and electrooculography (EOG). ECG is essential for the detection of cardiovascular conditions such as heart attacks or heart murmurs, which are some of the most common diseases. EMG is used to diagnose motor diseases like muscular dystrophia or myositis, or to monitor chronic motor diseases. EOG is less used than the other two signals and it allows to diagnose retinal abnormalities and attention deficit disorders [8].

Many portable devices for wearable acquisition can be found in the literature, such as ECG [9, 10, 11, 12, 13], EMG [14, 15, 16] or EEG sensors [17, 18]. EOG is a less common application, but still recent works have focused on this topic, as the one proposed by Debbarma *et al.* [19]. However, this kind of systems is designed to acquire only one type of signal or for a concrete application. Several authors have recently worked on the acquisition of multiple signals within a single device, which for many of these works is based on an Application-Specific Integrated Circuit (ASIC) with multiple inputs [20, 21, 22]. Other approximation is to use çASICs that provide a reconfigurable front-end rather than multiple inputs, thus allowing to change that front-end and to apply that hardware to different applications [23, 24, 25]. Even if this approximation could be adapted to different scenarios, it is still composed of dedicated hardware that cannot be easily modified.

The development of flexible electronics paves the way for new wearable devices that can be better integrated into the daily life of the user [26, 27]. Flexible devices are usually based on printed technologies, novel 2D materials, or the combination of these two technologies [28]. The most typical printing technologies are screen and ink-jet printing, along with spray coating [29, 30]. For example, ink-jet can be used on textiles to create e-textiles [31], or can be used on flexible substrates to create electrodes for biosignals [32]. These techniques are not limited to electrodes, as they can be also used for temperature or chemical sensors [33, 34, 35].

The expansion of 2D materials includes their application to devices for chemical sensing or biosignal acquisition. For example, Soganci *et al.* developed a reduced graphene oxide (rGO) glucose sensor [36]. Also, electrodes can be made of graphene, as those developed by Karim *et al.* [31], Lou *et al.* [37] or Golparvar *et al.* [38] that integrate graphene in textile elements. Laser Induced Graphene (LIG) is also a cost-effective technique to obtain this type of electrodes [32, 39, 40]. These electrodes have several advantages over the traditional ones, as they are dry and can avoid allergic problems related to pastes used in current alternatives [41, 42, 43]. Also polymers are available for these purposes, typically Poli(3,4- Ethylenedioxythiophene)-Poli(Styrene Sulfonate) (PEDOT) is used alone or in combination with carbon derived materials [44, 45, 46].

In this work, we combine the advantages of flexible electronics with analog and digital reconfigurable devices to create a versatile hardware platform able to acquire multiple types of signals, only requiring a reconfiguration to switch applications. This is possible thanks to the reconfiguration capabilities of the presented platform. Combining this feature with flexible electronics makes possible to adapt wearables to different parts of the body, or even integrate them into the user clothing. The device proposed in this paper is able to measure biosignals such as electrocardiogram, electromyogram or electrooculogram with the hardware included in the board and also perform chemical analysis using extension boards and the reconfigurability features of the device . These features provide a complete set of diagnosis tools to the user and to medical personnel, available either at home, to be used as a triage tool, or for remote patient monitoring. Besides, this approach has also several advantages in terms of sustainability. The use of only one device for different purposes allows to reduce electronic waste, reusing the device for different applications [47]. An overview of the system is shown in Figure 8.1.

The rest of the manuscript is structured in five sections. section 8.2 is devoted to the description of the system and the details of its design. section 8.3 details some of the methods used in this work, such as signal acquisition or the definition of some performance parameters. section 8.4 illustrates the results obtained from the developed prototype. A comparison to other alternatives in the literature is presented in section 8.5. Finally, section 8.6 summarizes the conclusions derived from this work.

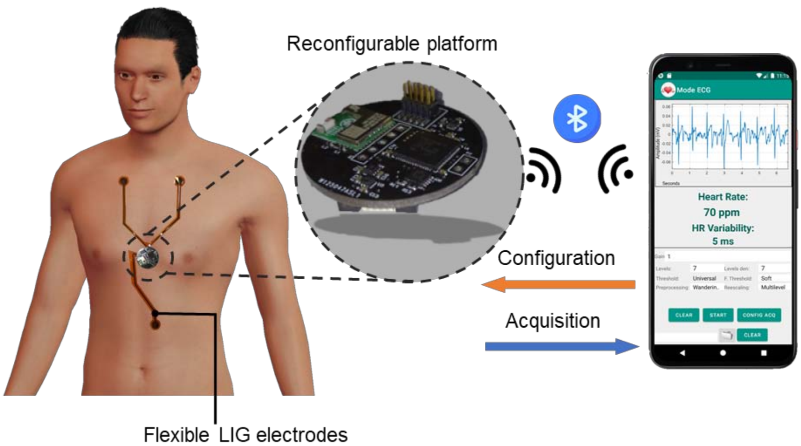

Figure 8.1: Conceptual view of the presented system.

8.2 System Design

8.2.1 Acquisition system

The developed system is based on reconfigurable devices with analog and digital reconfiguration capabilities, which allow to adapt the acquisition parameters to different biosignals. A schematic overview of the developed system is shown in Figure 8.1. The system is based on a Programable System on Chip (PSoC), specifically the PSoC 5LP from Cypress Semiconductors [48]. This unit oversees the interconnection of all the different subsystems thanks to its inherent reconfigurability. The PSoC5 LP also manages communications with external devices through SPI or UART connections. Finally, the

Bluetooth connection of the device is controlled by a PSoC4 BLE, also from Cypress Semiconductors [49], which manages the BLE services and communicates data to the central unit. This communication device can be also used to manage auxiliary tasks such as battery monitoring. All connectors referenced in Figure 8.2 are flexible, thus allowing to connect either external boards, such as expansion boards, or flexible electrodes or sensors directly linked to the system. These connectors have 4 terminals each one: two of them are power connectors (VCC and GND) and the other two are signal pins. Thanks to this configuration it is possible to connect up to 6 analog signals and 2 digital signals, while 4 power connectors are available in case they are required by any sensor.

The system is also equipped with an INA 333 (from Texas Instruments [50]) differential amplifier directly connected to the PSoC5 LP. Thanks to the reconfigurability of the PSoC 5LP, the differential amplifier can be connected to any analog input and combined with the analog circuitry available within the PSoC 5LP. This amplifier has a fixed gain of 50 V/V.

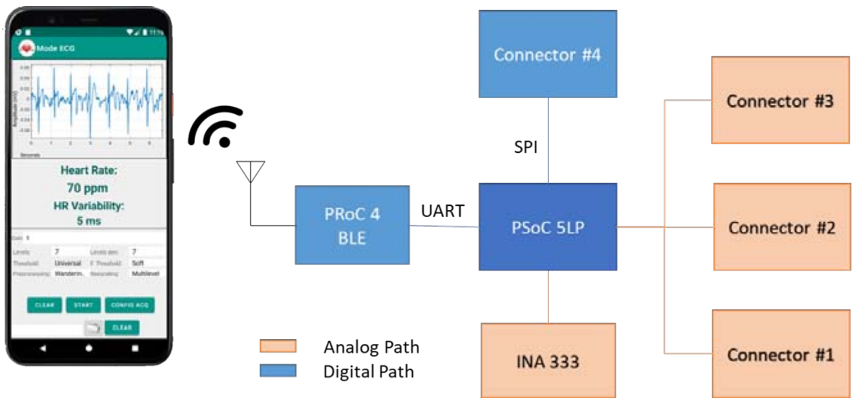

Figure 8.2: Schematic view of the developed prototype.

Thanks to the inherent reconfigurability of the PSoC5 LP, the external components can be connected to a variety of different circuits formed by the internal reconfigurable resources in the PSoC5 LP. In Figure 8.3a, a representation of the configuration for ECG acquisitions is shown, which exemplifies the philosophy of the developed system in which the INA333 amplifier is connected to two of the inputs through a preamplification stage.

Since the system is oriented to wearable use, power consumption is key. Thus, in order to improve this aspect, different regulators have been included in the device, as it is shown in Figure 8.3b. With this, it is possible to power down any external devices not in use. The system can be supplied in the range from 2.0 to 5.5 V, so a wide range of batteries can be used. The system has been tested with a 3.7-V, 350-mAh Li-ion battery that allowed to acquire signals for 16 hours. The final appearance of the prototype is shown in Figure 8.3c, where the main components are highlighted.

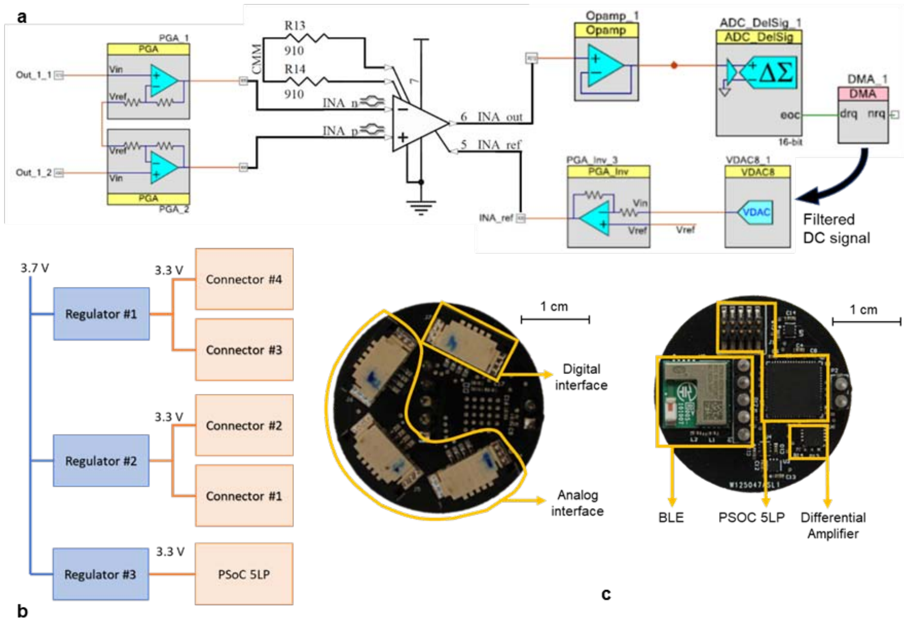

Figure 8.3: Proposed system: (a) Detail on the ECG acquisition configuration. (b) Power subsystem scheme. (c) Final prototype.

The device is mainly oriented to biosignal acquisition; however, its design also makes it possible to broaden its functionalities to other applications. For example, glucose sensing can be also implemented on this device using the technique presented in [51]. This technique needs of a temperature sensor and a small power supply, so the presented device only requires connecting the temperature sensor to the SPI interface and the heater to one of the available power interfaces. The final processing of this chemical sensor is based on a smartphone through colorimetric measurement.

8.2.2 Electrodes

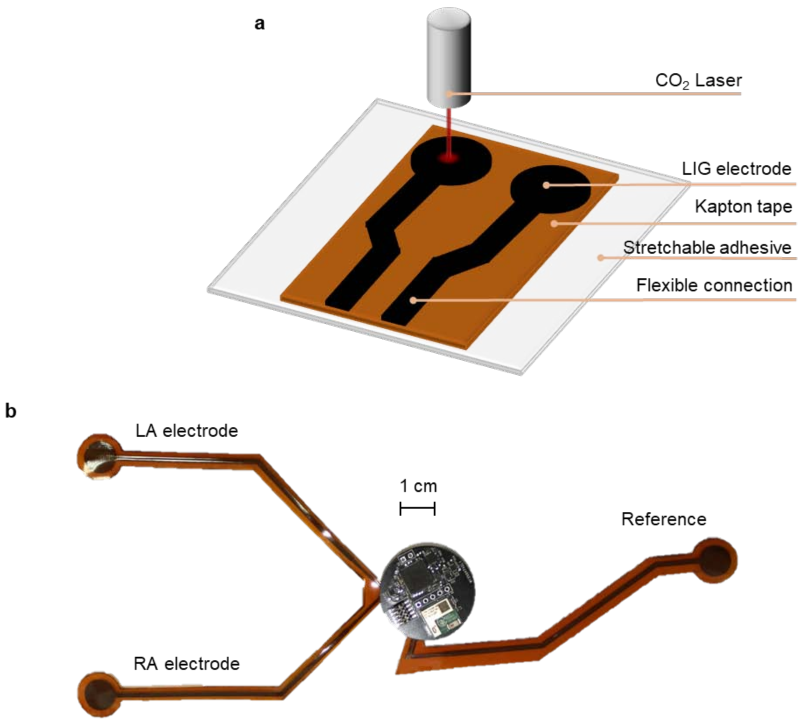

Figure 8.4: (a) LIG fabrication process; (b) Electrodes integrated with the prototype.

The electrodes used in this work are designed with LIG technology, which has been proven to be a cost-efficient option to create flexible electronics [52]. The electrodes are created by laser ablation of Kapton® (Dupont), thus producing the so-called Laser Induced Graphene (LIG). Figure 8.4a schematizes the structure of the electrode and its fabrication process. A 2.4-W CO_2 laser is used for the ablation of a Kapton film of 75 µm and, later, an adhesive patch is added to attach the electrode to the skin. The used electrodes are circular, with 1 cm of diameter, which is a size similar to commercial wet electrodes. The skin was only treated cleaning it with alcohol to eliminate any grease or dirt which could affect the measurement. The connections to the board are also imprinted on LIG, thus creating a patch-like electrode that can be used in a completely wearable system, similar to the one presented in [32]. The final aspect of the prototype and the patch electrodes fabricated to acquire ECG signals are shown in Figure 8.4b. This image is a clear example of how flexible electrodes, and the presented system can be combined. Just changing the flexible patch and the PSoC5 LP configuration, it is possible to adapt the device to other signals such as EOG or EMG as it is described in section 8.3.

8.2.3 Android App

A custom Android application has been developed to both configure the system and manage the acquisition of the different biosignals. The app is in charge of configuring the platform, acquiring the signals and processing them. It is also able to store the acquired data in the mobile device. Figure 8.5 shows some screenshots of the application. This app has been developed for the API level 31 with Android Studio 4.24 and it is compatible down to API level 26.

The preprocessing of signals to suppress noise and interference is based on the Wavelet Transform. To apply this transform to the signals, a high pass filter and low pass filter are applied subsequently to the signal in each of the so-called levels of the transform. The coefficients of the filters depend on the wavelet used for the transform. After the transform, low and high frequency components of the signal are obtained, so it is possible to suppress wandering through the low frequency components and to suppress high-frequency noise over the rest of the signal. As it can be seen in the ECG mode screenshot, the parameters of the signal processing can be changed on the fly to fine tune the algorithm depending on the circumstances of the acquisition. Details on the parameters and the processing can be found in [53]. This method allows to eliminate either wandering or high frequency noise in the case of ECG. For EOG the processing is applied to eliminate high frequency noise. EMG signals are not processed by the app as the filtering applied with the PSoC5 LP is enough for the needs of the subsequent data extraction. Further details on signal processing will be provided in section 8.3 and section 8.4.

8.3 Methods

Figure 8.5: Screenshots of custom Android App.

In this section the acquisition procedures for different biosignals using the presented prototype will be described. Additionally, details on the signal processing implemented for the different biosignals will be provided, and the performance parameters for each experiment will be presented.

8.3.1 Acquisition methods

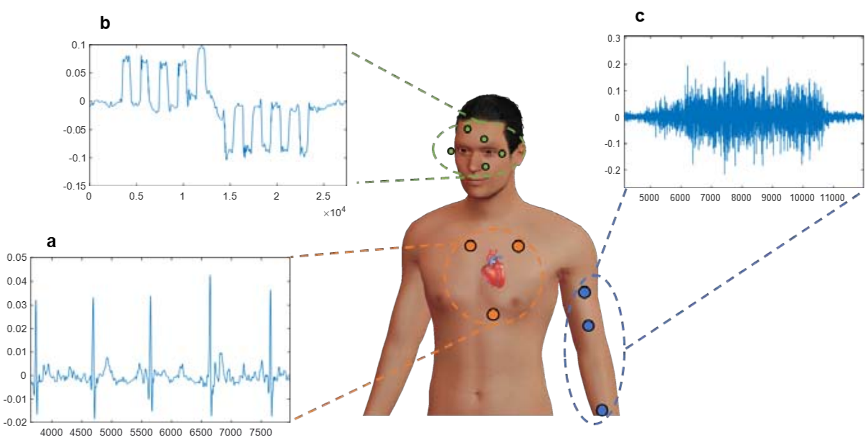

Figure 8.6: Acquisition details: (a) ECG signal and placement of electrodes (orange). (b) EOG and placement of electrodes (green), (c) EMG signal and placement of electrodes (blue).

The acquisition of biosignal is carried out with a differential amplification and a reference electrode for common mode and noise cancellation. In the case of ECG signals, Derivation I is acquired on the chest of the user by two electrodes above the heart and the reference electrode below it. The reference electrode is used to provide a common mode of VDD/2, thus allowing the amplifier full swing at the output and the feedback of noise with an inverter amplifier in order to cancel it. The signal is later digitalized at a sampling rate of 1 kHz and filtered with a pass-band filter in the 1-35 Hz band, which includes the main components of the ECG signal. This filter is implemented in the digital configurable part of PSoC5 LP. Figure 8.6a represents the positioning of electrodes and an example of the signal obtained from these positions and Figure 8.7c shows the actual position of electrodes. With this configuration a set of nine 20-second recordings were acquired from two healthy subjects.

In the case of Electrooculogram (EOG), two channels, vertical and horizontal, are required to track all the eye movements, as illustrated in Figure 8.6b. In Figure 8.7b the patch-like structure for both channels and the reference is shown in real use. In this case, the signals of both channels are multiplexed to be digitalized by the same Analog-to-Digital Converter (ADC), which samples at 2 kHz in order to digitalize each channel at 1 kHz. As detailed above, the reference is used for noise cancellation and common mode adaption. The filtering in this case is low-pass, with a cut-off frequency of 35 Hz, also implemented in the digital configurable subsystem, since the DC component is required to determine when the eye is fixed at any given position. In order to capture the EOG signal, a guide video (see supporting information) has been used to ensure the same movements were always repeated. The experiments to acquire EOG were focused on the acquisition of the two principal types of eye movement, saccadic and smooth pursuit movements. To achieve this, each acquisition was divided in two parts. In the first one, the subject is asked to make saccadic movements with the eyes looking to a point that suddenly changes its position. These movements are repeated five times in each direction. During the second part of the experiment the user is asked to follow a point that is slowly moving from side to side of the window.

Finally, for EMG signals, the acquisition is carried out in a similar way to that of ECG. However, the spectrum of the EMG signal covers the band between 10 and 300 Hz. Thus, the EMG signal is filtered with a pass-band filter between 10 and 500 Hz. This filter is combined with a notch filter at 50 Hz and 10-Hz bandwidth to suppress electrical grid interferences. The positions of the electrodes are represented in Figure 8.6c and shown in real use in Figure 8.7a. The acquisition was done during a maximum voluntary isometric contraction (MVIC) test of the brachial bicep. The subject was asked to push, applying the maximum force, against a fixture blocking the arm movement. As it will be detailed in subsection 8.3.2, a commercial instrument for biosignal acquisition, Biosignalsplux [50], is used as a reference for this experiment, which was repeated twice, one acquiring the EMG signals with the proposed prototype and then with the Biosignalsplux device. In the case of this Biosignalsplux device, commercial wet electrodes by Ambu® were used.

8.3.2 Performance parameters

To analyze the performance of the prototype, several parameters have been defined for each type of biosignal. The parameters are based in the extraction of characteristics of these signals. This way of defining the parameters allows to determine the quality of the acquisition, since a noisy of distorted signal will make more difficult the extraction of any parameters.

In the case of ECG, accuracy in the detection of each heartbeat, also defined as QRS complex for the name of the characteristic's points of each beat, is measured through three parameters, Sensibility, S_e, Positive Diagnosis Value, PDV and Accuracy, A_{cc}, which are defined as: Equation 8.2

$$S_e = \frac{TD}{TD + FN} \tag{8.1}$$

$$PDV = \frac{TD}{TD + FP} \tag{8.2}$$

$$A_{cc} = \frac{TD}{TD + FP + FN} \tag{8.3}$$

where TD are the correctly, or true-, detected peaks, FP are the False Positives, and FN are the False Negatives.

For EOG, the main objective is to determine the direction and amplitude of the movement through the combination of the vertical and horizontal channels, so the error in those directions will be the performance parameter. In this case, the error is defined relative to a deviation of $\pm\frac{\pi}{4}$ from the expected angle of the movement:

$$\varepsilon = \frac{\Theta_{\text{expected}} - \theta_{measured}}{\pi/4} \tag{8.4}$$

Finally, the EMG spectrum is studied obtaining the Mean Frequency (MNF) and Median Frequency (MDF), which have been demonstrated to be useful for analyzing the muscular fatigue during isometric contraction [52, 54]. Since in this case it is difficult to determine the correct MNF or MDF of an acquisition, the signals obtained with the proposed instrument will be compared to the obtained with the commercially available Biosignalsplux device, which is specifically designed for biosignal acquisition. Thus, the frequencies obtained with this instrument will be considered as the reference ones and the error in the frequencies obtained from the instrument presented in this work, MDF, will be determined as:

$$\varepsilon = \frac{MDF - MDF_{commercial}}{MDF_{commercial}} \tag{8.5}$$

where $MDF_{commercial}$ is the MDF value obtained from the Biosignalsplux device. The same expression for error is considered for the MNF.

Figure 8.7: Position of electrodes in real case uses. (a) EMG acquisition. (b) EOG acquisition. (c) ECG acquisition.

8.4 Results

The results obtained with the presented prototype are illustrated in this section. All the signals have been acquired with the prototype, which transmits the signals in blocks of 5 seconds through BLE to the mobile device. After this transmission, the mobile device processes the signals, which are shown to the user along with the results of the processing.

8.4.1 Electrocardiogram acquisition

The acquisition of ECG signals was done in segments of 20 seconds and then processed first using wavelet filtering [53] and, subsequently, applying

Table 8.1: Characteristics of the mean QRS peaks and time segments for the averaged QRS.

Peak	Amplitude (mV)	Standard deviation (mV)	Segment	Length(s)	Standard deviation (s)
P	0.0097	0.0075	**RR**	0.9466	0.0758
Q	-0.0145	0.0140	**PQ**	0.1208	0.0441
R	0.0638	0.0193	**QR**	0.0354	0.0185
S	-0.0376	0.0217	**RS**	0.0255	0.0038
T	0.0182	0.0065	**ST**	0.1927	0.0501

a threshold algorithm to detect the R peaks corresponding to each beat. After that, local minima before and after each R peak are searched for, in order to detect Q and S peaks. Finally, P and T peaks are found by searching for local maxima before Q peaks and after S peaks, respectively. In Figure 8.8a, a 10-second segment of one of the acquired ECG signals is shown, including the markers for the PQRST peaks of each beat. As it can be observed, it is possible to detect the characteristic points with a good accuracy for all of Q, R and S points. P and T peaks are more difficult to find, presenting thus higher failure rate in their detection.

Analyzing an averaged QRS-complex, it is possible to more clearly observe the amplitude and timing of each peak, as most of the random noise will be canceled. Figure 8.8b displays the mean QRS-complex obtained from a 20-second recording, which has been obtained after superimposing all detected complexes placing the R-peaks at the reference of the averaged QRS. Using this averaged QRS, the peaks' amplitudes and the duration of the different time segments can be studied. Results in Table 8.1, obtained from the average QRS in Figure 8.8b, show that while Q, R, S and T peaks are clearly appreciable, the P signal presents reduced amplitude and it is hard to distinguish from the noise. Regarding the time segments, the variation is low except for the QR segment, which presents a higher deviation. This can be explained by the low amplitude of the Q peak, which leads to lower precision in its detection along with the typical short duration of this segment, so a small error in the Q-peak determination can be translated into a large error in the segment determination.

To study FNs and FPs of the obtained ECG records, QRS complexes were manually annotated and the resulting positions compared to those detected with the processing detailed above. As detailed in subsection 8.3.11, the ECG acquisition was carried out with two healthy subjects and 20-second acquisitions for each one. The statistics, shown in Table 8.2, were

Table 8.2: Performance parameters for ECG signals.

Record	***FN***	***FP***	***TD***	A_{CC}	***PDV***	S_e
ECG_1	1	1	19	90.48%	95.00%	95.00%
ECG_2	1	2	18	85.71%	90.00%	94.74%
ECG_3	2	4	17	73.91%	80.95%	89.47%
ECG_4	1	3	17	80.95%	85.00%	94.44%
ECG_5	1	1	19	90.48%	95.00%	95.00%
ECG_6	3	1	18	81.82%	94.74%	85.71%
ECG_7	1	1	20	90.91%	95.24%	95.24%
ECG_8	1	1	18	90.00%	94.74%	94.74%
ECG_9	1	6	10	58.82%	62.50%	90.91%
		TOTAL	**168**	**82.56%**	**88.13%**	**92.81%**

obtained using equations Equation 8.1 to Equation 8.2. In general, the system presents an accuracy over 80% along with a similar PDV, while S_e is higher and over 90%. Thus, the system detects more false positives than false negatives. This behavior is the usual for threshold detection algorithms in the case of low amplitude signals, since noise can easily be over the threshold. The use of more complex algorithms, such as PCA or clustering methods [55], could improve these results.

8.4.2 Electrooculogram acquisition

The proposed instrument was also used for EOG acquisition. For this application, two experiments were carried out in order to study the saccadic and pursuit movements while the electrodes were positioned as shown in Figure 8.6. An example of the signal obtained from the saccadic movement experiment is shown in Figure 8.9. The amplitude in the horizontal channel approximately doubles the vertical channel's since, while the vertical channel captures only one eye, the horizontal captures both. This circumstance has been taken into account when processing the signals.

With these EOG acquisitions, the amplitude of the five movements in each direction has been averaged to estimate the direction and amplitude of movement. In Figure 8.10, a vectorial representation of the amplitudes shows the direction and amplitude of movement. The vectors are composed using the amplitudes of each channel (vertical and horizontal) as components of this vector and after normalization to the maximum of them.

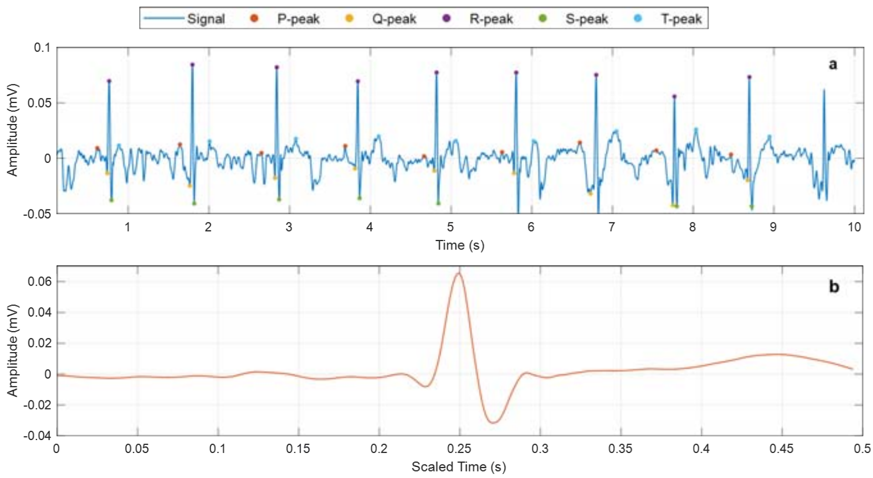

Figure 8.8: ECG acquisition. (a) Segment of an ECG signal acquired. (b) Mean QRS complex.

With this, it is possible to calculate the error in the determination of direction, as it was detailed in subsection 8.3.2. The results obtained for the precision in the determination of the movement direction are shown in Table 8.3. As it can be observed, the precision is over 90% in all the cases. The lower precision is obtained for the “look up” movement, which is affected by a blink movement that can be observed in Figure 8.9, in the vertical channel. Furthermore, for this movement, the noise amplitude in the horizontal axis is comparable to the signal amplitude of the vertical axis, so this can be confused as actual movements of the eye.

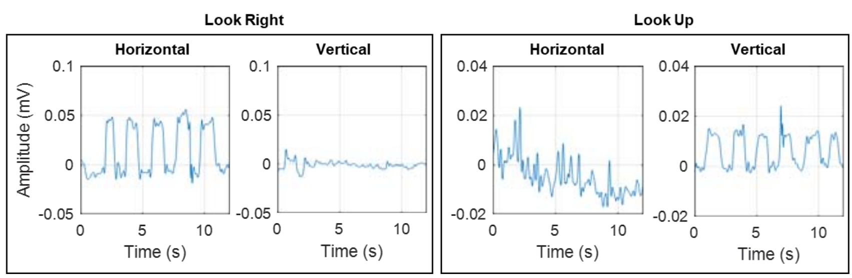

Figure 8.9: EOG signals obtained for the Look Right and Look Up movements.

Table 8.3: Precision in the determination of the direction of the movement.

Look right	Look left	Look down	Look up	Mean	Σ
96.7436%	97.2781%	97.3118%	92.9447%	96.0695%	2.0994%

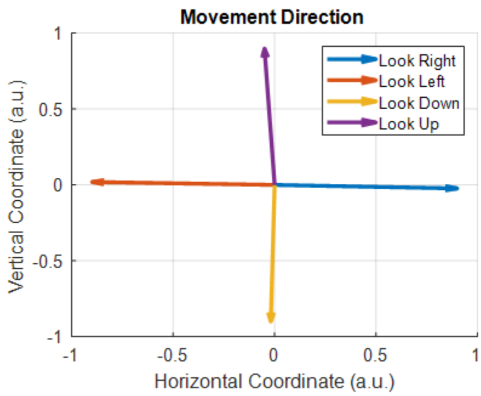

Figure 8.10: Estimation of movements directions from EOG signals.

For the study of pursuit movements, the results for both channels are shown in Figure 8.11a. In this case, the amplitude of the movement is variable in time. In Figure 8.11b, the vectors, obtained as in the case of saccadic movements, are shown over time. Despite the fact these vectors are mainly in the correct direction when the movement is near the peak, there is an appreciable error when the eye is looking ahead (which may be considered as the resting position). In Figure 8.11c the angle of sight and the expected angle are represented over time. As Figure 8.11c shows, despite the angle being close to the expected value, there is a small constant error, which increases as the direction changes. With all this, the mean error obtained in the experiment is 11% with respect to the expected angle.

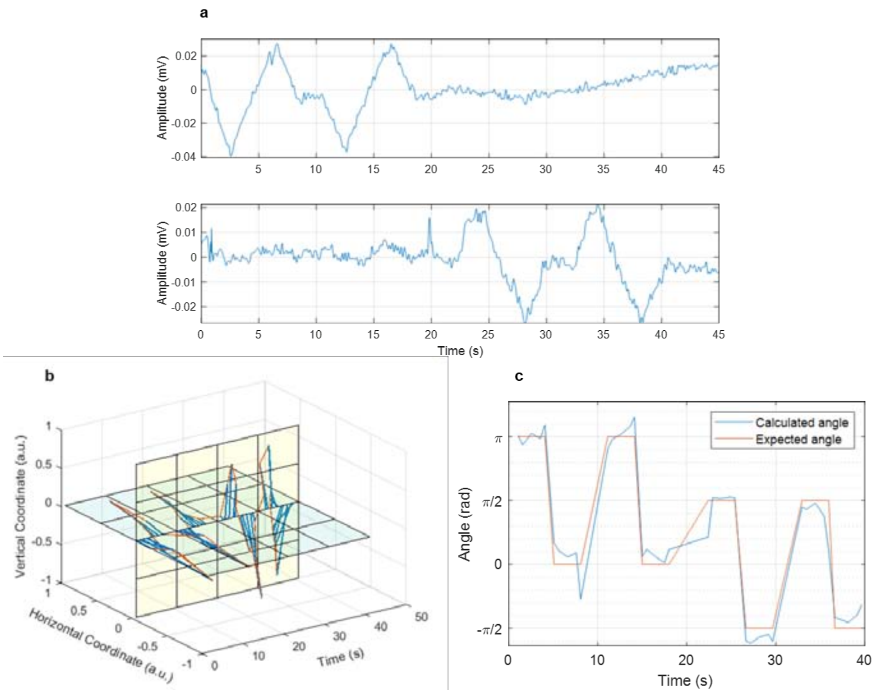

Figure 8.11: (a) Acquisition of pursuit movements in horizontal (up) and vertical channels. (b) Vectorial representation in time. (c) Expected and calculated angles from the acquisition.

8.4.3 Electromyogram acquisition

The third application of the proposed instrument is the acquisition of EMG signals. As described above, EMG acquisition was carried out on the biceps brachii during isometric contraction. The results of this experiment are shown in Figure 8.12a. As the parameter of interest for this type of signal is the frequency spectrum, an example of it is shown in Figure 8.12b. As it can be observed, the main part of this spectrum is between 30 and 70 Hz.

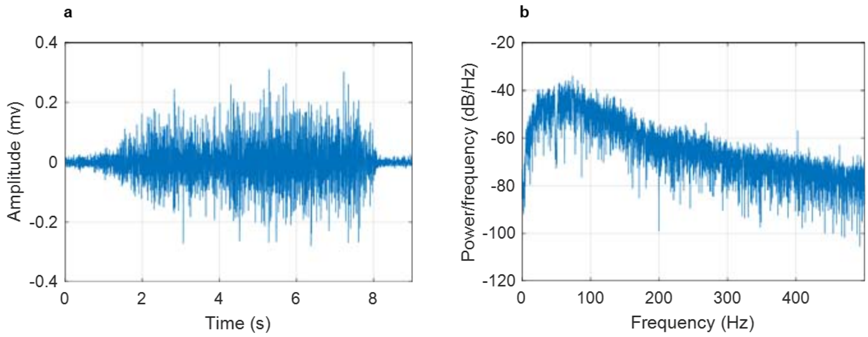

Figure 8.12: EMG acquired. (a) EMG signal of an isometric contraction for 6 s. (b) Spectrum of the obtained signal.

As detailed in subsection 8.3.2, a Biosignalsplux device was used as reference for this experiment. The frequencies obtained from both Biosignalsplux and the presented instrument are shown in Table 8.4. The results obtained with Biosignalsplux show lower median and mean frequencies than those from our prototype. Considering the error as detailed in section 8.2, the presented device has an error of 14% when compared to the results of Biosignalsplux. This discrepancy may be due to differences in the force exerted by the subject. It is also noticeable a difference in the RMS value, which can be due to differences in the contact of the electrodes used for both instruments.

Table 8.4: Results of EMG acquisition.

	MNF (Hz)	MDF (Hz)	RMS (mV)
Prototype instrument	75.24	69.35	0.062
Commercial instrument	65.70	62.44	0.970

8.5 Comparison to other alternatives

Finally, the presented system and the corresponding results have been compared to several works in the literature [16], [19, 20, 21, 22, 23, 24], [35], [46]. Table 8.5 summarizes a qualitative comparison between some recent works and the current proposal. Two main alternatives can be distinguished in the literature: approaches using an ASIC for several signals, and approaches using a flexible system for a single signal. Some works based on ASICs [20, 21, 22, 23, 24], just as this proposal, allow to capture different signals. Unfortunately, they are rigid and, in most cases, do not include the auxiliary hardware needed as power supply or communication subsystems.

Table 8.5: Comparative between recent works and this proposal.

Flexibility	Type of Wearable	Dry/Wet	Interface	Size (mm)	Drawback	Biosignals	Reconfigurability	Ref
No	-	-	Wired	1.7×0.6 (chip die)	ASIC	ECG/BioZ/ PPG/GPA/ GSR	Yes	[24]
Yes	Patch	Dry	Wireless	125×18	Not stretchable	EOG	No	[19]
Partial	Patch	Dry	Wireless	3.3×3.6	Rigid circuitry	EMG	Yes	[16]
No	-	Wet	Wired	2×3 (chip die)	ASIC	PPG/ECG/ RR	No	[22]
No	Wristband	Wet	Wireless	40×23	ASIC	ECG/PPG/ BioZ	No	[21]
No	-	Wet	Wired	1.5×1.7 (chip die)	ASIC	ECG/BioZ/ RR	No	[20]
No	-	Wet	Wired	5×5 (chip die)	ASIC	ECG/PPG	Yes	[23]
Partial	NFC Tag	-	Wired	150×70	Specific Tag for each app	ECG/PPG/ Temp.	No	[35]
Yes	T-Shirt	Dry	Wireless	Ø 30	Not stretchable	ECG	No	[46]
Partial	Patch	Dry	Wireless	Ø 30	Not stretchable	ECG/EMG/ EOG/...	Yes	This work

On the other hand, the approaches based on a device for a specific signal, as those proposed in [19], [46], are completely flexible. However, they can only acquire one type of signal and they cannot change their application. The device we propose in this paper combines the advantages of both approaches, *i.e.*, partial flexibility and the ability to acquire multiple signals. In fact, even if the proposed device has only been tested for ECG, EMG and EOG acquisition, it is able to either acquire other signals or switch applications. As an example, this device can be used for some other biological measurements or in chemical sensing, with minimum extra hardware, thanks to its inherent reconfigurability [51].

8.6 Conclusions

In this paper a new platform intended for the acquisition of biosignals in wearable applications is presented. The proposed prototype makes use of reconfigurable devices to adapt the acquisition interface to different signals, which in combination with flexible low-cost electrodes allow the acquisition of multiple types of signals in a variety of scenarios.

Some of the most common electrical biosignals, such as ECG, EMG and

EOG, have been acquired with the presented prototype and LIG electrodes in order to illustrate its capabilities. The performance of this device was remarkable in all the cases studied. For ECG, the accuracy is over 82% in the detection of QRS complexes even when using the most basic detection algorithms. For EOG, it is possible to determine the direction of the movements with an accuracy over 96%. Finally, in the case of EMG, the results showed an error lower than 15% when compared to a commercial *ad hoc* device. When compared to proposals in the literature, in this work we present a device which combines the advantages of different approaches, thus being able to acquire different signals while using flexible electronics to improve ergonomics.

These results demonstrate the wide range of possibilities in portable/wearable applications of the combination of reconfigurable devices with flexible electronics, especially for the remote monitoring of patients using multiple biosignals of interest. Furthermore, this device is not limited to biosignals and its inherent reconfigurability allows it to switch applications in very different fields, for example in portable chemical sensing as described in subsection 8.2.1. The versatility of this device makes it a complete set of monitoring tools integrated in a reduced size device.

Bibliography

[1] X. Liang, M. Barua, L. Chen, R. Lu, X. Shen, Li, and H. Luo, "Enabling pervasive healthcare through continuous remote health monitoring," *IEEE Wireless Communications*, vol. 19, no. 6, pp. 10–18, 12 2012.

[2] D. P. Morales, E. Castillo, V. Toral-Lopez, A. García, A. Meyer-Baese, A. Tahmassebi, S. Criado, and F. J. Romero, "Wearable biosignal acquisition system for decision aid," in *Smart Biomedical and Physiological Sensor Technology XV*, B. M. Cullum, E. S. McLamore, and D. Kiehl, Eds. SPIE, 5 2018, p. 15, [Online; accessed 2018-05-15]. [Online]. Available: https://www.spiedigitallibrary.org/conference-proceedings-of-spie/10662/2304988/Wearable-biosignal-acquisition-system-for-decision-aid/10.1117/12.2304988.full

[3] P. Lloyd-Sherlock, "Population ageing in developed and developing regions: implications for health policy," *Social Science & Medicine*, vol. 51, no. 6, pp. 887–895, 9 2000.

[4] M. J. Prince, F. Wu, Y. Guo, L. M. Gutierrez Robledo, M. O'Donnell, R. Sullivan, and S. Yusuf, "The burden of disease in older people and implications for health policy and practice," *The Lancet*, vol. 385, no. 9967, pp. 549–562, 2 2015.

[5] J. Navarro, E. Vidaña-Vila, R. Alsina-Pagès, and M. Hervás, "Real-time distributed architecture for remote acoustic elderly monitoring in residential-scale ambient assisted living scenarios," *Sensors*, vol. 18, no. 8, p. 2492, 8 2018.

[6] M. Pham, Y. Mengistu, H. M. Do, and W. Sheng, "Cloud-based smart home environment (coshe) for home healthcare," in *2016 IEEE International Conference on Automation Science and Engineering (CASE)*, 2016 IEEE International Conference on Automation Science and Engineering (CASE). Fort Worth, TX, USA: IEEE, 8 2016, pp. 483–488, [Online; accessed 2021-03-04]. [Online]. Available: http://ieeexplore.ieee.org/document/7743444/

[7] S. Patel, H. Park, P. Bonato, L. Chan, and M. Rodgers, "A review of wearable sensors and systems with application in rehabilitation," *Journal of NeuroEngineering and Rehabilitation*, vol. 9, no. 1, p. 21, 2012.

[8] F. Latifoğlu, M. Y. Esas, and E. Demirci, "Diagnosis of attention-deficit hyperactivity disorder using eog signals: a new approach," *Biomedical Engineering / Biomedizinische Technik*, vol. 65, no. 2, pp. 149–164, 4 2020.

[9] C. Liu, X. Zhang, L. Zhao, F. Liu, X. Chen, Y. Yao, and J. Li, "Signal quality assessment and lightweight qrs detection for wearable ecg smartvest system," *IEEE Internet of Things Journal*, vol. 6, no. 2, pp. 1363–1374, 4 2019.

[10] S. Ramasamy and B. Archana, "Wearable sensors for ecg measurement: a review," *Sensor Review*, vol. 38, no. 4, pp. 412–419, 2018.

[11] V. Toral, A. García, F. Romero, D. Morales, E. Castillo, L. Parrilla, F. Gómez-Campos, A. Morillas, and A. Sánchez, "Wearable system for biosignal acquisition and monitoring based on reconfigurable technologies," *Sensors*, vol. 19, no. 7, p. 1590, 4 2019.

[12] G. Cosoli, S. Spinsante, F. Scardulla, L. D'Acquisto, and L. Scalise, "Wireless ecg and cardiac monitoring systems: State of the art, available commercial devices and useful electronic components," *Measurement*, vol. 177, p. 109243, 6 2021.

[13] F. Patlar Akbulut and A. Akan, "A smart wearable system for short-term cardiovascular risk assessment with emotional dynamics," *Measurement*, vol. 128, pp. 237–246, 11 2018.

[14] A. Gruebler and K. Suzuki, "Design of a wearable device for reading positive expressions from facial emg signals," *IEEE Transactions on Affective Computing*, vol. 5, no. 3, pp. 227–237, 7 2014.

[15] R. Di Giminiani, M. Cardinale, M. Ferrari, and V. Quaresima, "Validation of fabric-based thigh-wearable emg sensors and oximetry for monitoring quadriceps activity during strength and endurance exercises," *Sensors*, vol. 20, no. 17, 2020.

[16] A. Moin, A. Zhou, A. Rahimi, S. Benatti, A. Menon, S. Tamakloe, J. Ting, N. Yamamoto, Y. Khan, F. Burghardt, L. Benini, A. C. Arias, and J. M. Rabaey, "An emg gesture recognition system with flexible high-density sensors and brain-inspired high-dimensional classifier," in *2018 IEEE International Symposium on Circuits and Systems (ISCAS)*, 2018 IEEE International Symposium on Circuits and Systems (ISCAS). Florence: IEEE, 2018, pp. 1–5, [Online; accessed 2021-10-07]. [Online]. Available: https://ieeexplore.ieee.org/document/8351613/

[17] G. Li, B.-L. Lee, and W.-Y. Chung, "Smartwatch-based wearable eeg system for driver drowsiness detection," *IEEE Sensors Journal*, vol. 15, no. 12, pp. 7169–7180, 12 2015.

[18] M. Ha, S. Lim, and H. Ko, "Wearable and flexible sensors for user-interactive health-monitoring devices," *Journal of Materials Chemistry B*, vol. 6, no. 24, pp. 4043–4064, 2018.

[19] S. Debbarma and S. Bhadra, "A lightweight flexible wireless electrooculogram monitoring system with printed gold electrodes," *IEEE Sensors Journal*, vol. 21, no. 18, pp. 20 931–20 942, 9 2021.

[20] J. Xu, P. Harpe, J. Pettine, C. Van Hoof, and R. F. Yazicioglu, "A low power configurable bio-impedance spectroscopy (bis) asic with simultaneous ecg and respiration recording functionality," in *ESSCIRC Conference 2015 - 41st European Solid-State Circuits Conference (ESSCIRC)*, ESSCIRC Conference 2015 - 41st European Solid-State Circuits Conference. Graz, Austria: IEEE, 9 2015, pp. 396–399, [Online; accessed 2022-01-26]. [Online]. Available: http://ieeexplore.ieee.org/document/7313911/

[21] M. Konijnenburg, S. Stanzione, L. Yan, D.-W. Jee, J. Pettine, R. van Wegberg, H. Kim, C. van Liempd, R. Fish, J. Schluessler,

H. de Groot, C. van Hoof, R. F. Yazicioglu, and N. van Helleputte, "28.4 a battery-powered efficient multi-sensor acquisition system with simultaneous ecg, bio-z, gsr, and ppg," in *2016 IEEE International Solid-State Circuits Conference (ISSCC)*, 2016 IEEE International Solid-State Circuits Conference (ISSCC). San Francisco, CA, USA: IEEE, 1 2016, pp. 480–481, [Online; accessed 2022-01-26]. [Online]. Available: http://ieeexplore.ieee.org/document/7418116/

[22] R. Agarwala, P. Wang, and B. H. Calhoun, "A 405nw/4.8μw event-driven multi-modal (v/i/r/c) sensor interface for physiological and environmental co-monitoring," in *2021 IEEE Biomedical Circuits and Systems Conference (BioCAS)*, 2021 IEEE Biomedical Circuits and Systems Conference (BioCAS). Berlin, Germany: IEEE, 10 2021, pp. 1–4, [Online; accessed 2022-01-26]. [Online]. Available: https://ieeexplore.ieee.org/document/9644963/

[23] J. Kim and H. Ko, "Reconfigurable voltage/current readout instrumentation amplifier for cardiovascular health monitoring," in *2018 IEEE International Symposium on Circuits and Systems (ISCAS)*, 2018 IEEE International Symposium on Circuits and Systems (ISCAS). Florence: IEEE, 5 2018, pp. 1–4, [Online; accessed 2022-01-26]. [Online]. Available: https://ieeexplore.ieee.org/document/8350923/

[24] J. Xu, M. Konijnenburg, H. Ha, R. van Wegberg, S. Song, D. Blanco-Almazan, C. Van Hoof, and N. Van Helleputte, "A 36 μw 1.1 mm ^{2} reconfigurable analog front-end for cardiovascular and respiratory signals recording," *IEEE Transactions on Biomedical Circuits and Systems*, vol. 12, no. 4, pp. 774–783, 8 2018.

[25] Y.-J. Huang, T.-H. Tzeng, T.-W. Lin, C.-W. Huang, P.-W. Yen, P.-H. Kuo, C.-T. Lin, and S.-S. Lu, "A self-powered cmos reconfigurable multi-sensor soc for biomedical applications," *IEEE Journal of Solid-State Circuits*, vol. 49, no. 4, pp. 851–866, 4 2014.

[26] W. Gao, H. Ota, D. Kiriya, K. Takei, and A. Javey, "Flexible electronics toward wearable sensing," *Accounts of Chemical Research*, vol. 52, no. 3, pp. 523–533, 3 2019.

[27] Y. Ma, Y. Zhang, S. Cai, Z. Han, X. Liu, F. Wang, Y. Cao, Z. Wang, H. Li, Y. Chen, and X. Feng, "Flexible hybrid electronics for digital healthcare," *Advanced Materials*, vol. 32, no. 15, p. 1902062, 4 2020.

[28] I.-C. Cheng and S. Wagner, "Overview of flexible electronics technology," in *Electronic Materials: Science & Technology*, W. S. Wong and

A. Salleo, Eds. Boston, MA: Springer US, 2009, vol. 11, pp. 1–28, collection-title: Electronic Materials: Science & Technology.

[29] Z. Cui, *Printed electronics: materials, technologies and applications*. Singapore: Wiley, 2016.

[30] S. K. Sinha, Y. Noh, N. Reljin, G. M. Treich, S. Hajeb-Mohammadalipour, Y. Guo, K. H. Chon, and G. A. Sotzing, "Screen-printed pedot:pss electrodes on commercial finished textiles for electrocardiography," *ACS Applied Materials & Interfaces*, vol. 9, no. 43, pp. 37 524–37 528, 11 2017.

[31] N. Karim, S. Afroj, A. Malandraki, S. Butterworth, C. Beach, M. Rigout, K. S. Novoselov, A. J. Casson, and S. G. Yeates, "All inkjet-printed graphene-based conductive patterns for wearable e-textile applications," *Journal of Materials Chemistry C*, vol. 5, no. 44, pp. 11 640–11 648, 2017.

[32] V. Toral, E. Castillo, A. Albretch, F. J. Romero, A. Garcia, N. Rodriguez, P. Lugli, D. P. Morales, and A. Rivadeneyra, "Cost-effective printed electrodes based on emerging materials applied to biosignal acquisition," *IEEE Access*, vol. 8, pp. 127 789–127 800, 2020.

[33] Y.-F. Wang, T. Sekine, Y. Takeda, K. Yokosawa, H. Matsui, D. Kumaki, T. Shiba, T. Nishikawa, and S. Tokito, "Fully printed pedot:pss-based temperature sensor with high humidity stability for wireless healthcare monitoring," *Scientific Reports*, vol. 10, no. 1, p. 2467, 12 2020.

[34] Y. Tang, K. Petropoulos, F. Kurth, H. Gao, D. Migliorelli, O. Guenat, and S. Generelli, "Screen-printed glucose sensors modified with cellulose nanocrystals (cncs) for cell culture monitoring," *Biosensors*, vol. 10, no. 9, p. 125, 9 2020.

[35] M. S. Zaman and B. I. Morshed, "A low-power portable scanner for body-worn wireless resistive analog passive (wrap) sensors for mhealth applications," *Measurement*, vol. 177, p. 109214, 6 2021.

[36] K. Soganci, H. Bingol, and E. Zor, "Simply patterned reduced graphene oxide as an effective biosensor platform for glucose determination," *Journal of Electroanalytical Chemistry*, vol. 880, p. 114801, 1 2021.

[37] C. Lou, R. Li, Z. Li, T. Liang, Z. Wei, M. Run, X. Yan, and X. Liu, "Flexible graphene electrodes for prolonged dynamic ecg monitoring," *Sensors*, vol. 16, no. 11, p. 1833, 11 2016.

[38] A. J. Golparvar and M. K. Yapici, "Electrooculography by wearable graphene textiles," *IEEE Sensors Journal*, vol. 18, no. 21, pp. 8971–8978, 11 2018.

[39] B. Sun, R. N. McCay, S. Goswami, Y. Xu, C. Zhang, Y. Ling, J. Lin, and Z. Yan, "Gas-permeable, multifunctional on-skin electronics based on laser-induced porous graphene and sugar-templated elastomer sponges," *Advanced Materials*, vol. 30, no. 50, p. 1804327, oct 2018.

[40] F. J. Romero, E. Castillo, A. Rivadeneyra, A. Toral-Lopez, M. Becherer, F. G. Ruiz, N. Rodriguez, and D. P. Morales, "Inexpensive and flexible nanographene-based electrodes for ubiquitous electrocardiogram monitoring," *npj Flexible Electronics*, vol. 3, no. 1, p. 12, 6 2019.

[41] R. J. Cochran and T. Rosen, "Contact dermatitis caused by ecg electrode paste:," *Southern Medical Journal*, vol. 73, no. 12, pp. 1667–1668, 12 1980.

[42] Y. M. Chi, T.-P. Jung, and G. Cauwenberghs, "Dry-contact and noncontact biopotential electrodes: Methodological review," *IEEE Reviews in Biomedical Engineering*, vol. 3, pp. 106–119, 2010.

[43] W. Uter and H. J. Schwanitz, "Contact dermatitis from propylene glycol in ecg electrode gel," *Contact Dermatitis*, vol. 34, no. 3, pp. 230–231, 3 1996.

[44] J. Roopa, K. Geetha, and B. Satyanarayana, "Fabrication of polymer based flexible sensors for eog and emg applications," *Materials Today: Proceedings*, p. S2214785321059265, 9 2021.

[45] C.-Y. Huang and C.-W. Chiu, "Facile fabrication of a stretchable and flexible nanofiber carbon film-sensing electrode by electrospinning and its application in smart clothing for ecg and emg monitoring," *ACS Applied Electronic Materials*, vol. 3, no. 2, pp. 676–686, 2 2021.

[46] S. Masihi, M. Panahi, D. Maddipatla, A. J. Hanson, S. Fenech, L. Bonek, N. Sapoznik, P. D. Fleming, B. J. Bazuin, and M. Z. Atashbar, "Development of a flexible wireless ecg monitoring device with dry fabric electrodes for wearable applications," *IEEE Sensors Journal*, pp. 1–1, 2021.

[47] V. Toral-López, C. González, F. J. Romero, E. Castillo, L. Parrilla, A. García, N. Rodriguez, A. Rivadeneyra, and D. P. Morales, "Reconfigurable electronics: Addressing the uncontrolled increase of waste electrical and electronic equipment," *Resources, Conservation and Recycling*, vol. 138, pp. 47–48, 11 2018.

[48] C. S. Corporation, *PSoC 5 LP Family Datasheet.* Cypress, 2016. [Online]. Available: http://www.cypress.com/file/45906/download

[49] Cypress, "Cyble-214015-01 ez-ble™ creator module." [Online]. Available: https://www.mouser.es/datasheet/2/100/CYPR_S_A0011803837_1-2541406.pdf

[50] T. Instruments, "Ina333 micro-power (50μa), zerø-drift, rail-to-rail out instrumentation amplifier," 12 2015. [Online]. Available: https://www.ti.com/lit/ds/symlink/ina333.pdf?ts=1651493600551&ref_url=https%253A%252F%252Fwww.google.com%252F

[51] I. Ortiz-Gómez, V. Toral-López, F. J. Romero, I. de Orbe-Payá, A. García, N. Rodríguez, L. F. Capitán-Vallvey, D. P. Morales, and A. Salinas-Castillo, "In situ synthesis of fluorescent silicon nanodots for determination of total carbohydrates in a paper microfluidic device combined with laser prepared graphene heater," *Sensors and Actuators B: Chemical*, vol. 332, p. 129506, apr 2021.

[52] D. Meldrum, E. Cahalane, R. Conroy, D. Fitzgerald, and O. Hardiman, "Maximum voluntary isometric contraction: Reference values and clinical application," *Amyotrophic Lateral Sclerosis*, vol. 8, no. 1, pp. 47–55, 1 2007.

[53] E. Castillo, D. P. Morales, A. García, Martínez-Martí, L. Parrilla, and A. J. Palma, "Noise suppression in ecg signals through efficient one-step wavelet processing techniques," *Journal of Applied Mathematics*, vol. 2013, p. e763903, 6 2013.

[54] L. Qi, J. M. Wakeling, A. Green, K. Lambrecht, and M. Ferguson-Pell, "Spectral properties of electromyographic and mechanomyographic signals during isometric ramp and step contractions in biceps brachii," *Journal of Electromyography and Kinesiology*, vol. 21, no. 1, pp. 128–135, 2 2011.

[55] E. Castillo, D. P. Morales, A. García, L. Parrilla, V. U. Ruiz, and J. A. Álvarez Bermejo, "A clustering-based method for single-channel fetal heart rate monitoring," *PLOS ONE*, vol. 13, no. 6, p. e0199308, 6 2018.

Chapter 9

Readout Portable System For Wireless Chipless Biosensing

Víctor Toral[1], José F. Salmerón[1], Diego P. Morales[1], Noel Rodríguez[1], Encarnación Castillo[1], Almudena Rivadeneyra[1]

1 – Department of Electronics and Computer Technology, Faculty of Science, University of Granada 18071 Granada, Spain

Published in IEEE RFID-TA 2021, pp. 1-4

- Date of Conference: 06-08 October 2021
- DOI: 10.1109/RFID-TA53372.2021.9617303
- Location : Delhi, India

Readout Portable System For Wireless Chipless Biosensing

Abstract: In this letter, we present the extension of a previous work on a cost-effective method for fabricating highly sensitive humidity sensors on flexible substrates with a reversible response, allowing precise monitoring of the humidity threshold. In that work we demonstrated the use of three-dimensional Metal-Organic Framework (MOF) film deposition based on the perylene-3,4,9,10-tetracarboxylate linker, potassium as metallic center and the inter-spacing of silver interdigitated electrodes (IDEs) as humidity sensors. In this work, we study one of the most important issues in efficient and reproducible mass production, which is to optimize the most important processes' parameters in their fabrication, such as controlling the thickness of the sensor's layers. We demonstrate this method not only allows for the creation of humidity sensors, but it also is possible to change the humidity value that changes the actuator state.

Keywords: RFID, LC circuit, biosignals, instrumentation

9.1 Introduction

Future management of healthcare systems need of innovative solution to avoid saturation of it due to the aging of the population [1, 2]. This aging will also require an increase in cares of the patients. Translating the Point Of Care (POC) to households will allow to improve the service offered to patients and an important point to avoid the saturation of the healthcare system which is the early detection of illnesses [3, 4, 5, 6, 7].

In this context, the monitorization of patients in home environment is clue. The acquisition of biosignals in this environment is relatively easy and widely studied in the literature [8, 9, 10]. However, there is a point, which is still a great challenge that is the analysis of substances in the body like, for example glucose, lactate, or cholesterol. This type of measurement usually implies the extraction of blood to measure them, which in home can be difficult.

To solve this challenge there are several solutions in the literature like measurement of substances in sweat, saliva or urine in small instruments which act like portable laboratories [11, 12]. In this work, we attempt to pave the way towards new sensors directly integrated in the body using RFID technology. Small RFID tags based in LC tanks can be easily integrated in different parts of the body [13]. For example, a patch in the skin or a dental prosthesis can be used as base for a LC tag whose capacitance or inductance are dependent on a chemical substance. The reading is based in a RFID reader, which is able to detect the changes in the resonant frequency of the tag. In this paper, a device to detect the resonant frequency and transmit the measurement through Bluetooth is presented.

9.2 Materials and Methods

9.2.1 Colpitts Oscillator

The system is based in a Colpitts oscillator whose tank inductor is a PCB printed antenna. The antenna is a 2.5 µH antenna with a size of 25x25 mm. The oscillator is a common emitter oscillator based in the MMBT3904 (Farchild Semiconductors). With the structure described in Figure 9.1, the resonant tank is composed by the inductance of the antenna, the capacitors C2 and C6. With this configuration the resonant frequency, then, will be:

$$C_{tank} = \frac{C2 \cdot C6}{C2 + C6} \tag{9.1}$$

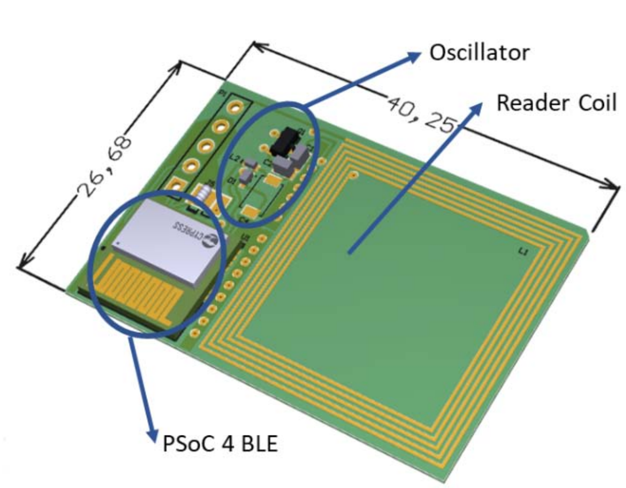

Figure 9.1: Oscillator schematic together with the control scheme used.

To measure the resonance of the tag, is needed to sweep along different frequencies of the oscillator. To do so, a varicap SMV1213-004LF is used in parallel with the tank in such a way that the resonant capacitance then is:

$$C_{tank} = \frac{C2 \cdot C6}{C2 + C6} + C_d \tag{9.2}$$

Being C_d the capacitance of the varicap diode. With this configuration the oscillation frequency is determined by C_{tank} and the planar inductance printed in the PCB, L_1. In this way the frequency will be:

$$f_{osc} = \frac{2\pi}{\sqrt{L_1 C_{tank}}} \tag{9.3}$$

Finally, the oscillator has been polarized with a resistor in the emitter. This resistor, beyond stabilizing the polarization permits the measurement of DC power consumption of the oscillator, which as will be explained below will be clue in the measurement of the RFID tag.

9.2.2 RFID tag

For testing purposes, the RFID tag used is a commercial RFID antenna in combination with a capacitor to make a resonant tank coupled with the oscillator. The antenna employed is Molex 146236-0031 (Molex) which is a flexible antenna for 13.56 Mhz. The antenna is a 45x55 mm printed antenna whose inductance is made in two spires.

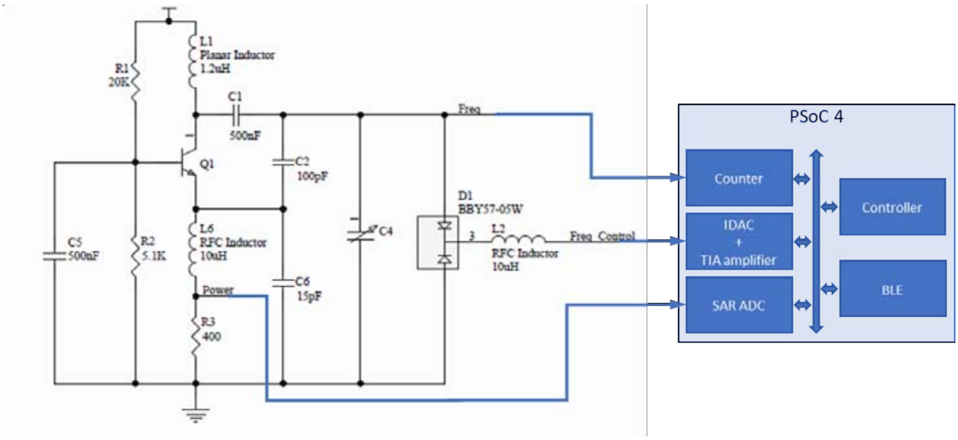

Figure 9.2: Reader prototype. Dimensions in mm.

The inductance measured was 2.5 μH. This antenna was combined with different capacitors to obtain several resonant frequencies for testing of the reading circuit. No matching network has been employed, just a capacitor to generate a resonant LC net.

9.2.3 Measurement method

To measure the resonance, the power consumption of the oscillator is used as an indirect measure. As demonstrated in [14], when the oscillator and the tag are in resonance, the consumption of the oscillator increases. Measuring the voltage through resistor R_E is possible to extract the DC current consumption of the oscillator. Then, to measure the resonance, the oscillator frequency is swept from 11 MHz to 14.5 MHz while the current consumption is measured at each step. Subsequently, the frequency of the peak power consumption is obtained being it the resonant frequency of the tag.

To be able to measure the frequency and the power consumption, a buffer is employed at the output and another one to measure the emitter resistor voltage.

9.2.4 Control and measuring system

The control and measuring system is based in a PSoC 4 BLE, which permits, apart from the control of the oscillator, a Bluetooth connection with a mobile system.

To control the frequency, the current Digital-Analog Converter (DAC) of

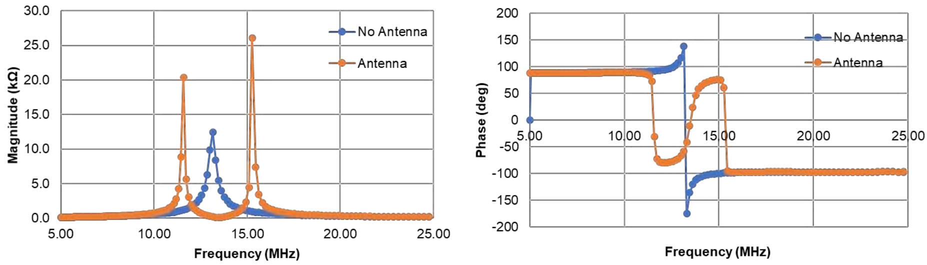

Figure 9.3: Impedance module and phase at the oscillator output with and without the test antenna coupled.

the PSoC with a small current-voltage amplifier is employed, with a range between 0 and 4 V. This voltage range in combination with the varactor response permit a variation in capacitance from 4 pF to 25pF.

The frequency measurement is done with using a 16 bits counter module whose count input is connected to the buffer at the oscillator output. The counter is synchronized with a timer that generates a measuring window of 4 ms.

Power consumption is measured in R_E using SAR ADC with a sampling frequency of 60 ksps. In Figure 9.2 an image of the prototype developed is shown.

9.3 Results and Discussions

As explained above, to test the reader a commercial antenna and a capacitor is employed to simulate the RFID tag. To study the behavior of the system an E4990A impedance analyzer (Keysight Technologies) was employed to measure the impedance at the output of the oscillator while working.

In Figure 9.3, the results of these measurements are shown. In this figure, the impedance at the output of the oscillator when C_d is 18.5 pF is represented in two situations, when the test antenna is coupled and when it is not coupled. As can be seen, when there is not any antenna, there is a single peak at the resonance frequency of 13.2 MHz. When placing the antenna, it is expected to have a peak resonance at lower frequency. However, in presence of the antenna the double peak characteristic of antiresonance appears.

When C_d is much higher or lower than the previous value, the second peak of antiresonance effect is much lower. For example, in Figure 9.4 the

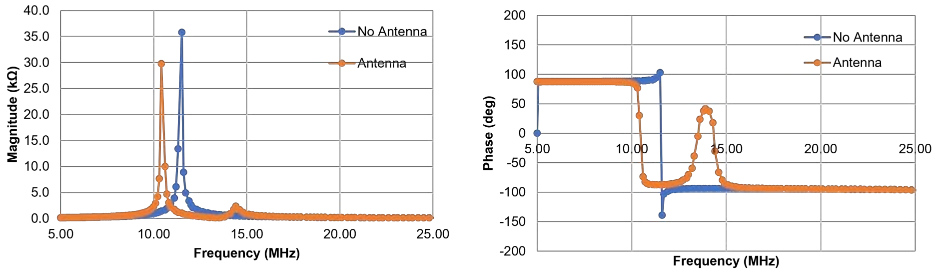

Figure 9.4: Impedance module and phase at the oscillator output with and without the test antenna coupled and 32 pF at the output.

results for $C_d = 32\ pF$ are shown.

As can be seen, when the antenna is coupled, the second peak is much lower and the antiresonance almost disappears, being the dominant peak close to the oscillator resonance frequency.

This effect of antiresonance is probably due to a mismatch in the impedances when oscillator and tag are close to resonance, which probably can be solved with an antenna made ad-hoc for the application. This antiresonance effect limits the precision of the reader as the output of the oscillator is not a single sine so the power of it will not depend directly on when the resonance is achieved.

9.4 Conclusions

In this paper, a RFID tag reader for biomedical applications is shown. The reader is based in PSoC system which allows to transmit the results through Bluetooth. The preliminary results show that while the reader oscillator is able to excite the tag correctly. However, the antiresonance effect which appears when the antenna is coupled with the oscillator, difficult the measurement of the prototype developed.

Bibliography

[1] M. J. Prince, F. Wu, Y. Guo, L. M. Gutierrez Robledo, M. O'Donnell, R. Sullivan, and S. Yusuf, "The burden of disease in older people and implications for health policy and practice," *The Lancet*, vol. 385, no. 9967, pp. 549–562, 2 2015.

[2] P. Lloyd-Sherlock, "Population ageing in developed and developing regions: implications for health policy," *Social Science & Medicine*, vol. 51, no. 6, pp. 887–895, 9 2000.

[3] X. Liang, M. Barua, L. Chen, R. Lu, X. Shen, X. Li, and H. Luo, "Enabling pervasive healthcare through continuous remote health monitoring," *IEEE Wireless Communications*, vol. 19, no. 6, pp. 10–18, 12 2012.

[4] J. Navarro, E. Vidaña-Vila, R. Alsina-Pagès, and M. Hervás, "Real-time distributed architecture for remote acoustic elderly monitoring in residential-scale ambient assisted living scenarios," *Sensors*, vol. 18, no. 8, p. 2492, 8 2018.

[5] M. Pham, Y. Mengistu, H. M. Do, and W. Sheng, "Cloud-based smart home environment (coshe) for home healthcare," 2016 IEEE International Conference on Automation Science and Engineering (CASE). Fort Worth, TX, USA: IEEE, 8 2016, pp. 483–488, [Online; accessed 2021-03-04]. [Online]. Available: http://ieeexplore.ieee.org/document/7743444/

[6] C. Fernandez-Llatas, A. Martinez-Romero, A. Bianchi, J. Henriques, P. Carvalho, and V. Traver, "Challenges in personalized systems for personal health care," 2016 IEEE-EMBS 3rd International Conference on Biomedical and Health Informatics (BHI). Las Vegas, NV: IEEE, 2 2016, pp. 356–359, [Online; accessed 2021-07-08]. [Online]. Available: http://ieeexplore.ieee.org/document/7455908/

[7] S. Patel, H. Park, P. Bonato, L. Chan, and M. Rodgers, "A review of wearable sensors and systems with application in rehabilitation," *Journal of NeuroEngineering and Rehabilitation*, vol. 9, no. 1, p. 21, 2012.

[8] U. Meyer-Baese, H. Muddu, S. Schinhaerl, M. Kumm, and P. Zipf, "Real-time fetal ecg system design using embedded microprocessors," L. Dai, Y. Zheng, H. Chu, and A. D. Meyer-Bäse, Eds. Baltimore, Maryland, United States: SPIE Commercial + Scientific Sensing and Imaging, 5 2016, p. 987106, [Online; accessed 2019-03-06]. [Online]. Available: http://proceedings.spiedigitallibrary.org/proceeding.aspx?doi=10.1117/12.2224256

[9] S. Shustak, L. Inzelberg, S. Steinberg, D. Rand, M. David Pur, I. Hillel, S. Katzav, F. Fahoum, M. De Vos, A. Mirelman, and Y. Hanein, "Home monitoring of sleep with a temporary-tattoo eeg, eog and emg electrode

array: a feasibility study," *Journal of Neural Engineering*, vol. 16, no. 2, p. 026024, 4 2019.

[10] J. Arnin, D. Anopas, M. Horapong, P. Triponyuwasi, T. Yamsa-ard, S. Iampetch, and Y. Wongsawat, "Wireless-based portable eeg-eog monitoring for real time drowsiness detection." IEEE, 7 2013.

[11] I. Ortiz-Gómez, A. Salinas-Castillo, A. G. García, J. A. Álvarez Bermejo, I. de Orbe-Payá, A. Rodríguez-Diéguez, and L. F. Capitán-Vallvey, "Microfluidic paper-based device for colorimetric determination of glucose based on a metal-organic framework acting as peroxidase mimetic," *Microchimica Acta*, vol. 185, no. 1, 1 2018, [Online; accessed 2019-03-07]. [Online]. Available: http://link.springer.com/10.1007/s00604-017-2575-7

[12] I. Ortiz-Gómez, V. Toral-López, F. J. Romero, I. de Orbe-Payá, A. García, N. Rodríguez, L. F. Capitán-Vallvey, D. P. Morales, and A. Salinas-Castillo, "In situ synthesis of fluorescent silicon nanodots for determination of total carbohydrates in a paper microfluidic device combined with laser prepared graphene heater," *Sensors and Actuators B: Chemical*, vol. 332, p. 129506, 4 2021.

[13] A. Rivadeneyra, A. Albrecht, F. Moreno-Cruz, D. P. Morales, M. Becherer, and J. F. Salmeron, "Screen printed security-button for radio frequency identification tags," *IEEE Access*, vol. 8, pp. 49 224–49 228, 2020.

[14] M. A. Carvajal, P. Escobedo, A. Martinez-Olmos, and A. J. Palma, "Readout circuit with improved sensitivity for contactless lc sensing tags," *IEEE Sensors Journal*, vol. 20, no. 2, pp. 885–891, 1 2020.

Part III

Non-published contributions

Chapter 10

Flexible supercapacitors electrodes

This chapter covers the work developed on energy harvesting systems carried out during the stay at the Materials Engineering Department at KU Leuven (Leuven, Belgium). This work consisted of the development of flexible electrodes for supercapacitors using novel materials such as MXenes and LIG were developed.

10.1 MXenes

MXenes are two-dimensional inorganic materials consisting of transition metal carbides, nitrides or carbonitrides with a general formula of $M_{n+1}X_nT_x$, where M is a transition metal, X is carbon or nitrogen and T_x represent the oxygen, fluorine or hydroxyl derived from the synthesis process. MXenes are obtained from MAX phase ceramics, these ceramics having a stechiometry of $M_{n+1}AX_n$, where M is a transition metal, A is an A-group element and X is Carbon or Nitrogen. Typical MAX phases are Ti_3AlC_2, Zr_2AlC, Ti_2SiC [1].

Several routes for the synthesis of MXenes are possible, all of them using the same steps but different reactives, as it is illustrated in Figure 10.1. The first step is the use of a strong acid like HF or HCl in combination with LiF to remove the A-element. After this process, MXenes can be exfoliated through sonication or mechanical agitation, resulting on flakes of multilayered MXenes. This flakes are composed of MXenes layers stacked by weak Van der Walls bonds. The exfoliation process can be improved by adding intercalants such as Dimethyl sulfoxide (DMSO) or Tetrabutylammonium hydroxide (TBAOH) that weaken Van der Walls bonds between layers.

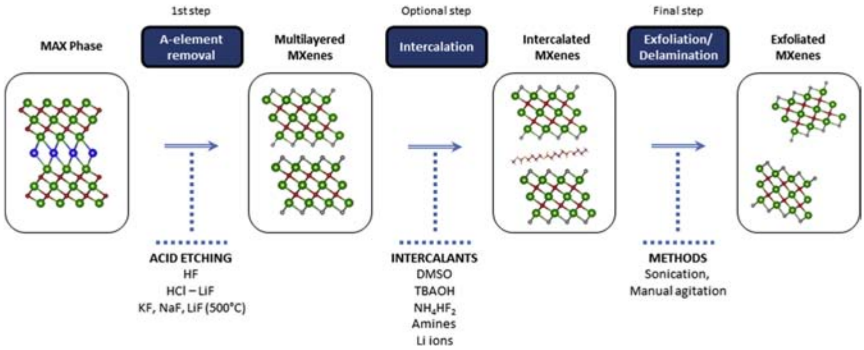

Figure 10.1: Schematic representation of MXenes synthesis procedures[1].

MXenes have unique properties in several aspects: mechanical, thermal and electric properties are remarkables for this kind of materials. In the field of energy harvesting, the most interesting properties are their high electric conductivity and ion intercalation. The latter is the most important charactersitic for electrochemical capacitors, since cations like Li^+, Na^+, NH_4, Mg^{2+}, Al^{3+} can be electrochemically intercalated between MXenes layers. $Ti_3C_2T_x$ is the most studied MXene for supercapacitors, especially in acid media [2]. To improve their properties, MXenes can be combined with conductive polymers able to intercalate between layers of MXenes. This structure prevents the restacking fo MXenes layers increasing the ionic conductivity and the surface available for ionic interchange. PEDOT is a good candidate for this work as it has been demonstrated in [3, 4].

10.2 Flexible supercapacitors

In this work, two types of flexible electrodes for supercapacitors have been studied, LIG electrodes and MXene/poly(3,4-ethylenedioxythiophene) (PEDOT) electrodes. Both were studied in aqueous electrolyte consisting of a solution of 1M H_2SO_4. However, liquid electrolytes are not a suitable option for wearables flexible supercapacitors. Gel electrolytes are the alternative for this kind of devices, so the LIG electrodes were also tested with a gel electrolyte.

The electrodes were tested using Cyclic Voltammetry (CV) at scan rates

[1] Reprinted from Ceramics International, vol. 45, Ronchi et. al, Synthesis, structure, properties and application of MXenes: Current status and perspectives, 18167-18188, 2019, with permission from Elsevier.

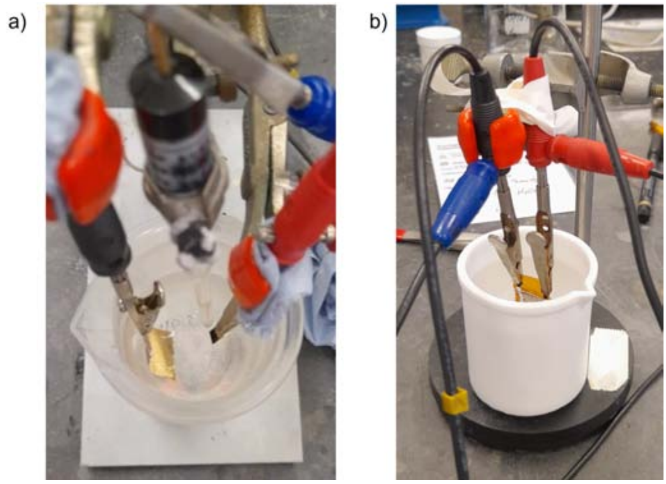

Figure 10.2: Measurement setup for the electrodes in aqueous 1M H_2SO_4 electrolyte; a) Half-cell three electrode setup; b) Full-cell two electrodes setup.

between 10 and 200 mV/s. The measurement equipment was an Autolab PGSTAT302N used with three-electrode measurement setup for half-cell measurements and two electrode configuration for full-cell measurements. Figure 10.2a shows the experimental setup for half-cell measurements and Figure 10.2b full-cell measurement.

As explained above, gel electrolytes are needed for wearable flexible supercapacitors. These electrolytes are based on a hydrogel with high ionic content, and typical polymers used for this are Poly-Vinyl Alcohol (PVA), Polyvinylidene fluoride (PVDF) or PolyCarbonate (PC), which are later combined with strong acids or bases that provide the ions to the electrolyte. In this work, a PVA/H_2SO_4 electrolyte that was prepared by dissolving 1 g of PVA in 10 ml of 1M H_2SO_4, stirred at 80°C during 2 hours, and was later extended over the electrodes.

10.2.1 Laser Induce Graphene electrodes

As the biosignals electrodes discussed above, the electrodes for supercapacitors were obtained using a 22.5-W laser at a speed of 1.08 m/s over Kapton with a thickness of 50 μm. Two versions of the electrodes are presented in this work, one IDE and the other one with a square shape. The IDE electrode has six fingers with a width of 1 mm and a space between them of 1 mm.

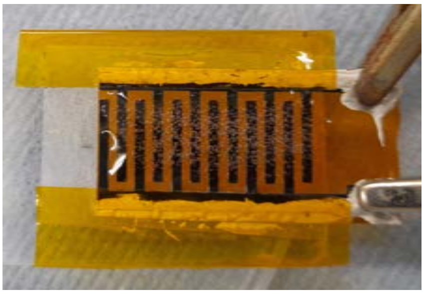

Figure 10.3: Full cell made of LIG with gel electrolyte.

The first experiment carried out was the characterization of LIG electrode with a half-cell setup in aqueous electrolyte using the square electrodes. Figure 10.4 shows the result of this experiment. As it can be observed in Figure 10.4a, the CV curve is tilted, which means a high series resistance of the cell. Figure 10.4b shows the specific differential capacitance of the electrode, defined as:

$$\frac{dq}{AdV} = \frac{i(V)}{s}\frac{1}{A} \tag{10.1}$$

where s is the scan rate and A is the area of the electrode. This parameter allows a better comparison between the devices and the scans. The specific capacity of the electrode can be derived by integrating the function:

$$C_A = \frac{1}{\Delta V A}\int \frac{dq}{dV}dV = \frac{1}{\Delta V A}\int idt \tag{10.2}$$

so the internal area of the curve is the capacitance of the device.

As it can be observed, the capacitance remains constant for low scan rates while for scan rates above 50 mV/s the capacitance is noticeably reduced. This is because the resistance loses will increase with the higher current at these scan rates. This resistance is originated by the geometry of the electrodes that generate a long current path to the current collector. A larger current collector is used in the complete cell setup to solve this problem

To test a full cell, two IDE electrodes, like the one in Figure 10.3, with 1 mm of space between the fingers were used. This experiment was carried out using both liquid and gel electrolyte. Figure 10.5 shows the CV curves of this device in both scenarios, with liquid and gel electrolyte. As it can be seen in Figure 10.5a, in the gel electrolyte, the classical pseudocapacitance CV curve is clearly noticeable. The capacitance is also stable with the scan rates. On the other hand, with liquid gel (Figure 10.5b) the pseudocapacitance behavior is not present and there is a big reduction peak when using low scan rates. Figure 10.5c shows a comparative between the capacitance per

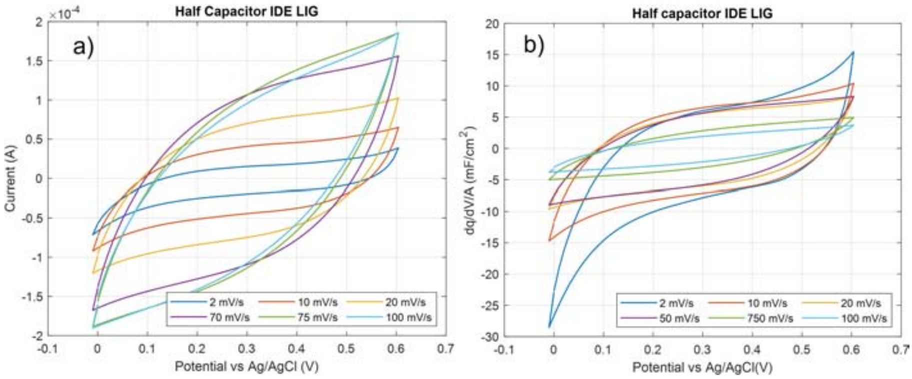

Figure 10.4: LIG electrode CV voltammetry. (a) CV curves of half cell made with LIG electrodes; (b) Differential capacity normalized to area of the electrode.

area of each electrolyte at different scan rates. The device with gel electrolyte has better performance except for the 2mV/s scan, in which liquid is much higher. This is due to the big reduction peak of this scan, which is a non-reversible process, so it is not a capacitive behavior. Ignoring this point, the better capacitance is 180 mF/cm^2 for the gel electrolyte at 50 mV/s.

10.2.2 MXenes/PEDOT:PSS electrodes

The formation of MXenes/PEDOT hybrid films was done from Ti_3C_2F Mxene, which was then blended with PEDOT:PSS in two different proportions: one compound was made in a mass ration of 2:1 (MXene:PEDOT), denoted as MP21, and the other one in a mass ratio of 1:1, denoted as MP11. Additionally, DMSO was also added to increase PEDOT/PSS conductivity [5, 6]. The compound obtained from this process has a high water content, so the components would precipitate if it was used to create films. To avoid this, the compounds were kept stirred until the viscosity increased, then the compoud was deposited and dried under vacuum on a flat leveled surface. Figure 10.6 shows the curves obtained from the compound with double the mass of MXenes than polymer (MP21). Here, the redox pikes are appreciable at 0.5 V in the case of the oxidation peak and 0.4 V in the case of the reduction peak. It is also noticeable the reduction of capacitance with lower scan rates.

In Figure 10.7 the CV curves for the compound with the same amount of MXenes and PEDOT:PSS are shown. In this case the reduction and oxidation peaks are at the same voltage, but with a higher contribution

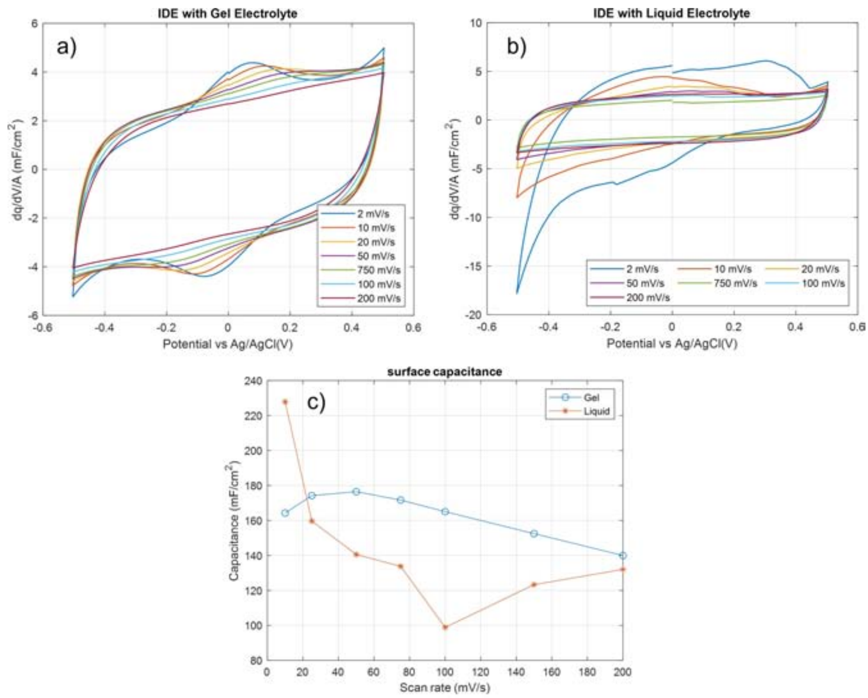

Figure 10.5: Comparative between liquid and gel electrolyte in full-cell measurements. a) Gel electrolyte; b) Liquid electrolyte; c) Surface capacitance comparative.

than in the previous case. It also exists a reduction of capacitance with the scan rate variation in this compound.

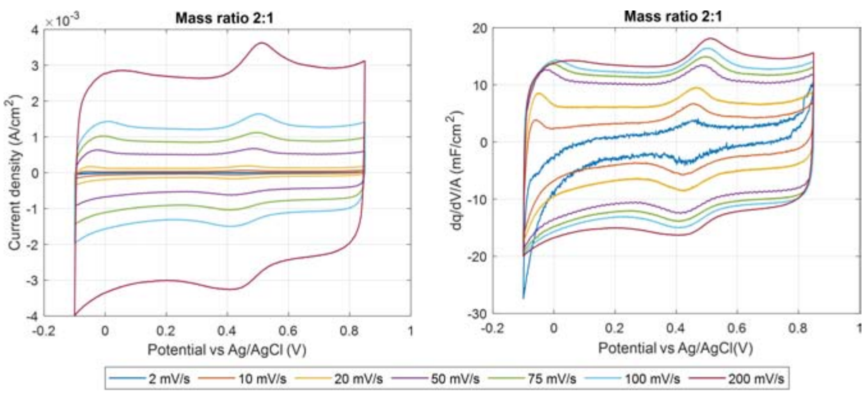

Figure 10.6: CV curves for the MP21 compound: a) CV curve; b) Differential capacitance curve normalized to the area.

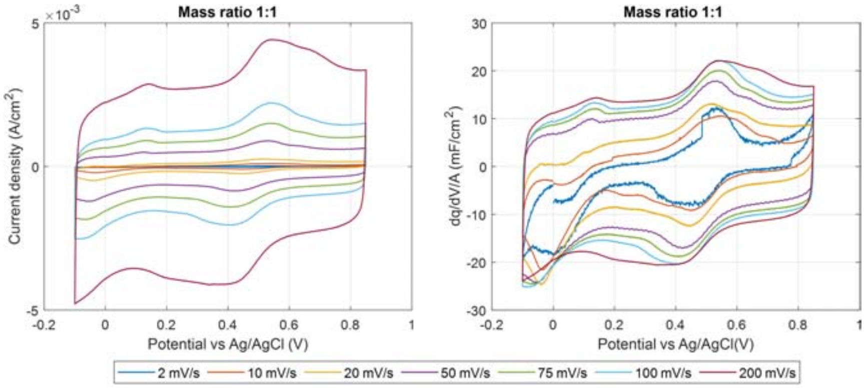

Figure 10.7: CV curves for compound MP11: a) CV curve; b) differential capacitance curve normalized to the area.

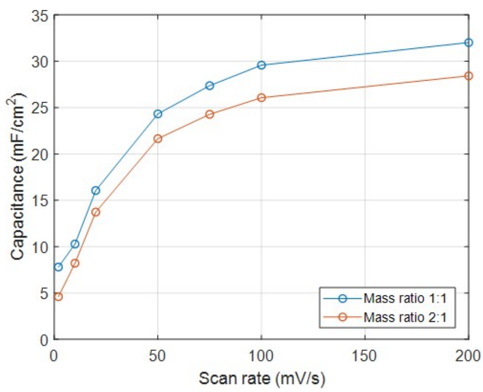

Figure 10.8: Comparative of surface capacitance.

In Figure 10.8 a comparative between the specific capacitance of MP11 and MP12 is shown. As it can be observed, the capacitance of MP11 compound is higher than the other compound as expected from the CV curves. This difference can be explained by the different molecular mass of both compounds. As PEDOT has a higher mass, with an equal mass ratio, the number of molecules of it will be lower than MXenes molecules. Then, the amount of PEDOT in MP21 compound is too low to effectively avoid the restacking of MXenes Thus, this compound will allow better intercallation of ions than the previous one. In any case, further research on this process is still required to explain more accurately this process.

10.3 Conclusions

The study of novel materials for flexible supercapacitor electrodes has been presented in this chapter. LIG and MXenes have been demonstrated to be great candidates for flexible supercapacitors, either with liquid or gel electrolytes.

LIG is a great option for capacitors, since it has a pseudocapacitive behavior but it requires an appropriate current collector to avoid parasitic resistance effects. In combination with a PVA/H_2SO_4 electrolyte, a full cell with LIG electrodes can reach capacitances of 180 mF/cm^2, similar to others in the literature [7, 8].

The other material studied is the Mxene Ti_3C_2F combined with PEDOT:PSS. This conductive polymer can improve the performance of the MXene as supercapacitor electrode. Two compounds, MP11 and MP21, were obtained by mixing the polymer and the MXene in different proportions. The compound with better performance was the MP11 compound, which had the same mass of MXenes and polymer. The maximum capacitance in this case is 32 mF/cm^2. This result is still far from results in the literature, so further optimizations of the process are still required [9, 10, 11, 4].

Bibliography

[1] N. Goossens, B. Tunca, T. Lapauw, K. Lambrinou, and J. Vleugels, "MAX phases, structure, processing, and properties," in *Encyclopedia of Materials: Technical Ceramics and Glasses*. Elsevier, 2021, pp. 182–199.

[2] R. M. Ronchi, J. T. Arantes, and S. F. Santos, "Synthesis, structure, properties and applications of MXenes: Current status and perspectives," *Ceramics International*, vol. 45, no. 15, pp. 18 167–18 188, oct 2019.

[3] L. Qin, Q. Tao, A. E. Ghazaly, J. Fernandez-Rodriguez, P. O. Å. Persson, J. Rosen, and F. Zhang, "High-performance ultrathin flexible solid-state supercapacitors based on solution processable $mo_{1.33}c$ MXene and PEDOT:PSS," *Advanced Functional Materials*, vol. 28, no. 2, p. 1703808, nov 2017.

[4] J. Ma, S. Zheng, Y. Cao, Y. Zhu, P. Das, H. Wang, Y. Liu, J. Wang, L. Chi, S. F. Liu, and Z.-S. Wu, "Aqueous MXene/PH1000 hybrid inks

for inkjet-printing micro-supercapacitors with unprecedented volumetric capacitance and modular self-powered microelectronics," *Advanced Energy Materials*, vol. 11, no. 23, p. 2100746, apr 2021.

[5] O. Dimitriev, D. Grinko, Y. Noskov, N. Ogurtsov, and A. Pud, "PEDOT:PSS films—effect of organic solvent additives and annealing on the film conductivity," *Synthetic Metals*, vol. 159, no. 21-22, pp. 2237–2239, nov 2009.

[6] J. Dong and G. Portale, "Role of the processing solvent on the electrical conductivity of PEDOT:PSS," *Advanced Materials Interfaces*, vol. 7, no. 18, p. 2000641, jul 2020.

[7] F. J. Romero, D. Gerardo, R. Romero, I. Ortiz-Gomez, A. Salinas-Castillo, C. L. Moraila-Martinez, N. Rodriguez, and D. P. Morales, "Comparison of laser-synthetized nanographene-based electrodes for flexible supercapacitors," *Micromachines*, vol. 11, no. 6, p. 555, may 2020.

[8] Z. Peng, J. Lin, R. Ye, E. L. G. Samuel, and J. M. Tour, "Flexible and stackable laser-induced graphene supercapacitors," *ACS Applied Materials & Interfaces*, vol. 7, no. 5, pp. 3414–3419, jan 2015.

[9] Y. Zhou, K. Maleski, B. Anasori, J. O. Thostenson, Y. Pang, Y. Feng, K. Zeng, C. B. Parker, S. Zauscher, Y. Gogotsi, J. T. Glass, and C. Cao, "Ti3c2tx mxene-reduced graphene oxide composite electrodes for stretchable supercapacitors," *ACS Nano*, vol. 14, no. 3, pp. 3576–3586, feb 2020.

[10] Z. Fan, Y. Wang, Z. Xie, D. Wang, Y. Yuan, H. Kang, B. Su, Z. Cheng, and Y. Liu, "Modified MXene/holey graphene films for advanced supercapacitor electrodes with superior energy storage," *Advanced Science*, vol. 5, no. 10, p. 1800750, aug 2018.

[11] J. Yan, C. E. Ren, K. Maleski, C. B. Hatter, B. Anasori, P. Urbankowski, A. Sarycheva, and Y. Gogotsi, "Flexible MXene/graphene films for ultrafast supercapacitors with outstanding volumetric capacitance," *Advanced Functional Materials*, vol. 27, no. 30, p. 1701264, jun 2017.

Part IV

Conclusions

Chapter 11

Conclusions

The main objective of this Thesis is to investigate and develop flexible electronics for application in wearable devices oriented to healthcare. During this work novel materials and techniques have been used combined with traditional electronics to reach this main objective. The work carried out adds to the state of the art in the following contributions:

- **Novel flexible electrodes**. Novel flexible electrodes based on flexible materials have been investigated and characterized in this work. Mainly two types of electrodes have been tested: printed electrodes and electrodes made of LIG. The electrodes were used for ECG EMG and EOG acquisitions and were compared with commercial Ag/AgCl electrodes, reaching a similar performance than them. LIG electrodes presented the lowest conductivity, however their performance was better for EMG and EOG. Printed electrodes were based on carbon and silver inks and they were screen printed over pet substrate in a patch like structure. Their performance in all signals was similar despite the silver electrodes had lower sheet resistance. The printed electrodes were also studied over textile substrates, focusing the study on the reproducibility of printed patterns and sheet resistance dependence of the substrate. From both of these studies, flexible electrodes have been demonstrated to be an alternative with equivalent performance in signal acquisitions to commercial ones while keeping two advantages: easier fabrication, and therefore lowest cost, and higher comfort and ergonomics for the user in long term monitorization.

- **Printed organic electronics**. In this contribution organic materials like MOFs and CPs have been used for humidity sensing. Two compound were studied as RH sensor over a printed IDE device. First, the optimization of printing techniques was demonstrated to achieve a controlled characteristic of the RH sensor based on MOF. This contribution demonstrated the use of MOF as a flexible printed sensor. Furthermore, a coordination polymer based on sodium ions have been shown as a RH sensor. Another device, using similar techniques, is presented as a

Similar techniques have been used in this case obtaining a device that changes its conductivity over 40% RH. Both presented devices act as a humidity switch, which has advantages on power consumption over capacitive or resistive sensors. Organics electronics have a great potential not only for environmental sensing but also for the development of portable chemical sensing. These type of devices are used in the development of Point Of Care (POC) diagnostics, which is another useful tool for remote diagnosis.

- **Wearable energy harvesting devices**. In this field, several flexible electrodes for supercapacitors have been developed. In this regard, MXenes were used as highly porous materials in combination with flexible polymers to obtain flexible capacitors. Also, LIG supercacitor were presented and studied with liquid and gel electrolytes, reaching high capacitances of up to 180 mF/cm2. This contribution demonstrated the use of novel materials for completely flexible energy storing devices. The research on MXenes/polymer electrodes analyzed how the proportion of each component affect to capacitance, showing up that an equal amount of MXenes and PEDOT resulted in better performance. However, this research still requires further optimization of the electrodes. MXenes have also a big potential in others energy harvesting devices such as TEG, which have great interest for the wearable electronics field.

- **Adaptable sensing platform**. Finally, this Thesis has contributed with several devices to use the technologies detailed above, highlighting a versatile reconfigurable platform. This innovative device allows the use of flexible electrodes and sensors in a single device, which can be used as POC chemical analysis device in combination with μPAD sensors. This platform could improve its ergonomics with a fully flexible design, however, complex silicon chips are still far from being completely flexible. Nevertheless, a flexible PCB would allow the device to completely adapt to different parts of the body.

Part V

Appendices

Appendix A

Supplementary information to Chapter 6

A.1 Powder XR Diffraction (PXRD) Analysis

The powders were gently ground in an agate mortar and then deposited with care in polyethylene terephthalate. Diffraction data (Cu Kα, $\lambda = 1.5418$ Å) were collected on a $\theta : \theta$ Bruker AXS D8 vertical scan diffractometer equipped with primary and secondary Soller slits, a secondary beam curved graphite monochromator, a Na(Tl)I scintillation detector, and pulse height amplifier discrimination. The generator was operated at 40 kV and 40 mA. Optics used were the following: divergence 0.5°, antiscatter 0.5°, receiving 0.2 mm. A long scan was performed with $5 < 2\theta < 30°$ with t = 5 s and $\Delta 2\theta = 0.02°$.

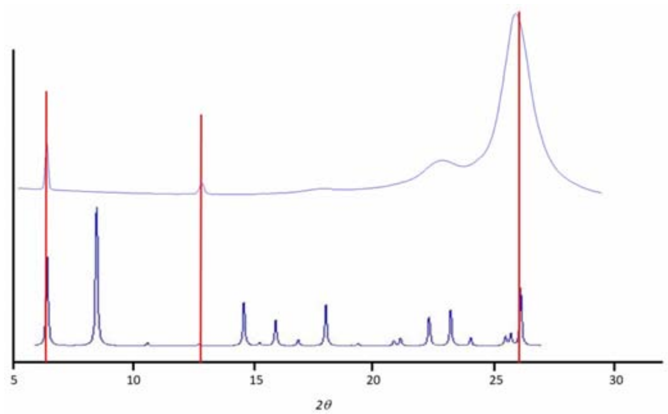

Figure A.1: Top: Experimental PXRD of sample after spray coating deposition. Down: Theoretical PXRD obtaining of single crystal data.

As can be shown, the main peaks of the experimental measurement coincide with the theoretical peaks of the diffractogram obtained from the crystalline data. Peaks: 6.32 (hkl 001), 12.67 (hkl 002), and 26.09 (hkl 301).

A.2 Impedance response figures

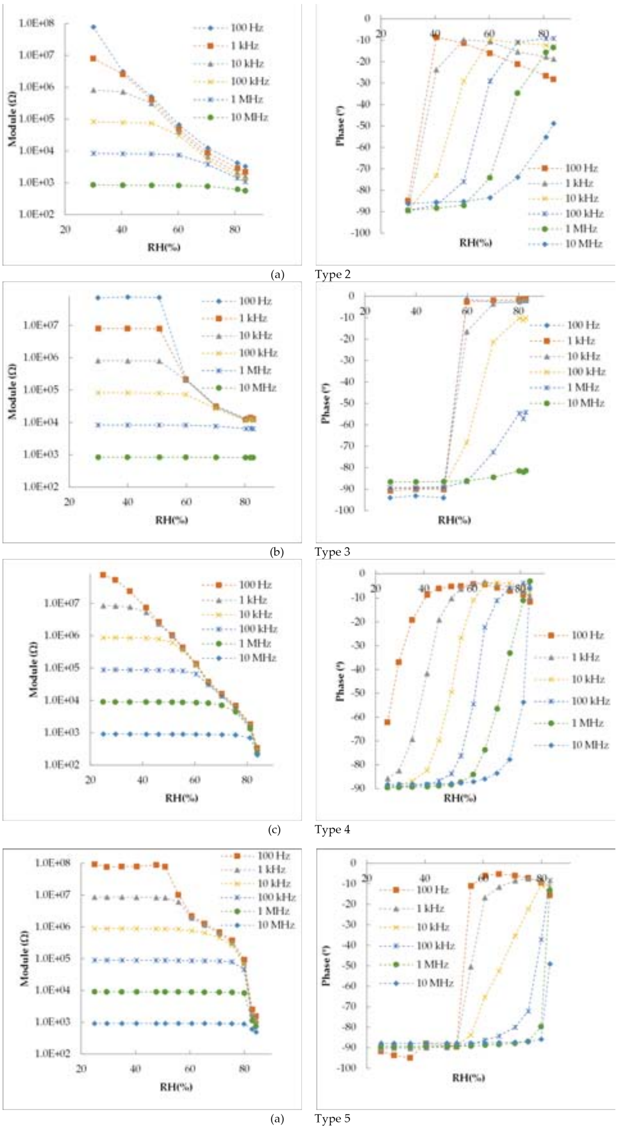

Figure A.2: Impedance response towards RH at 40 °C for different operating frequencies for sensors with interspacing of 300 µm: (a) type 2; (b) type 3; (c) type 4; (d) type 5. Module is depicted in the left column and phase in the right one.

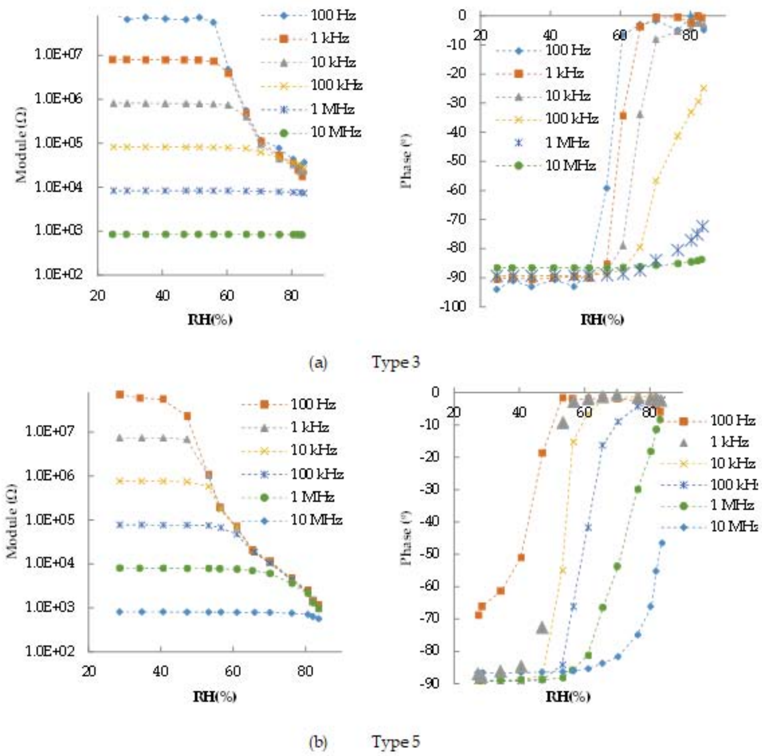

Figure A.3: Synthetic scheme with the structure of the MOF.

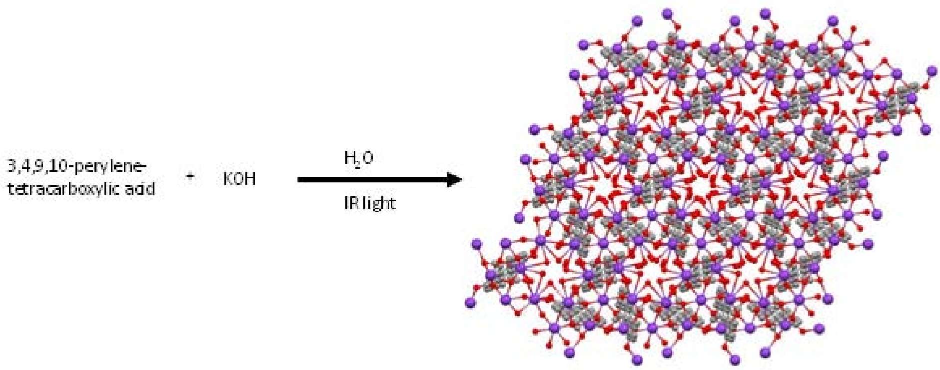

Figure A.4: Synthetic scheme with the structure of the MOF.